Christian-Albrechts-Universität zu Kiel
Institut für Theoretische Physik und Astrophysik

Kinetic Monte Carlo Simulations of Metal-Polymer Nanocomposite Formation

Dissertation
zur Erlangung des Doktorgrades
der Mathematisch-Naturwissenschaftlichen Fakultät
der Christian-Albrechts-Universität zu Kiel

vorgelegt von
Lasse Rosenthal

Kiel, 2013

Erster Gutachter:	Prof. Dr. Michael Bonitz Institut für Theoretische Physik und Astrophysik, Christian-Albrechts-Universität zu Kiel, Leibnizstraße 15, 24098 Kiel, Deutschland
Zweiter Gutachter:	Prof. Dr. Franz Faupel Institut für Materialwissenschaft - Materialverbunde, Christian-Albrechts-Universität zu Kiel, Kaiserstraße 2, 24143 Kiel, Deutschland
Tag der mündlichen Prüfung:	24. September 2013
Zum Druck genehmigt:	24. September 2013

gez.

_____

Dekan

Abstract

This work deals with the investigation of metal-polymer nanocomposite formation by means of kinetic Monte Carlo simulations. The focus of the analysis lies on diffusion and growth processes of metal clusters in the polymer matrix. To this end, a simulation model based on a catalog of elementary processes including corresponding rates covering the main cluster processes during metal-polymer nanocomposite formation and the notion of clusters as hard spheres was developed and implemented. Due to the simplifications of the underlying model, the simulations allowed for an investigation of systems consisting of up to several million metal clusters.

The simulations cover two different experimental scenarios. The first one is the formation of a metal-polymer interface. Here, metal atoms are deposited on a polymer surface. The second scenario is the simultaneous deposition of metal atoms and polymer. In both cases, special emphasis is placed on the influence of the process rates on quantities such as the metal concentration inside the polymer matrix, the cluster size distribution and the metallic filling factor.

Additionally, a simulation model was developed to describe the self-organized formation of metallic nanocolumns which was discovered under specific conditions during vapor phase co-deposition of the metallic and organic component. A key aspect of the discovered nanocolumn growth is a steep increase of the metallic filling factor at the transition from spherical to columnar growth. The simulations have provided a detailed understanding of the correlation between the increase of the metallic filling factor and the beginning of nanocolumn formation in terms of a few elementary process.

Kurzbeschreibung

Anmerkung: Diese Arbeit wurde auf Englisch verfasst. Die Kurzbeschreibung ist eine Übersetzung der englischen Fassung von Seite i.

Diese Arbeit handelt von der Untersuchung der Bildung von Metall-Polymer Nanokompositen auf Basis von kinetischen Monte-Carlo-Simulationen. Der Schwerpunkt der Analyse liegt auf Diffusions- und Wachstumsprozessen von Metallclustern in der Polymer-Matrix. Zu diesem Zwecke wurde ein Simulationsmodell entworfen und implementiert, welches auf einer Liste von elementaren Prozessen mit entsprechenden Prozessraten sowie der Annahme von Clustern als harten Kugeln basiert. Aufgrund der Vereinfachungen des zugrunde liegenden Modells ermöglichten die Simulationen die Untersuchung von Systemen, welche aus mehreren Millionen Metallclustern bestehen.

Die Simulationen decken zwei verschiedene experimentelle Szenarien ab. Das erste ist die Ausbildung einer Metall-Polymer-Grenzfläche. Hierzu werden Metallatome auf einer Polymer-Oberfläche abgeschieden. Das zweite Szenario ist die simultane Abscheidung von Metallatomen und Polymermolekülen. In beiden Fällen liegt das Augenmerk auf dem Einfluss der Prozessraten auf Größen wie z. B. der Metallkonzentration innerhalb der Polymer Matrix, der Größenverteilung der Cluster und dem metallischen Füllfaktor.

Zusätzlich wurde ein Modell zur Beschreibung des selbstorganisierten Wachstums von metallischen Nanosäulen, welches unter speziellen Bedingungen während der simultanen Gasphasenabscheidung der metallischen und organischen Komponenten entdeckt wurde, entwickelt. Ein zentraler Aspekt des entdeckten Nanosäulenwachstums ist ein sprunghafter Anstieg des metallischen Füllfaktors beim Übergang vom sphärischen Wachstum zum Säulenwachstum. Die Simulationen liefern ein detailliertes Verständnis

der Korrelation zwischen dem sprunghaften Anstieg des Füllfaktors und dem Einsetzen des Säulenwachstums auf Basis einiger weniger elementarer Prozesse.

Contents

List of Figures

CHAPTER 1

Motivation and Outline

Due to the ongoing success of nanochemistry and nanotechnology, the research field of nanocomposite materials has received increased attention since the end of the twentieth century. This results from the fact that the combination of the contradicting properties of the nm-sized filler particles and the host material allows for the production of multifunctional materials that can serve various functions. Examples include numerous applications in optics based on surface plasmon resonance [1, 2], electronics[3–6], food packaging [7], and medicine [8, 9]. However, nanocomposites are also widespread in biological systems. One striking example of a naturally occurring composite material is the inner shell layer produced by some molluscs, known as nacre (mother of pearl). Despite the brittle structure of its constituents, nacre exhibits a very high resilience and toughness which exceeds the toughness of its constituent materials by a factor of 1000 [10]. Due to its remarkable mechanical properties, nacre not only serves for decorative use, but is also an inspiration for the development of composite materials that mimic its microscopic structure [11, 12].

An important subcategory of nanocomposites are metal-polymer nanocomposites [13] which are based on a synthesis of nm-sized metallic filler particles dispersed in a polymer matrix. The research on metal-polymer nanocomposites has been triggered off by the need for further miniaturization, especially in microelectronics. Here, the usage of polymers, mostly polyimides, as low-permittivity dielectrics allowed for a significant improvement of speed and packing density of electronic structures. These applications

imply enormous demands on the thermal as well as the mechanical stability of the interface due to exposition to elevated temperatures and thermal cycling during processing and operation [14]. Therefore, improving the thermal load capacity as well as the mechanical resistance is still an active field of research [15, 16]. Yet another important issue is diffusion of metals in polymers. It has been shown that the degree of metal-polymer intermixing significantly affects the mechanical and dielectric properties of the interface [17–19].

The aim of the present thesis is to investigate the formation of metal-polymer nanocomposites by means of computer simulations. This work essentially gains its motivation by the research carried out by the Chair for Multicomponent Materials at the University of Kiel. Its aim is is to contribute to the understanding of the coupled processes determining the microstructure of metal-polymer nanocomposites from a macroscopic point of view. Since the complexity of the coupled physical and chemical processes occurring during metal-polymer nanocomposites formation does not allow for a treatment based on microscopic approaches, a simpler simulation approach neglecting the microscopic structure of the constituents has to be applied. Here, the method of choice is the kinetic Monte Carlo method [20] which has seen a remarkable progress over the last decades and which has been successfully applied to study the dynamics of coupled processes leading to structure formation of matter which are not accessible with *ab-initio* methods or continuum descriptions. Within in this framework, a simulation scheme including and combing several approaches of previous simulations [21–24] was developed, implemented and applied to different experimental scenarios such as the formation of a metal-polymer interface, co-deposition of metal and polymer and the self-organized growth of metallic nanocolumns. The implemented model allows for simulations covering all morphological sequences of cluster growth reaching from growth of isolated clusters to percolation.

Substantial simplifications of the simulation model are the neglecting of the inner atomic structure of the clusters and the polymer matrix. Instead, the clusters are modeled within the framework of the liquid drop model [25] and basic effects of the polymer matrix on the clusters are condensed into the diffusion and evaporation rates of clusters. Due to the complexity of the studied system on the one hand and the simplicity of the simulation on the other hand, the simulations are not intended to reproduce experimental outcomes quantitatively. Rather, the intention is to understand and predict qualitative changes due to variations of the deposition conditions. To this end, the simulation model is designed in such a way that the simulations allow for a detailed investigation of

systems containing up to several million metal clusters.

Thesis Outline

Part I. Introduction and basic Theory.

Chapter 2 provides an introductory review on metal-polymer nanocomposites. The fundamental physical processes occurring during metal-polymer nanocomposites are discussed. This is followed by a listing of some of the most frequently used manufacturing techniques for nanocomposite production. Finally, the chapter finishes with a brief overview of computer simulations of nanocomposites of the last 30 years.

Chapter 3 is devoted to a detailed discussion of the theory of continuous-time Markov chains which provides the foundations for the kinetic Monte Carlo method. Therefore, the chapter starts with a recapitulation of basic concepts of probability theory. In the following, the definition of continuous-time Markov chains and their main properties are laid out. The chapter culminates with a discussion of two algorithms for the numerical treatment of continuous-time Markov chains.

Part II. Kinetic Monte Carlo Simulations.

Chapter 4 gives a detailed description of the simulation model. Much emphasis is hereby devoted to the physical motivation of the process rates. Also covered is the simulation algorithm which has been used in the simulations. The algorithm is explained by means of a flowchart which illustrates the basic procedure of the program.

In **Chapter 5**, simulation results of the formation of a metal-polymer interface are presented and extensively discussed. The focus of this chapter lies on the discussion of the distribution of metal clusters in the polymer matrix and the size distribution of clusters in terms of the underlying elementary processes included in the simulations. To this end, the chapter begins with the discussion of the simple case of fully condensating metal atoms on a polymer surface which is free of defects. Additional effects such as surface defects, evaporation of monomers, and the formation of a percolating network are discussed.

Chapter 6 is concerned with simulations of co-deposition of metal and polymer. Central to this chapter are simulations of the self-organized formation of metallic nanocolumns which was discovered during co-deposition of a Fe-Ni-Co alloy and Teflon. To cover this effect in the simulations, a second cluster growth mechanism, leading to the formation of columnar structures, is introduced and discussed. Emphasis is placed on the analysis of the correlation between the transition from spherical cluster growth to nanocolumn formation and the steep increase of the metallic filling factor which was observed in experiments.

The thesis concludes with a recapitulation of the presented results in **Chapter 7**.

Part I

Introduction and basic Theory

CHAPTER 2

Metal-Polymer Nanocomposites: Main Properties and Fabrication

This chapter gives a short introductory review on nanocomposites based on metallized polymers. The chapter is divided into four sections. First, some research fields and possible technical applications of metal-polymer nanocomposites are briefly reported. In the second section, the fundamental physical processes occurring during manufacturing of metal-polymer nanocomposites are discussed. Hereby, special emphasis is placed on processes of the metallic filler. Further, an enumeration and an explanation of some of the most important manufacturing techniques of nanocomposites are given, and a subsequent overview about computer simulations done by other groups completes the chapter.

2.1 Properties of Metal-Polymer Nanocomposites

Nanocomposite science labels the study of multiphase composite materials with at least one phase appearing in the form of nm-sized particles or clusters having a dimension of less than 100 nm [26]. The benefits of nanocomposite materials are manifested in multi-functional properties due to the combination of advantageous features of their constituents into one material. Among the potential technical applications related to nanocomposite materials with metallic nanoparticles as fillers are devices with electrical resistivity ranging from single-electron hopping [3, 4] to metallic [5, 6], giant magne-

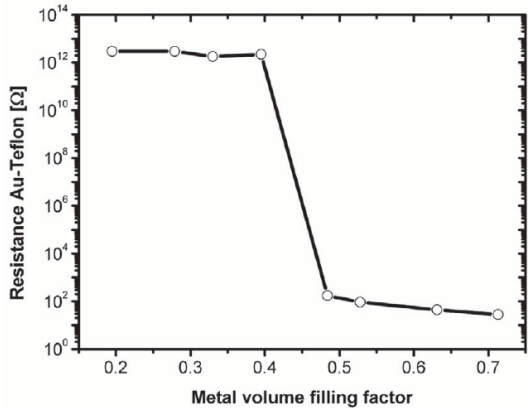

Figure 2.1: *Change of the electrical resistance in an Au-Teflon nanocomposite due to variation of the metallic filling factor. With kind permission reprinted from Ref. [28].*

toresistance [27], and tunable particle plasmon resonance frequencies [1, 2]. Specifically, metal-polymer nanocomposites [13] based on a synthesis of a nm-sized metallic filler dispersed in polymer host matrix allow for the production of promising materials with novel properties. Particularly, the need for further miniaturization and advanced packaging in the field of microelectronics has stimulated intensive research on metal-polymer nanocomposites [14] since polymers are generally low-cost materials which can well be processed into thin films and maintain mechanical and thermal stability upon processing under various ambient conditions. A striking example of electronic properties of a metal-polymer nanocomposite based on Au and Teflon is reported in [28], see Fig. 2.1. Here, Takele et al. report about a nanocomposite prepared by vapor phase co-deposition which spans ten magnitudes of electrical resistance ranging from $10^{12}\,\Omega$ to $10^{2}\,\Omega$. The investigated nanocomposite exhibited a percolation threshold at a metallic filling factor (i.e., the volume fraction of metallic nanoparticles) around 0.43. Once the filling factor exceeded this value, the electrical resistance quickly dropped by a factor of 10^{10}.

However, the potential application field of metal-polymer nanocomposites is not restricted to microelectronics; other important fields are optics [28–31], organic memory devices [32], and even antibacterial coatings [9, 33] finding application in food packaging [7].

2.2 Physical Aspects of Polymer Metallization

Metals and polymers are materials with very contrasting properties. Polymers are covalently bonded chain molecules built from repeating structural units, the so-called

monomers, which can be very simple chemical structures like in polyethylene, $-CH_2-$, or very complex compounds itself [34]. Many polymers exist in the glass state with no long-range order. There are polymers such as polyethylene oxide which exhibit crystalline structures; however, interconnection of polymer chains prevents crystalline regions from extending over large areas [34]. Polymers usually have small cohesive energies due to the weak interaction between polymer chains which is mediated by the weak van der Waals force. Due to the large number of monomers a polymer is made of (10^2–10^5) and the degrees of rotational freedom of covalent bonds at nearly constant bond angle and energy, polymer chains may attain an almost uncountable number of spatial arrangements allowing for a description in terms of the random coil model [35].

In contrast to that, metals tend to form densely packed crystalline structures whose physical characteristics arise from the strong metallic bonds between the atoms. Therefore, the cohesive energy of metals exceeds the cohesive energy of polymers by typically two orders of magnitude [13, 35, 36] and they exhibit a strong tendency to aggregate and form clusters (Volmer-Weber growth) during the metallization process.

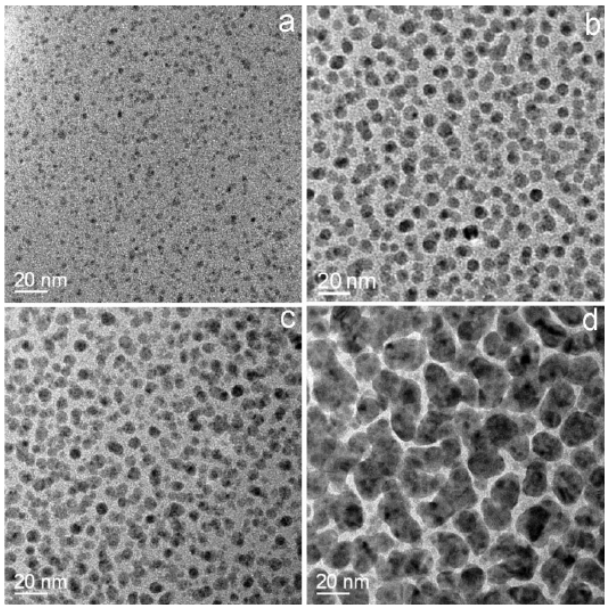

Figure 2.2: *TEM micrographs of Nylon-Ag nanocomposites with a thickness of about 60 nm and different metallic filling factors: a) 4.4%, b) 14%, c) 21%, and d) 41.5%. The transition from isolated clusters growth a) to elongated islands emerged from overlapping clusters b,c) and finally the percolation network d) is clearly illustrated. With kind permission reprinted from Ref. [30].*

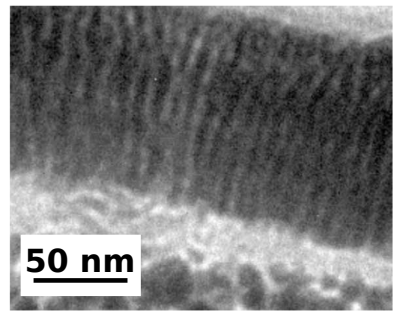

Figure 2.3: *Cross-sectional TEM image showing the formation of Fe-Ni-Co nanocolumns in Teflon AF on top of a layer of Ag clusters isolated by 20 nm of the same matrix. With kind permission reprinted from Ref. [42].*

2.2.1 Nucleation of Metals in Polymers

The initial stage of polymer metallization is far away from thermodynamic equilibrium as metal atoms impinge on the polymer surface and undergo a rather complex dynamics afterwards. Essential processes of these dynamics are random diffusion on the surface and into the bulk (see Sec. 2.2.2) and re-evaporation from the surface (see Sec. 2.2.4). If two metal atoms encounter each other on their path, they aggregate and form a cluster. Clusters are stable if their size exceeds the critical nucleus size which was experimentally determined to be one [37], implying that already dimers form stable clusters and do not decompose. The nucleation of clusters is mainly driven by two processes: the first one is random nucleation by encountering clusters. The second one is preferred nucleation which takes place at special surface sites that bind atoms and clusters [14]. The exact nature of these surface sites is not known, but the number density of these sites can be influenced with ion-beam treatment [37]. Preferred nucleation is expected to be the dominant growth mechanism in the early stages of polymer metallization and for low condensation coefficients (the condensation coefficient $\mathcal{C}$ is defined as the ratio of the number of adsorbed atoms to the total number of atoms impinging on the surface). Under different conditions, random nucleation is expected to dominate [14, 36]. Both growth mechanisms have been observed in experiments [38–40].

Cluster growth during polymer metallization can be categorized into different morphological sequences. The first stage can be identified by the growth of compact isolated islands which develop towards elongated islands in the second stage. These elongated islands start to overlap and build a percolating network in the third stage and, finally, form a continuous film spanning the entire substrate in the fourth stage [21, 41]. Fig. 2.2 shows transmission electron microscopy (TEM) micrographs illustrating these sequences.

Recent experiments have shown that agglomeration of metal atoms is not restricted

to growth of spherical clusters: under specific conditions, co-deposition (see Sec. 2.3) of the metallic and the polymer component can be applied to produce parallel metallic nanocolumns as it was reported for a Fe-Ni-Co alloy in a Teflon AF matrix [42]. TEM images of these nanocolumns, see Fig. 2.3, have shown that they are parallel arranged and exhibit a homogeneously distributed aspect ratio. In Sec. 6.2, the results from kinetic Monte Carlo (KMC) simulations of nanocolumn growth are presented.

2.2.2 Diffusion of Metals in Polymers

From the technological point of view, diffusion of metals in polymers is of great interest. Especially in microelectronics, where polymers are used as low-k dielectrics (a material with a small dielectric constant) to build electronic devices, the need for further miniaturization has triggered intensive research on diffusion of metals in polymers [17, 18, 43]. Since even small amounts of metal diffusing from the conductance lines act as deep impurities and increase the parasitic capacitance between the conductance lines, one central task of this research is to develop efficient methods to block metal diffusion in polymers by some barrier [14, 43]. While metals are known to form thin films and clusters obeying Volmer-Weber growth [45] when they are deposited on a polymer surface, the intermixing of metals and polymers depends on their chemical interaction. For low reactivity metals like Cu, Ag, Au, and Pd, which exhibit weak chemical interactions with

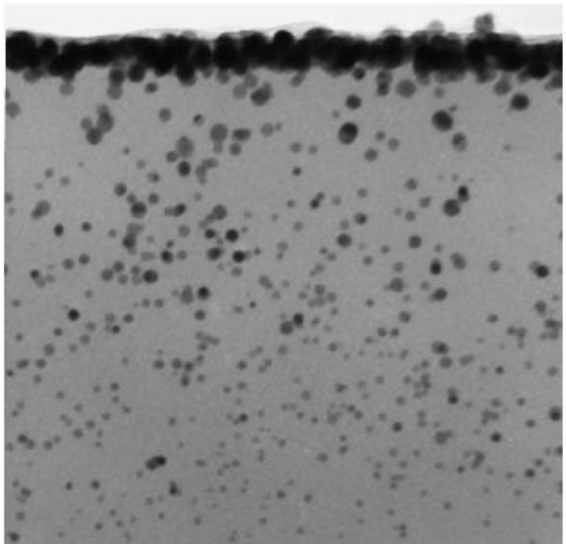

Figure 2.4: *Cross-sectional TEM micrograph of an Au-TMC-PC interface. Au was deposited with a rate of about 0.03 nm/min at 235 °C. The micrograph shows the interface after annealing for 12 h at 290 °C. The glass transition temperature of TMC-PC lies around 235 °C. The depicted sample has a width of about 320 nm. With kind permission reprinted from Ref. [44].*

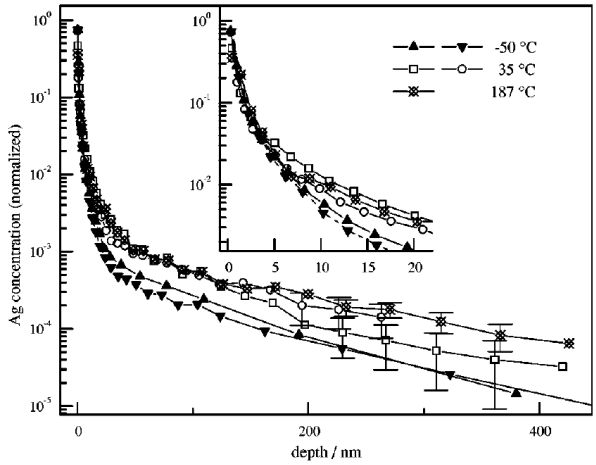

Figure 2.5: *Experimental concentration profile of Ag in trimethylcyclohexane polycarbonate obtained by radiotracer measurements in conjunction with ion-beam sputtering at different temperatures. With kind permission reprinted from Ref. [43].*

polymers [14], almost no intermixing with polymers should be expected due to their high aggregation tendency [35, 46].

In contradiction to these predictions, LeGoues et al. performed TEM studies of the Cu–pyromellitic dianhydride-oxydianiline (PMDA-ODA) interface in the 1980s, which revealed a remarkable migration of Cu into the PMDA-ODA and subsequent formation of spherical agglomerates below the surface at temperatures between 293 K and 573 K [17, 18]. These investigations have also shown that diffusion of Cu into polyimide is restricted to low deposition rates and elevated temperatures; a high deposition rate at elevated temperature effectively impeded diffusion and clustering of Cu under the surface as well as room temperature deposition and subsequent annealing. Tromp et al. drew the conclusion that an accelerated cluster growth on the surface due to enhanced deposition rates impedes diffusion of Cu under the surface, implying that diffusion into polymers is dominated by atoms and small clusters [17]. These conclusions are supported by experiments verifying the aggregation-induced immobility of Cu on polyimide [47].

Similar behavior for the Ag-polyimide interface [48, 49] and other metal/polymer combinations was observed in further experiments [14]. For metals forming strong chemical bindings with polymers, diffusion inside the polymer was found to be significantly reduced [18].

Atomic diffusion coefficients of metals in polymers have been studied by employing radiotracer measurements in conjunction with ion-beam sputtering [43, 50, 51]. This technique allows to determine depth-resolved concentration profiles from which the diffusion coefficients can be deduced by fitting the linear tail of the profile to the thin-film

solution of Fick's second law [43, 51]. An experimental concentration profile is depicted in Fig. 2.5.

Thran et al. have reported radiotracer measurements of the diffusion of Ag in TMC-PC, which clearly proved a migration of Ag into TMC-PC over large distances even at room temperature [43].

2.2.3 Embedding of Clusters

Diffusion of metals in polymers is a process which is not restricted to thermodynamical equilibrium and which may take place below as well as above the glass transition temperature. However, if the temperature of the polymer exceeds the glass transition temperature, embedding of clusters under the polymer surface may become energetically favorable due to the long-range mobility of the polymer chains. The driving force behind this process is caused by lowering the Gibb's free energy of the cluster-polymer system by embedding of clusters. The Gibb's free energy of a single cluster and the polymer consists of three contributions [52]:

$$G_c(z) = 2\pi r z \gamma_{mp} + 4\pi r^2 \gamma_m - 2\pi r z \gamma_m - \pi \gamma_p \left(r^2 - (r-z)^2\right), \quad 0 \leq z \leq 2r\,, \tag{2.1}$$

where $\gamma_{m(p)}$ denotes the surface tension of the metal(polymer) component and γ_{mp} the metal-polymer interface tension. The first term goes back to the interaction of the polymer and the embedded part of the cluster, the second and third term describe the contribution of the part of the cluster which projects above the surface, and the last term takes into account the reduction of the polymer surface tension caused by the embedded cluster, see also Fig. 2.6

If $G_c(z)$ monotonically decreases, the Gibb's free energy will continuously be lowered by embedding the cluster into the polymer bulk. This leads to the following inequal-

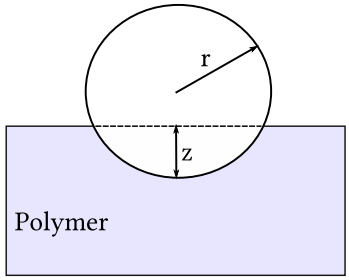

Figure 2.6: *Illustration of a partially embedded cluster with radius r and embedding depth z.*

ity [53, 54]:

$$G_c'(z) = 2\pi r\gamma_{mp} - 2\pi r\gamma_m - 2\pi r\gamma_p + 2\pi z\gamma_p < 0, \quad 0 \leq z \leq 2r$$
$$\iff \quad \gamma_m > \gamma_{mp} + \gamma_p. \tag{2.2}$$

For most metal/polymer combinations this inequality holds due to the high cohesive energy of metals, thus making submersion of clusters the thermodynamically preferred state.

As stated above, the onset of cluster embedding is expected near the glass transition temperature. Zaporojtchenko et al. performed experiments in which the onset of cluster embedding was used to determine the surface glass transition temperature of the polymer [55]. In these experiments, Cu was deposited on polystyrene (PS) and polycarbonate (PC) films at room temperature. After deposition, the films were heated and embedding of clusters was monitored by X-ray photoelectron spectroscopy (XPS). The XPS signals showed a steep increase which was caused by accelerated embedding of clusters and which could be identified with the surface glass transition.

If a cluster is completely buried under the surface, it still feels a weak van der Waals force pulling it deeper into the bulk due the larger amount of polymer below than above the cluster. This force is balanced by an opposed acting entropic force caused by local compressions of the polymer in the vicinity of the cluster. The interplay of these forces causes a characteristic size dependent minimum of the Gibb's free energy [35, 36], see Fig. 2.7

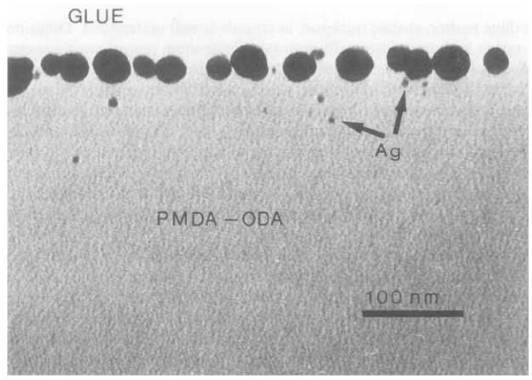

Figure 2.7: *Cross-sectional TEM micrograph of the Ag-polyimide interface. Ag was deposited with a rate of about 0.4 ML/min. at 360 °C. With kind permission reprinted from Ref. [49].*

2.2.4 Condensation of Clusters

When metal atoms are deposited on a metal surface, they usually exhibit a condensation coefficient C close to unity, even at elevated temperatures [14, 36]. The behavior of metal atoms which are deposited on a polymer surface is usually different from those deposited on metal surfaces. The condensation coefficient strongly depends on the metal/polymer combination as well as on the temperature and shows extreme variations by three orders of magnitude ranging from 0.002 for Ag on Teflon AF to 0.95 for Ag on polyimide at room temperature [37, 39, 40]. Radiotracer measurements performed by Thran et al. revealed that incomplete condensation of metal atoms on polymers is not due to direct backscattering of atoms from the polymer surface. Instead, metal atoms perform a random walk on the surface prior to reemission and have to overcome an energy barrier in order to be re-emitted from the surface [39].

If the metal coverage is very high, the probability for metal atoms to impinge on pre-existing metal clusters is drastically enhanced and thus the condensation coefficient reaches almost unity as it is known from metal atoms on metal surfaces [36].

2.3 Techniques of Nanocomposite Preparation

There are many different techniques for the production of metal-polymer nanocomposites. In general, these techniques can be divided into two broad categories, depending on whether they are based on primarily physical or chemical [13] processes. The most important ones among these will be briefly explained in this section.

2.3.1 Physical Approaches

Physical methods of nanocomposite production are based on purely physical means to deposit the metallic and polymer components of the nanocomposite. Among the most successful and versatile strategies is physical vapor deposition (PVD), also known as vapor phase deposition (VPD). PVD is based on the atomization of a solid or liquid source and its subsequent transport through a process chamber towards the surface of a suitable substrate [56]. In order to restrict scattering of the vaporized source with the background gas, and thus maximizing the current of particles impinging on the substrate, PVD has to be processed under vacuum conditions. Since PVD is a line of sight method, the deposition is usually not homogeneous. In many cases, the particle

beams are guided by appropriate electrical fields, or the substrate is rotated [57] in order to prevent shadowing of certain substrate areas.

Generally, PVD-based production of metal-polymer nanocomposites involves co- or tandem deposition of the vaporized metallic and organic components and subsequent formation of the composite by self organization. The main variants of VPD used for nanocomposite synthesis are evaporation, plasma polymerization, and sputter deposition and differ in the way the metallic and organic components are vaporized.

Evaporation

The production of metal-polymer nanocomposites by evaporation of its components was first introduced in the 1970s [58] and successfully applied to different experimental setups in the following years [9, 33, 42, 59–61]. The strength of this technique is that it provides good control over the process operation [33], the metallic filling factor [62], the final size, and the dispersion of metal clusters in the polymer matrix [9, 59]. A general problem of co-evaporation of both the metal and the polymer component is a low sticking coefficient of metal on polymers with low surface energy and a significant reduction of the molecular weight of polymers during VPD [9, 33].

During VPD, the metal and organic components of the nanocomposite are vaporized and subsequently condensed on the surface of a wafer. Strictly speaking, this technique does not involve the evaporation of the polymer chains themselves, but a decomposing of a polymer solid which can be achieved either by thermal breaking of the covalent bonds of the polymer chains and partial re-polymerization on the substrate [42, 62], or by evaporation of its monomers and subsequent polycondensation on the substrate.

Plasma Polymerization

Nanocomposite synthesis based on plasma polymerization uses a gas discharge that provides the energy which is required to ignite polymerization of organic precursors. Most frequently used precursors are fluorocarbon, hydrocarbon, and organosilicon [33]. Usually, plasma based polymerization is applied in combination with sputtering [61, 63–65] or evaporation [33, 58] of the metallic components and allows for the production of metal-polymer nanocomposites with tunable metallic filling factors [65] and remarkable electrical and optical properties [58, 65, 66]; a report about a nanocomposite of small Au particles dispersed in a C_3F_8 polymer matrix which spans twelve magnitudes of electrical resistivity ranging from $10^{-6}\,\Omega\,\mathrm{cm}$ to $10^{6}\,\Omega\,\mathrm{cm}$ can be found in Ref. [65].

The effect of plasma polymerization is known since the 1870s but was primarily perceived as a byproduct associated with the gas discharge [67]. From then on, it took almost one hundred years until the first attempts to utilize plasma polymerization for the deposition of thin films emerged in the 1960s [67, 68]. Stemming from their unique physical properties, an enhanced interest in plasma based synthesis of organotin polymers[1] arose [69, 70] and the first attempts to incorporate metallic components into a plasma polymer emerged in the 1970s [66, 71] and initialized an intensive exploration of plasma polymerization based metal-polymer nanocomposite production in the following years [60].

Sputter Deposition

Metal-polymer nanocomposite fabrication based on sputter deposition involves the decomposition of either the metal or both the metal and the polymer from a solid target into atoms or molecules [72] driven by ion or atom bombardment. The target is located near a substrate such that the liberated atoms can condense on the surface of the substrate and form a thin film.

Sputter deposition is employed in many different variants of which the most promising for nanocomposite fabrication is magnetron sputtering. Magnetron sputtering is an extension of the basic cathode sputtering process which has many limitations such as low deposition rates, low ionization rates in the plasma, and substrate heating effects [73]. These restrictions could be overcome by the invention of magnetron sputtering.

As already mentioned above, magnetron sputtering was first applied in conjunction with plasma polymerization at the end of the 1970s [63]; radio frequency (RF) magnetron sputtering of both metal and polymer was invented in 1983 [64].

As its name implies, the draft horse of magnetron sputtering techniques is a plasma based magnetron discharge which was invented in the 1930s [74] and received the form of contemporary magnetron sputtering assemblies in the 1960s [75, 76]. The essential component of a magnetron discharge system is the negative biased cathode [75] whose electrical field is superimposed by a magnetic field maintained by permanent magnets located underneath the cathode, see Fig. 2.8. The basic process is the generation of charged ions by a plasma discharge. These ions are accelerated towards the cathode and liberate atoms of the target by impact. The process gas is typically an inert gas, such as the noble gas argon, at a pressure between 0.1 and 5 Pa [73, 76, 77]. The ion

[1] Organotin polymers are polymers involving chemical compounds based on tin.

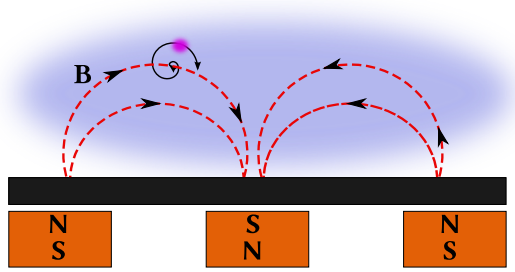

Figure 2.8: *Schematic illustration of the basic structure of a magnetron discharge including the electron trap region above the cathode. Secondary electrons are confined in the trap region by the combined action of the magnetic and the electric field and move on cycloid paths (which is suggested by the spiral around the magnetic field lines). The electric field lines are not depicted.*

impact also results in the emission of secondary electrons that are accelerated away from the cathode and confined in the *electron trap region* which constrains the electron motion to the vicinity of the target [73, 75]. The electron trap region is the area where the electrical field of the cathode and the magnetic field of the two coaxial magnets superimpose. The arrangement of the two magnets creates a magnetic field projecting into the space front of the cathode with an alignment parallel to the surface of the cathode. The magnetic field forces the electrons on a spiral path which substantially increases the probability of ionizing electron-atom collisions, thus allowing for a working pressure which is typically one magnitude lower compared to conventional cathode sputtering. Conversely, the increased ionization rate due to confined secondary electrons results in an enhanced ion flow towards the cathode giving higher sputter rates. Typical secondary electron emission coefficients lie around 5% [75]. Magnetron sputtering, as also sputtering in general, falls into two broad categories, direct current (DC) sputtering and radio frequency (RF) sputtering, depending on weather the cathode is biased with DC or alternate current (AC) voltage. The operation frequency of RF sputtering mostly lies around the free radio frequency 13.56 MHz, hence the name RF sputtering.

For polymer targets, RF sputtering is commonly used [77], which leads to crosslinked polymers [78]. Metals are commonly sputtered with DC magnetron discharges [33], except for magnetic metals for which RF sputtering is used [33]. An important criterion for the suitability of polymer sputtering is the sputter rate which sensitively depends on the polymer. Teflon, for example, was found to exhibit a sputter rate which is orders of magnitude higher than for most other polymers [79].

Cluster Sources

Cluster sources are apparatuses capable of producing free cluster beams with narrow size distributions. The first attempts to produce cluster beams by means of cluster sources were reported in the beginning of the 1980s [80]. The basic mechanism of cluster sources is to produce a metal vapor which is guided into a region with a flowing gas with relatively high pressure between 10 and 100 Pa [81, 82]. The flowing gas fulfills two purposes: first, it decelerates and cools the metal atoms and carries them through the apparatus until they are ejected through an orifice. Secondly, it ignites the cluster growth process by acting as a catalyst for dimer formation which is only possible by three-body collisions between two metal atoms and a gas atom [83]. Once the nucleation of di-atomic clusters in ignited, small clusters C_n grow by atomic attachment, $C_n + C_1 \rightarrow C_{n+1}$; larger clusters may also grow from cluster-cluster collisions, $C_n + C_m \rightarrow C_{n+m}$ [82].

The metal vapor can be produced my different means; the earliest approaches were thermal evaporation [80, 84, 85] and laser ablation [86, 87]. In the beginning of the 1990s, the first attempt to build cluster sources based on magnetron sputtering emerged [81]. A major advantage of cluster sources utilizing magnetron discharges is the uniformity of the discharge current, allowing, even at large cathode dimensions, for the production of homogeneous metal vapors in a large volume which significantly reduces attachment of metal atoms to the chamber wall [82]. Sputter discharge can also be used to ionize clusters [81].

2.3.2 Chemical Approaches

Chemical approaches are a popular class of techniques for nanocomposite fabrication and thin solid films in general. They offer good control of the nanoparticle size distribution [13, 88] and a reliable stabilization of metal clusters in the polymer matrix [13]. The general mechanism of chemical deposition techniques is to induce a chemical reaction of a precursor in the vicinity of a wafer surface. During this chemical reaction, the precursor leaves a solid layer on the wafer surface. Chemical approaches are classified according to the phase of the precursor.

Chemical Vapor Deposition

Chemical deposition techniques with gas-phase precursors are summarized under the label chemical vapor deposition (CVD) and are often used in semiconductor industry. A necessary prerequisite is that volatile compounds of the precursor exist which deposit the

desired solid-phase film on the wafer during the reaction process. The energy required to maintain the chemical reaction can be supplied in different forms, the most common of which is heat, but also other energy forms such as electrical discharge (plasma enhanced chemical vapor deposition (PECVD)) or photons (photon induced chemical vapor deposition (PHCVD)) are in use. A major advantage of CVD is to enable high deposition rates and the generation of thick coatings [89]. But CVD has also several disadvantages the most serious of which are high process temperatures and the need of precursors with high vapor pressure which are often hazardous and lead to toxic by-products of the chemical reaction [89].

Wet Chemical Techniques

Metal-polymer nanocomposites can also be fabricated using wet chemical approaches [31, 88, 90]. Wet chemical techniques rely on the use of liquid precursors and cover a broad spectrum of methods. Prominent examples of wet chemical techniques are spin coating [91, 92] and chemical solution deposition (CSD) methods, also known as *sol-gel* methods.

Spin coating is a procedure whereby the coating material is brought on a rotating disc and ejected by centrifugal force resulting in the coverage of the wafer disc with a thin film. It provides good control of the resulting film thickness and is often used to generate highly uniform polymer films covering large areas ($\varnothing \geq 30$ cm) [92].

The sol-gel process is used to generate a solid material from a colloidal solution and is widely adopted for processing inorganic ceramics and glass materials [93]. The sol-gel process starts with the generation of a colloidal solution (sol) consisting of nm-sized precursor particles dissolved in a host liquid. By condensation of the precursor particles, the solution evolves towards a di-phasic gel-like structure consisting of a polymeric network of the precursor and the remaining liquid implemented in the pores of the gelation network. After gelation, the remaining liquid is removed by a drying process which has a significant influence on the final texture of the remaining component [13] and is often performed under hypercritical conditions [93] in order to reduce the surface tension of the liquid. This technique allows for nanocomposite fabrication in different ways, depending on the stage at which the filler particles of the nanocomposite are added into the process [26]. Metal-polymer nanocomposites can be processed with *in situ* and *ex situ* approaches [33]. In the first case, metallic nanoparticles are formed within a polymer solution. In the ex situ process, nanoparticles with desired properties

are generated separately and added to the solution afterwards. In both case, the clusters are incorporated into the nanocomposite during the gelation process.

2.4 Computer Simulations of Metal-Polymer Nanocomposites

Computer simulations of metal-polymer nanocomposites divide into two main branches: Monte Carlo (MC) simulations and Molecular dynamics (MD) simulations. While MC methods are mainly applied to describe macroscopic phenomena during formation of nanocomposites, MD simulations are preferably used to explore transport and growth processes on an atomistic scale.

The first attempts to support experimental observations of metal-polymer interfaces by means of MC simulations based on the Metropolis algorithm [94] were reported by LeGoues et al. [18]. The aim of these studies was to reproduce and to explain the morphology of cluster growth and diffusion in a Cu/Ni-polyimide interface investigated with cross-sectional TEM. Therefore, LeGoues et al. idealized the interface as a two-dimensional grid with several interaction sites representing the polymer which had the effect to bind atoms at nearest neighbor sites. To incorporate the dynamics of the polymer as well as the dynamics of the metal, the interaction sites were allowed to move along the grid. The purpose of these simulations was to determine the influence of the deposition rate on the interface formation. A similar model involving a three-dimensional grid was used in simulations by Faupel et al. [95] and Silverman [96].

The simulations implemented during this work combine several approaches of previous simulations. The basic assumptions were introduced by Thran et al. who dropped the restrictions of a grid and investigated the interplay of diffusion and aggregation of metal clusters within a continuous space scheme by means of KMC simulations [22, 24]. In this work, this model is adopted and extended by the introduction of monomer evaporation and the integration of the interrupted coalescence model (ICM) by Yu et al. [21]. The main feature of the ICM is to stop equilibration of clusters if they exceed a certain size, enabling simulations of systems undergoing a percolation transition. Furthermore, co-deposition of metal and polymer was implemented as well as a second growth mechanism to simulate the growth of metallic nanocolumns during co-deposition [97]. A Detailed description of the simulations can be read in Chap. 4.

Recently, Khan et al. performed lattice based atomistic KMC simulations of the growth of Au nanorods in a Au-silica nanocomposite produced by co-deposition [98]. The simulations Khan et al. developed, allowed for an incorporation of local surface

heating effects due to impact of energetic atoms and highlighted the role of surface diffusion assisted phase separation for the growth of columnar structures.

Besides, MC models have also been utilized to study the formation of thin films covering all morphological stages reaching from compact island growth [99] to percolation [21, 23, 100, 101]. For these simulations, the Family and Meakin model (FMM) [99, 102] has established itself as the standard model for clusters.

In order to investigate nanocomposite formation on microscopic time and length scales, MD simulations have been applied since the early 1990s [103–108]. Mostly, the main purpose of these simulations is to obtain diffusion coefficients of metal particles by evaluating their trajectories. Particular worthy of mention is a report of Haberland who studied the effects of energetic impact of clusters on surfaces and thin films by means of MD simulations [108].

CHAPTER 3

Theoretical Foundations of Kinetic Monte Carlo Methods

Statistical physics deals with the description of macroscopic systems within the framework of probability theory. One of the main problems physicists have to address is to develop appropriate mathematical models incorporating the large number of degrees of freedom that are crucial for the behavior of the described system. While quantum mechanical methods and molecular dynamics provide powerful tools to a variety of physical processes on microscopic time and length scales, these methods can —despite of an enormous methodological and computational progress in the last decades— not be applied to macroscopic systems ($N \propto 10^{23}$). This is not only due to the limitations of contemporary computers but mainly to the principal impossibility to detect the initial conditions of all particles constituting a macroscopic physical system. Therefore, statistical physics is a theory of fundamental importance for physics in general and other sciences as well because it builds a bridge between the microscopic physical laws on the one side and macroscopic phenomena on the other. It is established on a combination of fundamental microscopic physical laws, mathematical methods of probability theory, asymptotic statistics (such as the law of large numbers) and a few fundamental physical postulates.

One important class of algorithms in statistical physics is summarized under the label Monte Carlo methods [109] and can be applied to a large number of stochastic processes not only in physics but also in numerical mathematics [110], biology [111, 112],

and economics [113, 114], to name a few.

What all Monte Carlo methods have in common is the use of random numbers. The basic idea of using some kind of random process (which is quite similar to the use of random numbers), in order to get insight into a given problem is quite old; in 1777, Georges-Louis Leclerc de Buffon outlined an experiment allowing for an estimation of π, involving repeatedly dropping needles on a floor made of parallel strips of wood (or a sheet of lined paper) and observing how often the needle intersects a line between two strips [115, 116].

The modern version of the Monte Carlo method, which is based on the use of computer generated random numbers, was invented by Stanisław Marcin Ulam in the 1940s during his work on nuclear weapon projects at the Los Alamos National Laboratory [117]. It was given its name by Nicholas Metropolis, alluding to the famous Monte Carlo Casino, where S. Ulam's uncle often gambled [117]. The first Monte Carlo program was implemented by John von Neumann and carried out on the ENIAC (Electronic Numerical Integrator And Computer) in the late 1940s under the supervision of N. Metropolis [117, 118]. The aim of these studies was to study the problem of neutron diffusion in fissionable materials [109, 117].

One of the basic mathematical tools used in Monte Carlo methods is given by the Markov chain method which is applicable both to systems in and out of equilibrium as long as they obey the so-called Markov property. The most famous application of Markov chains and the Monte Carlo method in general is probably the Metropolis algorithm [94], which was developed by N. Metropolis and co-workers in the early 1950s in order to generate ensembles of physical systems in thermodynamic equilibrium distributed according to the Boltzmann distribution [119]. Twenty years later, the Metropolis algorithm was extended to what is nowadays known as the Metropolis-Hastings algorithm, which can generate ensembles according to arbitrary distributions [120].

Markov chain methods can be divided into two main branches: discrete-time methods and continuous-time methods. While discrete-time Markov chains (DTMCs) mainly find application in simulations of systems in thermodynamic equilibrium, continuous-time Markov chains (CTMCs) can be applied to model the time development of physical systems out of equilibrium. The CTMC method therefore provides the mathematical and theoretical foundation of the KMC method as it was invented by A. Bortz and co-workers in the 1970s [20], as well as several other algorithms built upon it.

This chapter gives a brief introduction into the concept of CTMCs and the underlying basics of probability theory. Furthermore, it provides a discussion of the KMC method as

described in [20] and an algorithm based on the first reaction (FR) method, introduced by D. Gillespie [121–123], that was used during this work.

3.1 Fundamental Terms of Probability Theory

In this section, the basic concepts of probability theory that are necessary to understand the notion of Markov chains are introduced. For a comprehensive discussion of probability theory and Markov chains the reader is referred to [124, 125].

3.1.1 Probability Space

The basic mathematical concept to formally describe random processes is given by the *probability space* which is defined as a triple (Ω, Σ, P) consisting of

1. a sample space Ω containing all possible outcomes of an observation.
2. a set of events[1] $\Sigma \subset \beta(\Omega)$ ($\beta(\Omega)$ denotes the power set of Ω) consisting of subsets of Ω. Σ is a σ-algebra, i.e.
   a) Σ is nonempty : $\exists\, \mathcal{A} \subset \Omega : \mathcal{A} \in \Sigma$.
   b) Σ is closed under complementation : $\mathcal{A} \in \Sigma \Longrightarrow \mathcal{A}^c := \Omega \backslash \mathcal{A} \in \Sigma$.
   c) Σ is closed under countable unions : $\mathcal{A}_1, \mathcal{A}_2, \ldots \in \Sigma \Longrightarrow \cup_{i\in\mathbb{N}} \mathcal{A}_i \in \Sigma$.
3. a probability measure $P : \Sigma \to \mathbb{R}_0^+$ satisfying the *Kolmogorow* axioms:
   a) $0 \leq P(\mathcal{A}) \leq 1 \quad \forall \mathcal{A} \in \Sigma$.
   b) $P(\Omega) = 1$.
   c) for every set of pairwise disjoint events $\{\mathcal{A}_i\}_{i\in\mathcal{I}}$ it is

$$P(\cup_{i\in\mathcal{I}}\mathcal{A}_i) = \sum_{i\in\mathcal{I}} P(\mathcal{A}_i). \tag{3.1}$$

[1] Note that an elementary outcome $\omega \in \Omega$ is not an event in the sense of the definition. An event is rather a set of elementary outcomes. In the case of discrete probability spaces with countable sample spaces Ω it is common to choose $\beta(\Omega)$ as the set of events such that every elementary outcome $\omega \in \Omega$ can be identified with the singleton $\{\omega\}$. In the following, only discrete probability spaces will be considered which renders the formal distinction between ω and $\{\omega\}$ redundant.

The axiomatic foundation of probability theory in terms of probability spaces was performed by Andrei Kolmogorow in the 1930s and can heuristically be interpreted by the notion of probability as the empirical frequency of the occurrence of a given event in the limit of sufficiently many performances of the experiment, as it was introduced by Pierre-Simon Laplace in his *Essai philosophique sur les probabilités* in 1814 [126]: if N independent experiments are performed and event $\mathcal{A}$ occurs $N_\mathcal{A}$ times, the empirical frequency is $f(\mathcal{A}) = N_\mathcal{A}/N$ and corresponds to the probability of the occurrence of event $\mathcal{A}$.

3.1.2 Random Variables

A central task in physics is the quantitative description of system properties in terms of a set of arbitrary observables which are usually represented by mathematical objects like numbers, vectors and so on. In statistical physics, the formal integration of this mapping of system states onto mathematical objects is provided by so called *random variables*: A real-valued random variable[2] is a function $X : \Omega \to \mathbb{R}$ such that

$$\{X \leq a\} := \{\omega \in \Omega \,|\, X(\omega) \leq a\} \in \Sigma \quad \forall a \in \mathbb{R}. \tag{3.2}$$

3.1.3 Independence, Conditional Probability, and the Markov Property

Independence

Consider two events $\mathcal{A}$ and $\mathcal{B}$ of an arbitrary probability space. $\mathcal{A}$ and $\mathcal{B}$ are defined to be stochastically independent if the occurrence of $\mathcal{A}$ does not affect the probability of the occurrence of $\mathcal{B}$ and vice versa. In this case, the joint probability of the occurrence of $\mathcal{A}$ *and* $\mathcal{B}$ is given by the product of their probabilities:

$$P(\mathcal{A} \cap \mathcal{B}) = P(\mathcal{A})P(\mathcal{B}). \tag{3.3}$$

This property can directly be transferred to random variables: two random variables X and Y are defined to be independent if

$$P(X \leq a, Y \leq b) = P(X \leq a)P(X \leq b) \quad \forall a, b \in \mathbb{R}. \tag{3.4}$$

Here, a general notation scheme, that will be used throughout this work, has been introduced: $P(X \leq a) := P(\{X \leq a\})$, where the shorthand notation of Def. (3.2) is

[2] In the following, the prefix real-valued will be omitted since only real-valued random variables will be considered.

used. Also, on the left-hand side of Eq. (3.4), the notation scheme of commas replacing intersection signs[3] is used: $P(\mathcal{A}, \mathcal{B}) \equiv P(\mathcal{A} \cap \mathcal{B})$.

Conditional Probability

The *conditional probability* $P(\mathcal{A} \mid \mathcal{B})$ represents the probability of event $\mathcal{A}$ to occur on the condition that event $\mathcal{B}$ already occurred:

$$P(\mathcal{A} \mid \mathcal{B}) := \frac{P(\mathcal{A} \cap \mathcal{B})}{P(\mathcal{B})}. \tag{3.5}$$

This definition can be easily understood in terms of probability as relative frequencies, as described in Sec. 3.1.1: on the condition that event $\mathcal{B}$ already occurred, the relative frequency of $\mathcal{A}$ reads $N_{\mathcal{A}\cap\mathcal{B}}/N_{\mathcal{B}} = P(\mathcal{A} \cap \mathcal{B})/P(\mathcal{B})$.

Markov Property for Events

The *Markov property* is the key concept of the theory of Markov chains and represents the characteristic memoryless property of random processes. If two events $\mathcal{A}$ and $\mathcal{C}$ are conditionally independent given another event $\mathcal{B}$, i.e.

$$P(\mathcal{A} \cap \mathcal{C} \mid \mathcal{B}) = P(\mathcal{A} \mid \mathcal{B}) P(\mathcal{C} \mid \mathcal{B}), \tag{3.6}$$

then

$$\begin{aligned} P(\mathcal{C} \mid \mathcal{A}, \mathcal{B}) = \frac{P(\mathcal{A} \cap \mathcal{B} \cap \mathcal{C})}{P(\mathcal{A} \cap \mathcal{B})} &= \frac{P(\mathcal{A} \cap \mathcal{C} \mid \mathcal{B}) P(\mathcal{B})}{P(\mathcal{A} \cap \mathcal{B})} \\ &\overset{(3.6)}{=} \frac{P(\mathcal{A} \mid \mathcal{B}) P(\mathcal{C} \mid \mathcal{B}) P(\mathcal{B})}{P(\mathcal{A} \cap \mathcal{B})} = P(\mathcal{C} \mid \mathcal{B}). \end{aligned} \tag{3.7}$$

Eq. (3.7) is called the Markov property for events.

3.1.4 The Law of total Probability and Bayes Sequential Formula

From the definition of the conditional probability, Eq. (3.5), two important conclusions can be deduced. Consider the events $\mathcal{B}_1, \ldots, \mathcal{B}_n$ to be a partition[4] of a given event set

[3] This notation will mainly be used in the context of Markov chains and corresponds to that propagated in the relevant literature.

[4] A collection of pairwise disjoint sets overlapping the whole event set Σ.

Σ. Then it follows from $\mathcal{A} = \cup_{i=1}^{n}(\mathcal{A} \cap \mathcal{B}_i)$, Def. (3.5), and the third Kolmogorow axiom, Eq. (3.1), the *law of total probability*

$$P(\mathcal{A}) = \sum_{i=1}^{n} P(\mathcal{A} \,|\, \mathcal{B}_i) P(\mathcal{B}_i). \tag{3.8}$$

The law of total probability expresses the probability of the occurrence of event $\mathcal{A}$ in terms of the realization of several distinct events.

The other conclusion is known under the name *Bayes sequential formula*. For any collection of events $\mathcal{A}_1, \ldots \mathcal{A}_n$ it holds

$$\begin{aligned} P(\cap_{i=1}^{n}\mathcal{A}_i) &= P(\mathcal{A}_1) \cdot \frac{P(\mathcal{A}_1 \cap \mathcal{A}_2)}{P(\mathcal{A}_1)} \cdot \frac{P(\mathcal{A}_1 \cap \mathcal{A}_2 \cap \mathcal{A}_3)}{P(\mathcal{A}_1 \cap \mathcal{A}_2)} \cdot \ldots \cdot \frac{P(\cap_{i=1}^{n}\mathcal{A}_i)}{P(\cap_{i=1}^{n-1}\mathcal{A}_i)} \\ &= P(\mathcal{A}_1) \prod_{i=2}^{n} P(\mathcal{A}_i \mid \cap_{k=1}^{i-1} \mathcal{A}_k). \end{aligned} \tag{3.9}$$

3.1.5 Stochastic Processes

The formalism of stochastic processes provides the basis for the description of time ordered random processes, or in other words, the time evolution of a random variable. Formally, a stochastic process in continuous time is defined as a collection $\{X_t\}_{t\in\mathbb{R}^+}$ of random variables defined on a given probability space (Ω, Σ, P) which is indexed by a continuous parameter t.

3.1.6 Distribution Function, Probability Density and Expectation Value

Cumulative Distribution Function

The cumulative distribution function (CDF) $F_X(x)$ represents the probability of sampling a random variable X with a value smaller than or equal to x:

$$F_X(x) := P(X \leq x). \tag{3.10}$$

The CDF has the following properties:

1. $F_X(x) : \mathbb{R} \to [0, 1]$.

2. F_X is nondecreasing.

3. $\lim_{x\to-\infty} F_X(x) = 0, \quad \lim_{x\to\infty} F_X(x) = 1.$

4. F_X is right-continuous.

5. $P(X = a) = F_X(a) - F_X(a-), \quad F_X(a-) := \lim_{h\to 0} F_X(a-h).$

6. $P(a < X \leq b) = F_X(b) - F_X(a).$

Probability density

In case of continuous random variables, the CDF can be written as an integral, using the probability density function (PDF) $f_X(x)$:

$$F_X(x) = \int_{-\infty}^{x} f_X(x')\,\mathrm{d}x'. \tag{3.11}$$

From Eq. (3.11) and (3.10), one can immediately deduce two main properties of the PDF:

1. $\int_{-\infty}^{\infty} f_X(x')\,\mathrm{d}x' = 1.$

2. $P(a < X \leq b) = \int_{a}^{b} f_X(x')\,\mathrm{d}x'.$

Expectation Value

The *expectation value* $\mathrm{E}[X]$ is the weighted average of all possible values a random variable can hold. For the most frequent cases of absolutely continuous random variables the expectation value is defined as

$$\mathrm{E}[X] = \int_{-\infty}^{\infty} f_X(x)x\,\mathrm{d}x. \tag{3.12}$$

Note that this definition does not imply the expectation value to be the value with the highest probability.

3.1.7 The Exponential Distribution

Definition

The *exponential distribution* is a class of continuous distribution functions and of great importance for the modeling of processes in which events occur continuously and independently at a constant averaged rate. Commonly, the exponential distribution is defined via its probability density function:

$$f_X(x;\lambda) = \begin{cases} \lambda \exp(-\lambda x) & x \geq 0 \\ 0 & x < 0, \end{cases} \tag{3.13}$$

where λ is the parameter of the distribution and usually called the rate parameter.

Some properties of the exponential distribution which are referred to in the following are

1. $\mathrm{E}[X] = \frac{1}{\lambda}$.

2. $F_X(x;\lambda) = P(X \leq x) = 1 - \exp(-\lambda x)$.

3. $P(X > x) = 1 - F_X(x;\lambda) = \exp(-\lambda x)$.

The key feature which makes the exponential distribution important for many applications is its memorylessness: the distribution of an exponentially distributed random variable X conditioned on $\{X > u\}$ is again exponential with the same rate parameter:

$$\begin{aligned} P(X > t + u \,|\, X > u) &= \frac{P(X > t+u)}{P(X > u)} = \frac{\exp(-\lambda(t+u))}{\exp(-\lambda u)} \\ &= \exp(-\lambda t) = P(X > t). \end{aligned} \tag{3.14}$$

It can easily be shown that the exponential distribution is the only distribution fulfilling the memoryless property.

Another important property of the exponential distribution, which is crucial for the applicability of the Bortz-Kalos-Lebowitz (BKL) algorithm, is the fact that the *distribution of the minimum of independent exponentially distributed (i.e.d.)* random variables is again exponential. Consider $\{X_i\}_{i\in\mathcal{I}}, \mathcal{I} = 1, \ldots, n$ to be i.e.d. random variables with

corresponding rate parameters $\{\lambda_i\}_{i\in\mathcal{I}}$. Then, One obtains

$$P(\min\{X\}_{i\in\mathcal{I}} > x) = P(\cap_{i=1}^{n}\{X_i > x\}) = \prod_{i=1}^{n} P(X_i > x)$$
$$= \exp\Big(-x\sum_{i=1}^{n}\lambda_i\Big), \tag{3.15}$$

which proves the statement.

The so-called *competition theorem* is complementary to the distribution of the minimum of i.e.d. random variables and provides the distribution of the index of the random variable which achieves the minimum in Eq. (3.15). Again, $\{X_i\}_{i\in\mathcal{I}}$ are i.e.d. random variables with corresponding rate parameters $\{\lambda_i\}_{i\in\mathcal{I}}$. Define $K := j$ if $X_j = \min\{X_i\}_{i\in\mathcal{I}}$ and $U := \min\{X_i\}_{i\in\mathcal{I}\setminus\{K\}}$. Further, put $f_u(u) = \lambda_u \exp(-\lambda_u u)$ with $\lambda_u = \sum_{i\in\mathcal{I}\setminus\{K\}}\lambda_i$. Then the distribution $P(K = j)$ reads

$$P(K=j) = \lim_{x\to\infty} P(X_j < U, X_j < x) = \lim_{x\to\infty}\int_0^x \Big(\int_y^\infty f_u(u)\,\mathrm{d}u\Big)\lambda_j\exp(-\lambda_j y)\,\mathrm{d}y$$
$$= \lim_{x\to\infty}\lambda_j\int_0^x \exp(-y\sum_{i=1}^{n}\lambda_i)\,\mathrm{d}y = \frac{\lambda_j}{\sum_{i=1}^{n}\lambda_i}. \tag{3.16}$$

Eq. (3.15) and (3.16) provide the basic components of algorithms for the numerical treatment of CTMCs.

3.2 Continuous-Time Markov Chains

3.2.1 Basic Definitions

A Markov chain is the mathematical model of a system undergoing transitions from one state to another in a countable set of states. In contrast to discrete-time Markov chains where no transition times are defined, continuous-time Markov chains are processes including a distribution function for the time interval between two transitions. Formally, a CTMC is defined as a stochastic process $\{X_t\}_{t\in\mathbb{R}^+}$ on a countable[5] sample space $\Omega = \{\omega_1, \ldots, \omega_k\}$ such that:

[5] In this work, only finite sample spaces are considered.

1. The sample paths $t \to X_t$ are right-continuous step functions.

2. The process $\{X_t\}_{t\in\mathbb{R}^+}$ fulfills the *Markov property*, that is

$$P(X_{t+u} = \omega_j \,|\, X_t = \omega_i, \cap_{s=1}^{n}\{X_{t_s} = \omega_{i_s}\}) = P(X_{t+u} = \omega_j \,|\, X_t = \omega_i) \quad (3.17)$$

for all $\omega_j, \omega_i, \omega_{i_1}, \ldots, \omega_{i_n} \in \Omega$ and any nondecreasing sequence of times $0 \leq t_1 \leq t_2 \leq \ldots \leq t_n \leq t \leq t+u$.

Condition (1) ensures that no explosions occur, i.e. in every time interval Δt, only a finite number of transitions can occur. Condition (2) states that at any time the future of the Markov process is only affected by its current state and not by the sequence of states that preceded it.

A special class of Markov chains, which is of importance for this work, are *time homogeneous* Markov chains. Time homogeneous Markov chains are characterized by an isotropic distribution of transition times, i.e. for all $\omega_i, \omega_j \in \Omega$ and any $0 \leq u \leq t$ it is

$$P(X_{t+u} = \omega_j \,|\, X_t = \omega_i) = P(X_t = \omega_j \,|\, X_{t-u} = \omega_i). \quad (3.18)$$

The time evolution of a Markov chain is described by the transition matrix $\mathbf{P}(t) = \{p_{ij}(t)\}_{\omega_i,\omega_j\in\Omega}$,

$$p_{ij}(t) := P(X_{u+t} = \omega_j \,|\, X_u = \omega_i), \quad \lim_{\varepsilon\to 0^+} \mathbf{P}(\varepsilon) = \mathbb{1}, \quad (3.19)$$

which is a continuous function of t. Here it is important to realize that the entry $p_{ij}(t)$ of the transition matrix just renders the probability to find the system in state ω_i at any given time u and in state ω_j a time interval t later. Note that the process does not necessarily evolve directly from state ω_i to state ω_j; instead, it can evolve from state ω_i to state ω_j by occupying an arbitrary number of states in between the time interval t.

The distribution of states is governed by the time-dependent probability vector

$$\mathbf{w}(t) = \big(w_i(t), \ldots, w_k(t)\big), \quad w_i(t) := P(X_t = \omega_i), \quad (3.20)$$

which can be computed, once the transition matrix and the initial distribution $\mathbf{w}(t=0)$ are known, by applying the law of total probability, Eq. (3.8),

$$\begin{aligned} w_i(t) &= P(X_t = \omega_i) = \sum_j P(X_t = \omega_i, X_0 = \omega_j) \\ &= \sum_j P(X_0 = \omega_j) P(X_t = \omega_i \,|\, X_0 = \omega_j) = \sum_j w_j(0) p_{ji}(t) \\ &\Longrightarrow \mathbf{w}(t) = \mathbf{w}(0)\mathbf{P}. \end{aligned} \quad (3.21)$$

Here, the notation $\sum_i \equiv \sum_{i,\omega_i \in \Omega}$ was introduced for better readability. In line with this notation, the abbreviation $\sum_{i \neq j} \equiv \sum_{i,\omega_i \neq \omega_k}$ will also be used in the following.

Under the same conditions, the probability of an evolution path, i.e. a sequence of occupied states at fixed times, can be computed by applying Bayes sequential formula, Eq. (3.9), in combination with the law of total probability, Eq. (3.8):

$$\begin{aligned} P(X_{t_1} = \omega_{i_1}, \ldots, X_{t_n} = \omega_{i_n}) &= \sum_j P(X_{t_0=0} = \omega_j, X_{t_1} = \omega_{i_1}, \ldots, X_{t_n} = \omega_{i_n}) \\ &= \sum_j P(X_0 = \omega_j) \prod_{k=1}^{n} P(X_{t_k} = \omega_{i_k} \mid \cap_{l=0}^{k-1} \{X_{t_l} = \omega_{i_l}\}) \\ &= \sum_j w_j(0) \prod_{k=1}^{n} P(X_{t_k} = \omega_{i_k} \mid X_{t_{k-1}} = \omega_{i_{k-1}}) \\ &= \sum_j w_j(0) \prod_{k=1}^{n} p_{i_{k-1},i_k}(t_k - t_{k-1}), \quad \omega_0 \equiv \omega_j. \end{aligned} \tag{3.22}$$

3.2.2 Key Properties of Continuous-time Markov Chains

The Chapman-Kolmogorow Equation

One central equation containing the key property of the transition matrices $\mathbf{P}(t)$ is the *Chapman-Kolmogorow equation* which renders the transition probability from state ω_i to state ω_j as the sum of all possible ways with intermediate states ω_k in between:

$$\begin{aligned} p_{ij}(t+u) &= P(X_{t+u} = \omega_j \mid X_0 = \omega_i) \\ &= \sum_k P(X_{t+u} = \omega_j, X_t = \omega_k \mid X_0 = \omega_i) \\ &= \sum_k P(X_{t+u} = \omega_j \mid X_t = \omega_k, X_0 = \omega_i) P(X_t = \omega_k \mid X_0 = \omega_i) \\ &= \sum_k p_{kj}(u) p_{ik}(t) \quad \Longleftrightarrow \quad \mathbf{P}(t+u) = \mathbf{P}(t)\mathbf{P}(u). \end{aligned} \tag{3.23}$$

Thus, the transition matrices obey the exponentiation identity

$$\mathbf{P}\Big(\sum_{i=1}^{n} t_i\Big) = \prod_{i=1}^{n} \mathbf{P}(t_i), \tag{3.24}$$

which follows from Eq. (3.23) by induction.

Two Properties of Transition Times

As stated in the beginning of Sec. 3.2.1, the main extension of CTMCs compared to DTMCs, is the incorporation of transition times between two consecutive states. Consequently, one of the main questions is how the distribution of transition times can be computed. By making use of the Markov property, Eq. (3.17), it can be shown that the distribution of transition times fulfills the memoryless property. To prove this statement, consider the process to reach state ω_i at time t_i and let $\tau_i := \sup\{t \geq t_i \,|\, X_t = \omega_i\} - t_i$ denote the time interval after which the process transitions away from state ω_i. Then the event $\{\tau_i > u\}$ is equivalent to the event $\{X_s = \omega_i, s \in [t_i, t_i + u]\}$. By applying the Markov property, Eq. (3.17), and the definition of the time homogeneity, Eq. (3.18), one obtains[6]

$$\begin{aligned} P(\tau_i > u + t \,|\, \tau_i > u) &= P(X_s = \omega_i, s \in [t_i, t_i + u + t] \,|\, X_s = \omega_i, s \in [t_i, t_i + u]) \\ &= P(X_s = \omega_i, s \in [t_i + u, t_i + u + t] \,|\, X_{t_i+u} = \omega_i) \\ &= P(X_s = \omega_i, s \in [t_i, t_i + t] \,|\, X_{t_i} = \omega_i) \\ &= P(\tau_i > t). \end{aligned} \tag{3.25}$$

Thus, the distribution of transition times has the memoryless property implying that it is exponentially distributed with rate λ_i.

Another important property which requires a more formal proof (see e.g. [127]) is the independence of the transition time τ_i and the state ω_j the process reaches after the next transition:

$$P(X_{\tau_i} = \omega_j \,|\, \tau_i \leq t, X_0 = \omega_i) = P(X_{\tau_i} = \omega_j \,|\, X_0 = \omega_i) =: a_{ij}. \tag{3.26}$$

To distinguish this definition from the definition of the transition matrix, Eq. (3.19), one has to recall that τ_i denotes the time interval the process needs to leave state ω_i and not an arbitrary time interval as in Eq. (3.19).

[6] Strictly speaking, the argumentation is not completely correct because the Markov property, Eq. (3.17), only holds for finite sequences of states. For a rigorous proof, the reader is referred to [127].

3.2.3 The Q-Matrix

Having stated that the transition times of CTMCs are exponentially distributed, the remaining question is how the transition from one state to another can be computed. It can be shown that for every transition $\omega_i \to \omega_j$ a rate λ_{ij} can be constructed, giving rise to the notion of a CTMC as a sequence of competing transitions with exponentially distributed transition times. The corresponding rates are given by the entries of the *Q-matrix* (also called *infinitesimal generator*), $\mathbf{Q} = \{q_{ij}\}_{\omega_i,\omega_j\in\Omega}$, which is defined as

$$\mathbf{Q} := \lim_{\varepsilon\to 0^+} \frac{\mathbf{P}(\varepsilon) - \mathbf{P}(0)}{\varepsilon} = \lim_{\varepsilon\to 0^+} \frac{\mathbf{P}(\varepsilon) - \mathbb{1}}{\varepsilon}, \tag{3.27}$$

where $\mathbb{1}$ denotes the identity matrix. From the definition of the Q-matrix, it follows that the entries of the transition matrix can be written as a Taylor series,

$$p_{ij}(\varepsilon) = q_{ij}\varepsilon + \delta_{ij} + \mathcal{O}(\varepsilon^2), \quad \varepsilon > 0. \tag{3.28}$$

The diagonal elements of $\mathbf{Q}$ are given by

$$\begin{aligned} q_{ii} &= \lim_{\varepsilon\to 0^+} \frac{p_{ii}(\varepsilon) - 1}{\varepsilon} = \lim_{\varepsilon\to 0^+} \frac{\left(1 - \sum_{j\neq i} p_{ij}(\varepsilon)\right) - 1}{\varepsilon} = -\sum_{j\neq i} q_{ij} \\ &=: -q_i. \end{aligned} \tag{3.29}$$

By expanding the distribution of the transition time τ_i in a Taylor series, it can easily be shown that q_i is equal to the rate λ_i of the transition time τ_i. From Eq. (3.25), it follows that

$$P(\tau_i \leq \varepsilon) = 1 - \exp(-\lambda_i\varepsilon) = \lambda_i\varepsilon + \mathcal{O}(\varepsilon^2). \tag{3.30}$$

Alternatively, $P(\tau_i \leq \varepsilon)$ can be written in terms of the probability matrix $\mathbf{P}$,

$$\begin{aligned} P(\tau_i \leq \varepsilon) &= \sum_{j\neq i} P(X_\varepsilon = \omega_j \,|\, X_0 = \omega_i) = \sum_{j\neq i} p_{ij}(\varepsilon) \\ &\overset{(3.28)}{=} \sum_{j\neq i} q_{ij}\varepsilon + \mathcal{O}(\varepsilon^2) \overset{(3.29)}{=} q_i\varepsilon + \mathcal{O}(\varepsilon^2), \end{aligned} \tag{3.31}$$

where ε has to be sufficiently small in order to guarantee that only one transition (from ω_i to the subsequent state) occurs during the time interval ε. Equating the linear coefficients of Eqs. (3.30) and (3.31) yields

$$q_i = \lambda_i, \tag{3.32}$$

and thus

$$P(\tau_i \leq \varepsilon) = 1 - \exp(-q_i \varepsilon). \tag{3.33}$$

In order to work out the meaning of the off-diagonal elements of $\mathbf{Q}$, one has to use Eq. (3.28) and the definition of the transition matrix, Eq. (3.19). Again, ε is assumed to be sufficiently small, such that only one transition may occur during the time interval ε,

$$\begin{aligned} p_{ij}(\varepsilon) &= P(X_\varepsilon = \omega_j \,|\, X_0 = \omega_i) = P(X_{\tau_i} = \omega_j, \tau_i \leq \varepsilon \,|\, X_0 = \omega_i) \\ &= P(\tau_i \leq \varepsilon \,|\, X_0 = \omega_i) P(X_{\tau_i} = \omega_j \,|\, \tau_i \leq \varepsilon, X_0 = \omega_i) \\ &= P(\tau_i \leq \varepsilon) P(X_{\tau_i} = \omega_j \,|\, X_0 = \omega_i) \\ &= \left(q_i \varepsilon + \mathcal{O}(\varepsilon^2)\right) a_{ij} = q_i a_{ij} \varepsilon + \mathcal{O}(\varepsilon^2), \quad i \neq j. \end{aligned} \tag{3.34}$$

Here it is important to note that $P(\tau_i \leq \varepsilon \,|\, X_0 = \omega_i) \equiv P(\tau_i \leq \varepsilon)$ since the definition of the transition time already implies the process to be in state ω_i at $t = 0$, see Sec. 3.2.2. By equating the linear coefficients of Eqs. (3.28) and (3.34), one obtains

$$q_{ij} = q_i a_{ij} \implies a_{ij} = \frac{q_{ij}}{qi}, \quad i \neq j. \tag{3.35}$$

Eqs. (3.26), (3.33) and (3.35) are the key results of this section. They reveal that the entries of the Q-matrix determine both the transition time τ_i and the next transition $\omega_i \to \omega_j$ given a state ω_i:

$$\begin{aligned} &P(X_{\tau_i} = \omega_j, \tau_i \leq t \,|\, X_0 = \omega_i) \\ &\quad = P(\tau_i \leq t) P(X_{\tau_i} = \omega_j \,|\, X_0 = \omega_i) = (1 - \exp(-q_i t)) \, \frac{q_{ij}}{q_i}. \end{aligned} \tag{3.36}$$

In addition, comparison of Eq. (3.35) and the competition theorem, Eq. (3.16), suggests to interpret the off-diagonal elements q_{ij} of the Q-matrix as transition rates determining the time the process needs to reach state ω_j starting from ω_i.

3.2.4 Kolmogorow Equations, Master Equation

Backward and Forward Equations

The Q-matrix, as introduced above, allows for a local description of a CTMC in the sense that transitions from one state to another can be constructed. However, the Q-matrix also determines the global behavior of the CTMC which is governed by the transition matrix.

A. Kolmogorow derived a set of differential equations, called *Kolmogorow backward (BW) and forward equations (FW)*, connecting the transition matrix $\mathbf{P}$ with the Q-matrix:

$$\begin{aligned}\varepsilon^{-1}(p_{ij}(t+\varepsilon) - p_{ij}(t)) &= \sum_k \varepsilon^{-1}\left(p_{ik}(\varepsilon) - \delta_{ik}\right) p_{kj}(t) \\ &= \sum_k \varepsilon^{-1} p_{ik}(t)\left(p_{kj}(\varepsilon) - \delta_{kj}\right). \end{aligned} \tag{3.37}$$

By taking the limit $\varepsilon \to 0^+$, using Eq. (3.28), and assuming that the right-sided derivative of $\mathbf{P}$ exists for all $t \in \mathbb{R}^+$ and is continuous, one obtains a system of ordinary first-order differential equations

$$\frac{d}{dt}p_{ij}(t) = \sum_k q_{ik}p_{kj}(t) \quad \Longleftrightarrow \quad \frac{d}{dt}\mathbf{P}(t) = \mathbf{Q}\mathbf{P}(t) \quad \text{(BW)}, \tag{3.38}$$

$$\frac{d}{dt}p_{ij}(t) = \sum_k p_{ik}(t)q_{kj} \quad \Longleftrightarrow \quad \frac{d}{dt}\mathbf{P}(t) = \mathbf{P}(t)\mathbf{Q} \quad \text{(FW)}. \tag{3.39}$$

These differential equations are known as the Kolmogorow equations (also called the backward and forward equations, respectively). In case of finite sample spaces, the solution to these equations is given by the exponential of the Q-matrix:

$$\mathbf{P}(t) = \exp(t\mathbf{Q}) = \sum_{n=0}^{\infty} \frac{(t\mathbf{Q})^n}{n!}, \quad \mathbf{P}(0) = \mathbb{1}. \tag{3.40}$$

Master Equation

Based on the Kolmogorow forward equation, Eq. (3.39), it is possible to derive a set of differential equations for the probability vector $\mathbf{w}$(t), Def. (3.20),

$$\begin{aligned}\frac{d}{dt}p_{ij}(t) &= \sum_k p_{ik}(t)q_{kj} = -p_{ij}(t)q_j + \sum_{k\neq j} p_{ik}(t)q_{kj} \\ &= \sum_{k\neq j} p_{ik}(t)q_{kj} - \sum_{k\neq j} p_{ij}(t)q_{jk}. \end{aligned} \tag{3.41}$$

Using Eq. (3.21), multiplication with $w_i(0)$, and subsequent summation over i yields

$$\frac{d}{dt}w_j(t) = \sum_{k\neq j} w_k(t)q_{kj} - \sum_{k\neq j} w_j(t)q_{jk}. \tag{3.42}$$

Eq. (3.42) is known as the *master equation* and is the central equation of equilibrium Monte Carlo methods [120], where the focus lies on the construction of a transition matrix yielding a desired stationary equilibrium distribution, i.e $\frac{d}{dt}w_i(t) = 0$ for all i.

3.3 Two algorithmic Constructions of Continuous-Time Markov Chains

Having introduced the fundamentals of probability theory and the theory of continuous-time Markov chains in the previous sections, this section is devoted to the discussion of two algorithms for the construction of CTMCs. Both algorithms have in common that in each simulation step the knowledge of all possible transitions $\omega_i \to \omega_j, j \neq i$ and their corresponding rates $\{q_{ij}\}$ is required.

3.3.1 The Bortz-Kalos-Lebowitz Algorithm

The first algorithm to be discussed is the Bortz-Kalos-Lebowitz algorithm [20], also known as residence-time algorithm or the n-fold way. It mainly consists of two separate units. The first one is the building of the *embedded Markov chain* $\{X_n\}_{n\in\mathbb{N}}$ of the process:

$$X_n := X_{t_n}, \tag{3.43}$$

where $\{t_n\}_{n\in\mathbb{N}}$ denotes the sequence of transition times. The second one is the generation of the sequence of transition times. Due to the independence of the transition time and the subsequent transition path, Eq. (3.26), these two units can be treated separately.

Algorithm I (Bortz-Kalos-Lebowitz algorithm)

Initialization:

1. Set the initial time $t_0 = 0$.
2. Select the initial state X_0 according to an arbitrary initial distribution.

Simulation step:

1. Set up a list of all possible transitions $\omega_i \to \omega_j$ and their corresponding rates $\{q_{ij}\}$.
2. Compute the diagonal element $q_i = -\sum_j q_{ij} = -q_{ii}$ of the Q-matrix, where i labels the current state of the process.
3. Sample the residence time τ_n of the process in state ω_i from an exponential distribution with rate q_i and set $t_{n+1} = t_n + \tau_n$.

4. Sample the next transition $\omega_i \to \omega_j$ according to the probability distribution

$$P(X_{t_{n+1}} = \omega_j \,|\, X_{t_n} = \omega_i) = a_{ij} = \frac{q_{ij}}{q_i}. \tag{3.44}$$

5. Perform the transition $\omega_i \to \omega_j$ and continue with step 1.

With regard to random number sampling, the BKL algorithm is very efficient since it requires only two random numbers in each simulation step (step 3 and 4). However, In many cases, the most time-consuming part of this algorithm is the computation of the diagonal element q_i of the Q-matrix (step 2).

3.3.2 The First Reaction Method

The second algorithm to be covered is the first reaction method. It was invented by D. Gillespie in the 1970s in order to simulate the time evolution of coupled chemical reactions [121–123]. Mathematically, it is based on the formal equivalence of Eq. (3.35) and the competition theorem, Eq. (3.16): in Sec. 3.2.3 it was shown that the elements of the Q-matrix determine the local behavior of the CTMC:

$$P(X_{\tau_i} = \omega_j, \tau_i \leq t \,|\, X_0 = \omega_i) = (1 - \exp(-q_i t)) \, \frac{q_{ij}}{q_i}. \tag{3.45}$$

Combination of Eqs. (3.15) and (3.16) shows that Eq. (3.45) is formally equivalent to

$$\begin{aligned} P(\min\{X\}_{i\in\mathcal{I}} \leq x, K = j) &= P(\min\{X\}_{i\in\mathcal{I}} \leq x) P(K = j) \\ &= \left(1 - \exp(-x \sum_{i=1}^{n} \lambda_i)\right) \frac{\lambda_j}{\sum_{i=1}^{n} \lambda_i}, \end{aligned} \tag{3.46}$$

with K being defined as in Sec. 3.1.7.

As already suggested in Sec. 3.2.3, this equivalence allows for an interpretation of the time development of a CTMC as a competition of all possible transitions $\omega_i \to \omega_j, j \neq i$ in terms of competing i.e.d. random variables with rates q_{ij}. Instead of creating the embedded Markov chain and sampling the residence time independently from each other, as it is done within the BKL algorithm, it is possible to sample a transition time for every possible transition and choose the transition with the smallest residence time as the next transition and the corresponding time as the next transition time.

Algorithm II (first reaction method)
As in the BKL algorithm, $\{t_n\}_{n\in\mathbb{N}}$ denotes the sequence of transition times.

Initialization:

1. Set the initial time $t_0 = 0$.
2. Select the initial state X_0 according to an arbitrary initial distribution.

Simulation step:

1. Set up a list of all possible transitions $\omega_i \to \omega_j$ and their corresponding rates $\{q_{ij}\}$, where ω_i denotes the current state of the process.
2. Sample a transition time τ_{ij} for every possible transition $\omega_i \to \omega_j, j \neq i$ and store them in ascending order.
3. Choose the transition $\omega_i \to \omega_k$ for which $\tau_{ik} < \tau_{ij}, \forall j \neq k$ and set $t_{n+1} = t_n + \tau_{ik}$
4. Perform the transition $\omega_i \to \omega_k$ and continue with step 1.

In each simulation step, this algorithm requires to sample one random number for every possible transition $\omega_i \to \omega_j$. In comparison to the BKL algorithm which only requires *two* random numbers in each simulation step, this algorithm seems not to be very efficient at first glance. However, in many cases most of the transitions and corresponding rates stay unaffected during a transition step[7]. In this case, the FR method can be modified in a very effective way by utilizing the memoryless property of the exponential distribution, Eq. (3.14). Then, step 2 of the algorithm requires to sample transition times only for new transitions. These transition times have to be sorted into the preexisting list of transition times which correspond to transitions unaffected by the last transition. For these unchanged transitions no new residence times need to be sampled due to the memoryless property of the exponential distribution. For many systems, this modified version of the FR method turns out to be superior to the BKL algorithm.

[7] In this context, it is useful to think of the simulation of surface diffusion processes, where a diffusion jump of one single particle is unlikely to affect *all* other particles, but rather some particles in its local vicinity.

Part II

Kinetic Monte Carlo Simulations

CHAPTER 4

Details of the Simulations

This chapter is devoted to a detailed description of the simulation model. The investigated system is a many particle system consisting mainly of polymer chains and metal clusters in various sizes. Due to the complexity of the processes which are crucial for the formation of metal polymer nanocomposites, an *ab-initio* approach is not applicable. Alternatively, the system is modeled by using an algorithm based on the kinetic Monte Carlo method [20, 128] whose mathematical foundations were discussed in Chap. 3. The KMC method has seen remarkable progress over the last several decades and has been successfully applied to study the dynamics of coupled processes, leading to structure formation of matter, which are not accessible via *ab-initio* methods or continuum approaches. Two important fields of applications are surface processes such as island growth [23, 129] and self-organization of atomic lattices [130–132], to give two examples.

Since many of the required input parameters are not known exactly, it is not the aim of the simulations to reproduce experiments quantitatively. Instead, the goal was to develop a feasible simulation scheme that covers the main aspects of nanocomposite formation and which is able to reproduce and predict qualitative changes caused by variations of experimental conditions. Therefore, in terms of KMC simulations, at the heart of the simulation model is a catalog of idealized processes such as cluster growth, diffusion processes, and evaporation. The rules under which these processes proceed are described in the first section of this chapter. The second section is devoted to a discussion of the simulation algorithm and important numerical details.

4.1 Description of the Simulation Model

The main goal of the simulations is the analysis of coupled cluster processes such as diffusion, evaporation and cluster growth and their influence on the resulting structure of the nanocomposite. The simulation model extends previous simulations of the diffusion of metal in polymers [22]. In order to develop a simulation algorithm that allows for the description of such a macroscopic system (typical simulations contain up to 10^7 clusters), the complex processes taking place during polymer metalization have to be condensed into a self-consistent simulation scheme containing the main cluster processes and their corresponding rates.

4.1.1 Polymer

The complex microscopic properties of the polymer substrate, its atomic and chemical structure are not directly included in the simulation model. Instead, its influence is reflected in averaged cluster mobilities (expressed in rate constants), atomic evaporation rates and diffusion jump lengths of clusters. In general, the polymer is considered as a continuum.

Two different experimental scenarios are covered by the simulations: the first one is the formation of a metal-polymer interface. In this case, the polymer is located in the half-space $\{(x, y, z) \in \mathbb{R}^3 \,|\, z \leq 0\}$ with its surface located at $z = 0$. The second scenario is co-deposition of metal and polymer [133]. To model this process, the polymer surface is shifted in positive z-direction with a constant velocity v_p corresponding to the incoming flux of polymer. This shift is superimposed by a second shift which is due to the arrival of new metal atoms on the surface. This is necessary to avoid metallic filling factors larger than 1, see also Sec. 6.1. To this end, monomers which are deposited on the surface are assigned an effective volume V_{eff} which is defined as the volume one atom contributes to one monolayer (ML) of atoms (one ML is defined as certain density of atoms covering the surface. For details see Sec. 4.1.6). The polymer surface is then shifted by $\delta z = V_{eff}/A$ (A is the area of the surface) every time a monomer is deposited on the surface and shifted by -δz once a monomer evaporates from the surface.

In experiments, the polymer substrate is often pretreated with ion bombardment [38] or reactive metals [43] in order to produce point-like surface defects with a desired surface density. To incorporate these effect in the simulations [134], distinguished points with a predefined trapping radius $r_t = 0.3\,\text{nm}$ are randomly distributed on the surface.

The effect of defects is to fix clusters as soon as they diffuse into their trapping region. These clusters serve as preferred nucleation sites for cluster growth.

4.1.2 Clusters

Clusters are considered within the framework of the liquid drop model [25]. The liquid drop model assumes clusters to have a constant density regardless of their size and a spherical shape, which is a good assumption supported by TEM measurements [55, 135] and MD simulations of small Ag_n clusters [136]. Then the radius r_n of a cluster C_n containing n atoms is equal to

$$r_n = r_a n^{1/3}, \tag{4.1}$$

where r_a is the atomic radius of the cluster species. According to experimental results, clusters are assumed to be stable in the sense that they do not decompose into smaller clusters [37]. In general, clusters may agglomerate and form larger clusters if the distance of their surfaces falls below a critical distance r_{crit}. The nucleation of clusters starts from a two-body process and obeys the following reaction scheme:

$$C_1^{(t)} + C_1 \rightarrow C_2^{(t)}, \qquad C_n^{(t)} + C_m \rightarrow C_{n+m}^{(t)}, \tag{4.2}$$

where the subscripts denote the number of atoms the cluster contains and the optional superscript t indicates that the cluster is trapped by a defect site. As one can see from the reaction scheme, formation of clusters is mainly due to two processes. The first one is the formation of large clusters by merging of two free smaller clusters. The second process that has to be taken into account is the growth of clusters at defect sites. Within this process, one of the two participating clusters (and the resulting cluster) is trapped by a surface defect. After agglomeration, the radius r_{m+n} of the new cluster is given by:

$$r_{m+n} = \left(r_m^3 + r_n^3\right)^{1/3}, \tag{4.3}$$

which is in accordance with Eq. (4.1). This model of cluster growth goes back to P. Meakin and F. Family, who invented it in order to study the coalescence of clusters on two-dimensional substrates [99, 102]. Obviously, this model can only describe the first stage of cluster growth which is characterized by growth of separated spherical islands. In order to describe the transition from spherical growth to the formation of elongated structures, consisting of partially coalesced clusters, and finally the full percolation stage, a cutoff radius r_c is introduced above which two overlapping clusters do not fully coalesce but stay side by side. This growth model is an extension of the

Family and Meakin model (FMM) and usually referred to as the interrupted coalescence model (ICM) [21]. The ICM involves the following rules for two clusters with radiuses r_m and r_n:

1. If $r_m < r_c$ *or* $r_n < r_c$, the clusters agglomerate according to Eq. (4.3) and the new cluster is located at the center of mass of the two clusters.

2. If $r_m >= r_c$ *and* $r_n >= r_c$, the clusters do not coalesce but stay juxtaposed.

4.1.3 Cluster Processes

After being deposited on the surface, atoms (clusters) may perform several competing processes, see Fig. 4.1 for an illustration. Clusters may perform two different diffusion processes: surface and bulk diffusion. Surface diffusion leads from one point on the surface to another one. Bulk diffusion is diffusion from the surface into the bulk or diffusion within the bulk. According to MD simulations indicating that diffusion in polymers is a hopping process [104–107, 137], clusters perform isotropically distributed diffusion jumps of constant length $l = 0.6\,\text{nm}$, which is approximately the diameter of a polycarbonate chain. Diffusion jumps occur at discrete points in time and a jump frequency depending on the material as well as the cluster size, for details see Sec. 4.1.5.

Radiotracer measurements revealed that, depending on the temperature and the metal/polymer combination, metal atoms do not fully condensate on the polymer surface but partially re-evaporate. According to these measurements, metal atoms perform a random walk on the surface prior to re-emission, rather than being backscattered directly [39]. To capture this effect, monomers are allowed to evaporate from the surface

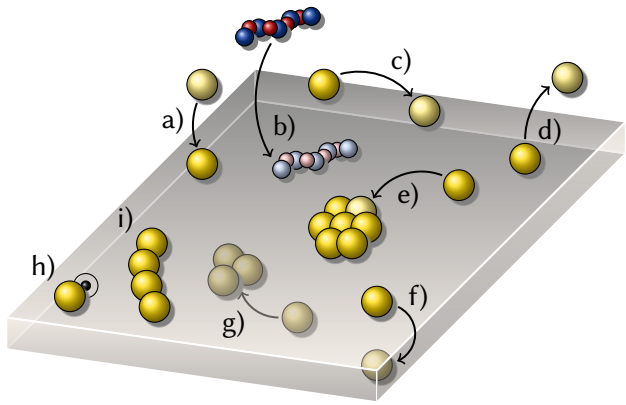

Figure 4.1: *Illustration of the elementary cluster processes considered in the KMC simulations of nanocomposite formation including deposition of atoms and polymer a,b), surface and bulk diffusion c,f,g), reemission of monomers d), cluster agglomeration e,g), trapping at surface defects h), and formation of percolating networks induced by interrupted coalescence of clusters i).*

with a certain rate ν_e that has to be adjusted to the desired values of condensation coefficients $\mathcal{C}$ known from experiments.

4.1.4 Time Evolution

The time evolution of the system is governed by the frequencies $\nu_{\mathrm{n}}^{b/s}$ of diffusion events which are related to the diffusion coefficients $D_{\mathrm{n}}^{b/s}$ by

$$D_{\mathrm{n}}^{b/s} = \beta l^2 \nu_{\mathrm{n}}^{b/s}, \qquad \beta = \begin{cases} 1/6 : \text{bulk diffusion} \\ 1/4 : \text{surface diffusion} \end{cases}, \tag{4.4}$$

with the jump length l and a geometrical factor β. Further, b and s stand for bulk and surface diffusion, respectively. The time scale in the whole simulation is then set by one of these rates. Due to the fact that for many systems exact atomic diffusion constants are not known, the bulk diffusion rate is set to one and a dimensionless time τ scale is defined by scaling time with the inverse of the bulk diffusion rate of monomers:

$$\tau = 1\,\mathrm{jpa} := 1/\nu_1^b = \frac{l^2}{6 D_1^b}. \tag{4.5}$$

By definition, 1 jumps per atom (jpa) is the average time between two bulk diffusion events of a monomer, see also Sec. 3.1.7. Assuming a bulk diffusion coefficient D_1^b of 10^{-15} cm^2/s, which is a typical magnitude for metal/polymer systems [36, 44, 138], and the jump length to be $l = 0.6$ nm, 1 jpa translates into 6×10^{-1} s.

Furthermore, all rates of processes incorporated in the simulations are given in units of the bulk diffusion rate.

4.1.5 Diffusion Rates

The diffusion coefficients obviously depend on the cluster size which is also indicated by the subscript n denoting the number of atoms a cluster consists of. To model the bulk diffusion of clusters in polymer systems below the glass transition temperature T_g, different approaches were developed. A central role has been played by the so-called free volume theory (FVT) introduced by M. Cohen and D. Turnbull [139]. It was developed in the 1950s to describe self-diffusion in liquids of hard spheres. The main idea of the FVT is to explain diffusion in terms of the redistribution of vacancies. The assumptions of

the FVT lead to the following prediction for the diffusion coefficient D of the diffusing species:

$$D \sim e^{-\gamma \frac{V^*}{V_f}}, \tag{4.6}$$

where γ is a geometrical factor, V^* is the minimum volume into which a molecule of the diffusing species can jump, and V_f is the average free volume per spherical molecule in the liquid. Cohen and Turnbull stated that V^* is approximately the specific volume of the diffusing molecule which means that the FVT, in its original formulation, predicts an exponential decay of the diffusion coefficient with the size of the diffusing particle. In the 1970s, the concepts of the FVT were extended to describe binary diffusion processes in systems consisting of a polymer species and a solvent [140–143]. These extensions also predict an exponential dependence of the diffusion coefficient on the particle size.

Based on the outcomes of the FVT, the following scaling of the bulk diffusion rate with the cluster size n is chosen:

$$\nu_{\mathrm{n}}^b = 2^{-n} \cdot \nu_1^b, \qquad \nu_1^b \equiv 1. \tag{4.7}$$

In order to describe surface diffusion adequately, the FVT is not applicable since the concept of vacancies is not appropriate. As a first approximation a simple power law to connect the surface diffusion rate of a cluster with its size is assumed:

$$\nu_{\mathrm{n}}^s = n^{-\alpha} \cdot \nu_1^s, \qquad \nu_1^s = m \cdot \nu_1^b, \tag{4.8}$$

where the coefficient m denotes the ratio between the surface and bulk diffusion rate of monomers. Typically, surface diffusion is many orders of magnitude faster than bulk diffusion, which is also the case for metal diffusion in polymer systems [14], where the ratio of surface and bulk diffusion coefficients might be substantially smaller than for typical solids due to the large surface roughness of polymers [35]. However, a value around $m = 40$ appeared to be a reasonable choice in order to reproduce the typical bimodal shape of cluster size distributions observed in experiments [35]. For the simulation data presented in this work, a value $\alpha = 1$ was used. MD simulations of cluster diffusion on crystalline surfaces have also predicted a diffusivity following a power law of this form, where α is close to 1 [23].

The glass transition temperature T_g is related to the long range mobility of polymer chains [14, 35]. MD simulations [144] and experiments [145, 146] have shown that diffusion of solvents in polymers falls into two regimes, depending on the ratio σ of the particle size and the gyration radius of the polymer chains. For large particles, ($\sigma > 1$),

theoretical investigations [147] and MD simulations [144] predict the polymer melt to behave like a continuum on the length scale of the particles and the diffusion coefficient D_{n}^{b} to be in good agreement with the *Stokes-Einstein* relation:

$$D_{\mathrm{n}}^{b} = \frac{k_B T}{6\pi\eta r_n} \quad \Longrightarrow \quad D_{\mathrm{n}}^{b} \sim n^{-1/3}. \tag{4.9}$$

If the particles are smaller than the polymer chains, $(\sigma < 1)$, the prediction of the Stokes-Einstein relation usually fails and underestimates the diffusivity since the clusters start to see the microscopic viscosity [144] which is expected to be reduced in comparison to the global viscosity due to depletion of polymer around those particle's surfaces [148, 149]. In this regime, MD simulations suggest the diffusion coefficient to be inversely proportional to the cube of the radius [144], contradicting the predictions of the Stokes-Einstein relation,

$$D_{\mathrm{n}}^{b} \sim R_n^{-3} \quad \Longrightarrow \quad D_{\mathrm{n}}^{b} \sim n^{-1}\,, \tag{4.10}$$

with R_n being the particles hydrodynamical radius which is defined as the radius of a hard sphere that diffuses at the same rate as the particle. In many cases R_n is orders of magnitude larger than the actual particle radius [150]. However, since clusters are considered as hard spheres in the simulations, R_n is identical to the cluster radius.

4.1.6 Deposition

As in real experiments, metal atoms are deposited on the surface during a finite deposition time t_d with a certain flux R_m of atoms which is assumed to be stationary. The deposition rate is given units of ML/jpa, where one monolayer corresponds to a surface density of 10 atoms per nm^2 [37]. Assuming that one ML has the thickness of the atomic diameter d_a, 1 ML/jpa can be translated into SI units using the definition of jpa, Def. (4.5),

$$1\,\mathrm{ML/jpa} = \frac{6 d_a D_1^b}{l^2}. \tag{4.11}$$

Assuming the same bulk diffusion coefficient D_1^b and jump length l as above, 1 ML/jpa translates into 3×10^1 nm/min.

4.2 The Simulation Algorithm

As already mentioned in Chap. 3, the algorithm used in the simulations is based on the first reaction method introduced by Gillespie in the 1970s [121]. The main idea of this

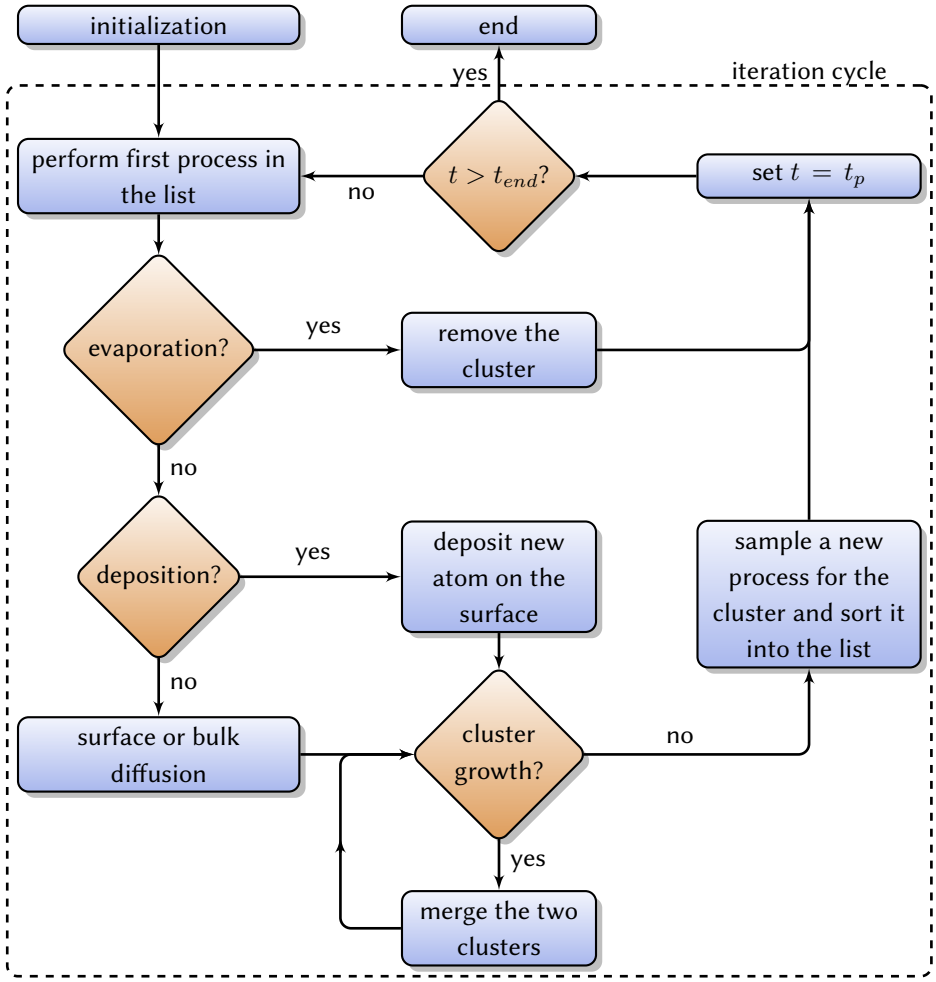

Figure 4.2: *A Flowchart of the simulations illustrating the numerical procedure within one iteration cycle.*

algorithm is to sample time points for every possible elementary process i of the system with its associated rate ν_i. In contrast to the notation in Sec. 3.3, here the transition rates are labeled by just one number and not by two as in Sec. 3.3. This is possible since the transitions the system undergoes do not depend on the current state of system: the diffusion rate of a cluster of a certain size stays unchanged during the evolution of the system. These time points are stored in ascending order and in every simulation step,

the process associated with the smallest process time t_{min} is carried out and the system clock is advanced to the time point t_{min}. Next, the time points of processes belonging to those clusters that were involved in that transition (by cluster agglomeration) are removed from the list, whereas for the remaining clusters, whose state changed due to the last process, a new process time t_i is sampled from an exponential distribution and sorted into the list. At this point, the FR method reveals its advantage over the BKL algorithm; due to the memoryless property of the exponential distribution, the process times of those clusters that were not affected by the last process do not have to be re-sampled. In contrast to that, within the BKL algorithm, the computation of the diagonal element q_i of the Q-matrix and the subsequent sampling of the next process is usually computationally very expensive and has to be performed every simulation step. In case of the present simulations, the most time-consuming part is the organization of the time-ordered list of processes.

Fig. 4.2 shows an algorithm flowchart illustrating the numerical procedure for the case of metal-polymer interface formation with unrestricted cluster growth. As one can see from Fig. 4.2, the iteration cycle (which is framed by the dotted line) always begins with the execution of the process associated with the smallest process time. In case of atomic evaporation, the dataset of the corresponding cluster is simply destroyed and the clock is advanced to the point in time at which the evaporation takes place. If the process is a diffusion process or deposition of a new cluster, the diffusion process is executed or a new cluster is deposited on the surface of the polymer matrix, respectively. Next, it is checked if the distance of the active cluster to any other cluster lies below the critical distance r_{crit}. If yes, the two clusters merge according to Eqs. (4.2) and (4.3) and the data set of one of the clusters is destroyed[1]. This step has to be performed in a loop since the distance to any other cluster may fall below the critical distance due to agglomeration. This loop is left if the distance to all other clusters lies above the critical distance. Afterwards, a new process and an associated process time are sampled and sorted into the time-ordered list of processes. The algorithm terminates once the time exceeds the total simulation time t_{end} which is given as an input parameter to the simulations.

[1] In effect that means the dataset of the non-processing cluster is destroyed and its process time and the corresponding process are removed from the time-ordered list of processes.

CHAPTER 5

Formation of Metal-Polymer Interfaces

In this chapter, numerical results of kinetic Monte Carlo simulations [133, 134] of metal-polymer interface formation [38, 43, 135, 151] are presented. Metal atoms are deposited on a polymer surface and exhibit surface diffusion as well as diffusion into the bulk. At the same time metal atoms form clusters due to their high cohesive energy, re-evaporate from the surface, or get trapped by surface defects. The focus of the present chapter is to discuss the complex interplay of these processes and how the microstructure of the resulting composite is affected due to variation of the deposition conditions.

For all results discussed below, the size of the surface lies between 2500 nm × 2500 nm and 4500 nm × 4500 nm. If not explicitly mentioned, the deposited thickness δ amounts 2 ML, corresponding to a number of 6.25×10^7 to 2.025×10^8 atoms for the given size range of the surface. The monomer deposition rate R_m is spatially homogeneous and varied between 1.0×10^{-5} ML/jpa and 1.0×10^3 ML/jpa. As in experiments, metal atoms are deposited on the surface over a final deposition time $t_d = \delta / R_m$ and immediately start to diffuse and agglomerate after deposition. For the majority of the presented results, the size dependence of the bulk diffusion rate ν_{n}^b is chosen according to Eq. (4.7), which is an appropriate assumption for the diffusion of metal particles in polymers below the glass transition temperature T_g. Simulations with temperatures above the glass transition temperature are discussed in Sec. 5.1.3. Here, the scaling of the bulk diffusion rate ν_{n}^b obeys Eqs. (4.9) and (4.10).

All results presented below correspond to a time instant of 10^4 jpa after the termina-

tion of the deposition. The time dependence of the results was carefully studied and it has been found that longer simulation times do not change the results significantly.

This chapter is divided into four sections: in the first section, the interplay of cluster growth and diffusion is studied for a surface without defects and complete condensation of atoms. In the following two sections, the effects of surface defects and monomer evaporation are investigated. Finally, the chapter concludes with the discussion of simulations involving the interrupted coalescence model introduced in Sec. 4.1.2.

5.1 Complete Condensation without Surface Defects

The interplay of cluster agglomeration and diffusion depending on the deposition conditions is investigated for a polymer surface free of defects. Atomic evaporation is neglected.

5.1.1 Concentration Profiles

The first quantity which will be discussed is the depth-resolved concentration of metal inside the polymer bulk. In order to compute the metal concentration, the polymer was divided in thin layers of thickness 0.015 nm parallel aligned to the surface. The concentration in a given layer at depth z is then defined as the layer volume occupied by clusters divided by the total volume of that layer.

Concentration profiles for two different deposition rates differing by a factor of 20 are depicted in Fig. 5.1. The blue line shows the total concentration and the other lines the fraction of the concentration attributed to clusters in a certain size range as it is indicated in the figure. The total concentration in Fig. 5.1 can, in general, be divided into three parts whose shape is strongly influenced by the deposition rate R_m. The first region is a narrow area just below the surface with a width of about 1 to 2 nm. Here, the cluster concentration is very high with a maximum located about one diffusion length underneath the surface. The second region is characterized by an abrupt decay of the concentration by one to three orders of magnitude and extends over about 1 to 2 nm. The last region which begins in a depth of about 2 to 4 nm, is very broad, and shows a much slower decay of the metal concentration in the bulk. Here the density decay is close to a Gaussian profile which would be the profile in the case of free diffusion of non-interacting particles according to the thin-film solution of Fick's second law.

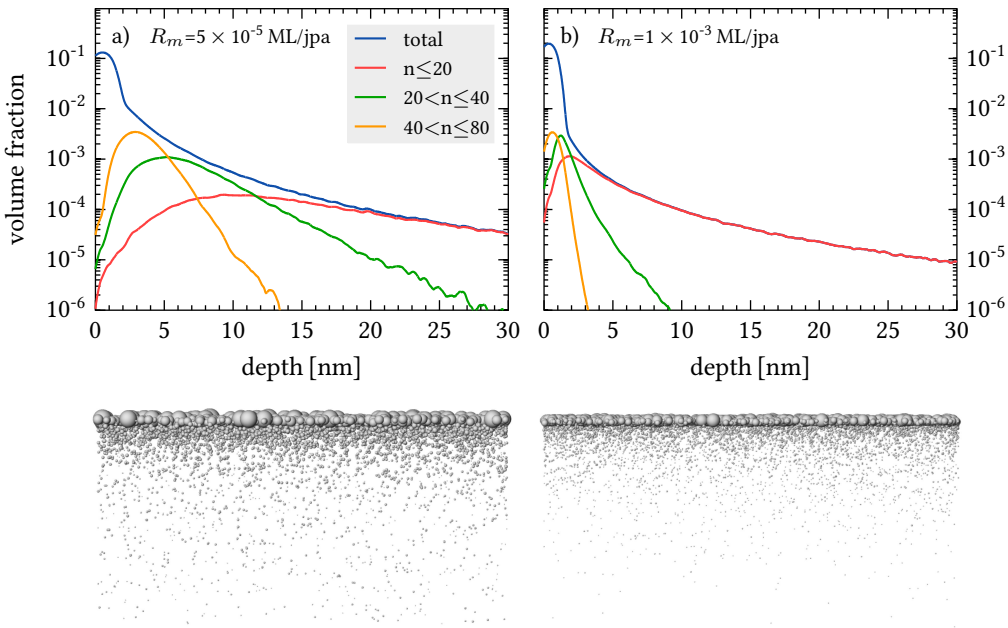

Figure 5.1: *Upper panel: Depth-resolved Concentration profiles for two different values of the atomic deposition rate R_m as indicated in the figure. Lower panel: Illustration of the corresponding cluster density in a 120 nm × 60 nm cutout of the system. The line of vision is directed onto the x-z plane.*

Consequently, all deviations from this behavior result from agglomeration and cluster growth which is most distinctive in the vicinity of the surface.

Fig. 5.2 shows how the deposition rate affects the total concentration profiles. With an increase of the rate, also the concentration in the first region near the surface grows monotonically. From the second region on, the picture turns into its opposite: an increase of the deposition rate leads to a monotonic reduction of the metal fraction in the bulk. The explanation is that an increased deposition rate leads to a more homogeneous growth of smaller, more or less immobile, clusters on the surface (see Sec. 5.1.2), which results in a higher coverage of the surface. Consequently, the probability for small mobile clusters to encounter larger immobile clusters on the surface before diffusing into the bulk is enhanced. In addition to that, there is a higher probability for incoming atoms to impinge directly on clusters on the surface. This explanation is readily verified by considering how many clusters of different sizes are found in a given depth. In Fig. 5.1

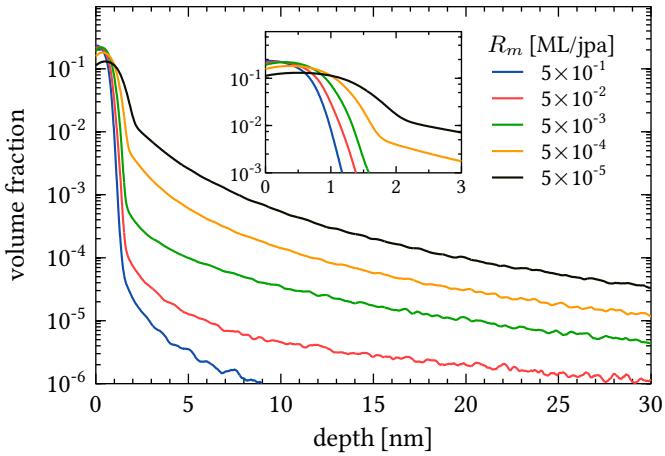

Figure 5.2: *Concentration profiles for five different deposition rates R_m spanning five orders of magnitude.*

the contributions of clusters with less than 20 atoms, with 20 to 40 atoms, 40 to 80 atoms and of larger clusters, to the total density are depicted separately. One clearly sees that, near the surface, the concentration is dominated by the largest clusters with a size of more than 80 atoms. This has been observed for all simulated deposition rates. For the smaller cluster groups one observes a maximum concentration in a depth of few nanometers, cf. Fig. 5.1: first, clusters with a size between 40 and 80 atoms reach a maximum concentration in a depth of about 3 nm, followed by clusters with 20 to 40 atoms the concentration of which peaks in about 5 nm depth. Finally, clusters smaller than 20 atoms have their highest concentration in a depth of about 10 nm. Deeper in the bulk practically only the smallest clusters are found.

In order to gain quantitative insight on how the deposition rate R_m influences the distribution of metal inside the polymer, the mass fraction Q_z of metal, which has penetrated the polymer matrix deeper than a certain depth z [24] is computed. The results for two different values of δ (0.1 ML and 2.0 ML) are collected in Fig. 5.3. Q_z is connected with the concentration profile $c(z)$ via

$$Q_z = \frac{\int_z^\infty c(z')\,dz'}{\int_0^\infty c(z')\,dz'}\,. \tag{5.1}$$

Corresponding to the results shown in Fig. 5.2, the mass fraction of metal in the polymer matrix decreases with an increase of the deposition rate. Interestingly, the mass fraction of metal inside the polymer matrix starts to saturate at very high deposition rates implying that even very fast deposition can not prevent diffusion of metal into the polymer matrix at all. This effect is especially pronounced for thin film thicknesses (see

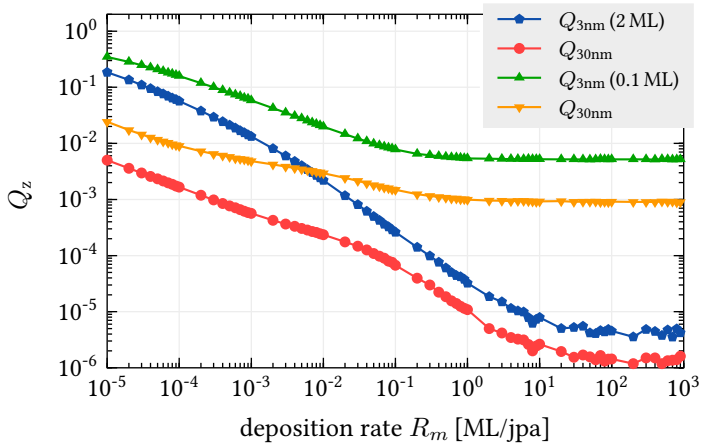

Figure 5.3: *Mass fraction Q_z of metal that has penetrated the polymer matrix deeper than different depths z as a function of the deposition rate R_m. See Eq. (5.1) for the exact definition of Q_z.*

the green and orange curves in Fig. 5.2). Here, the saturation starts at a value of the deposition rate at about 1 ML/jpa and the fraction of clusters that are located 30 nm or deeper in the bulk remains at a value of 1.0×10^{-3}, whereas for 2.0 ML saturation begins around 10 ML/jpa with a value of Q_z which is three orders of magnitude lower than for 0.1 ML. This is very impressive since this implies that for $\delta = 0.1$ ML the total amount of metal located deeper than both 3 (blue and green curves) and 30 nm (red and orange curves) is larger than for $\delta = 2.0$ ML (Note that the total amount of deposited metal only differs by a factor of 20).

Fig. 5.4 a) shows the total amount (measured in ML) of metal $q_z = Q_z\delta$ that is located deeper than $z = 30$ nm in the bulk for three different deposition rates R_m. In Fig. 5.4 b), the corresponding mass fractions Q_{30nm} are depicted. One can clearly see that q_{30nm} has a maximum for the two lower values of R_m which is located around $\delta = 1.0 \times 10^{-2}$ ML. For $R_m = 1.0 \times 10^{2}$ ML/jpa the deposition time t_d lies between 1.0×10^{-6} jpa and 1.0×10^{-2} jpa, i.e. practically no diffusion takes place during deposition. In this case, there are two contrary working mechanisms that are responsible for the non-monotonic behavior of q_{30nm}. The first one, which leads to an increase of q_{30nm}, is an increase of the deposited thickness δ: if more atoms are deposited on the surface, more atoms and clusters may diffuse into the bulk. The second mechanism leading to a decrease of q_{30nm} is aggregation-induced immobility of clusters which comes into play the more atoms are deposited on the surface. For R_m=1.0×10^{-2} ML/jpa and values below (cf. the red curve in Fig. 5.4 a)), the situation is different: up to δ=1.0×10^{-2} ML, the behavior of q is nearly exactly the same as for R_m=1.0×10^{2} ML/jpa. For higher values

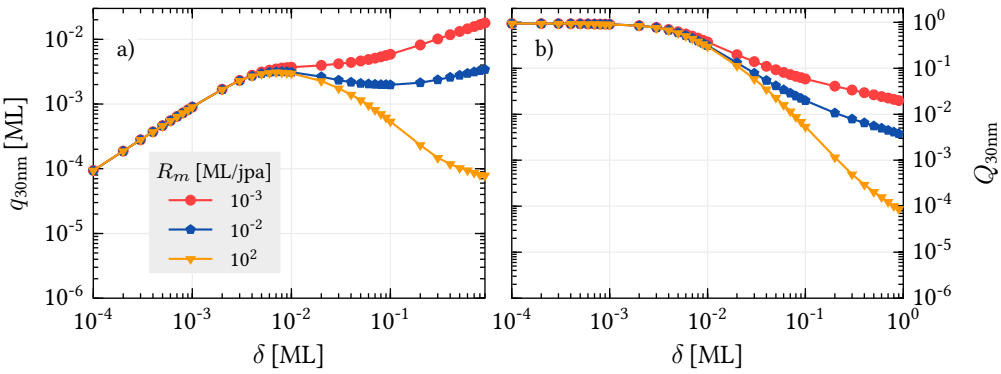

Figure 5.4: *Left panel: total amount q of metal that has penetrated the polymer matrix deeper than 30 nm as a function of the deposited thickness δ for three different deposition rates. Right: mass fraction Q of metal that has penetrated the polymer matrix deeper than 30 nm as a function of the deposited thickness δ. The deposition rates are the same as in the left panel.*

of δ, diffusion processes during deposition start to play a role because t_d exceeds the time amount of 1 jpa, which is by definition the average time between two bulk diffusion jumps of a single atom, see Eq. (4.5) and Sec. 3.1.7. As a consequence, atoms and small clusters may diffuse into the polymer matrix during deposition leading to an enhanced metal concentration in the bulk.

5.1.2 Cluster Size Distributions

In addition to the concentration profiles discussed above, the simulations also yield the complete information about the size spectrum of the grown clusters. To this end, size distributions were calculated from the resulting cluster configuration as the fraction of clusters with a particular size n (measured in number of atoms) related to the total number of clusters. Despite the fact that the size distributions are defined only on integers, they are depicted as continuous functions resulting from spline approximations of the given data sets. Since the simulations usually contain several million clusters, the size distributions are a priori very smooth such that the depicted splines do not distort the simulated size distributions. In Fig. 5.5 size distributions for three different deposition rates ranging from 2.0×10^{-5} ML/jpa to 1.0×10^{-3} ML/jpa are depicted. Fig. 5.5 a) shows the global distribution of cluster sizes which is typically characterized by three maxima

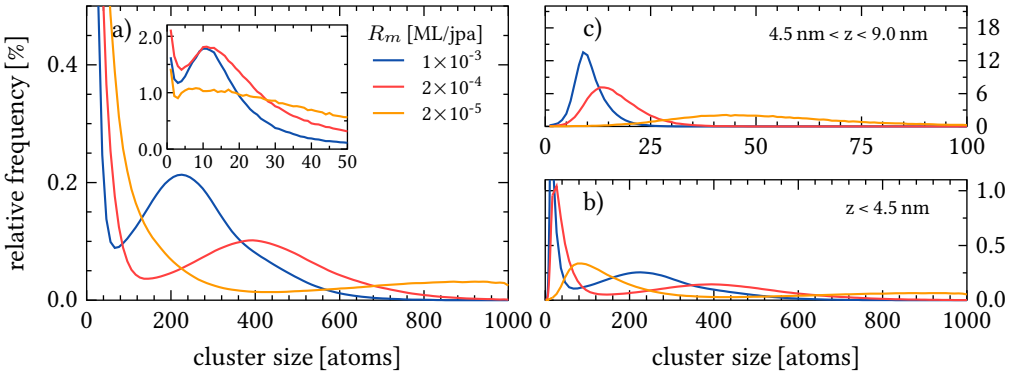

Figure 5.5: *Cluster size distributions for three different deposition rates R_m spanning three orders of magnitude as indicated in the figure. No surface defects. Left panel: global cluster size distribution. Right panel: depth-resolved size distributions in two different thin layers of thickness 4.5 nm below the surface. Note the different vertical scales.*

whose shape and position vary with the deposition rate. A bimodal shape of the cluster size distribution with one maximum at small sizes and one maximum at larger sizes is very well known from experiments [35, 152, 153]. The finite resolution of experimental measurements of cluster sizes might be the reason for the indistinguishability of the first two peaks which are very close to each other.

At all deposition rates, the first peak is contributed by monomers and the second peak by clusters of a size around $n = 10$, whereby the second peak is very broadened for the lowest deposition rate. Both peaks exhibit about the same intensity and dominate the third peak by a factor of around 10. Thus, there is a large fraction of dimers and trimers and a rapid decay of the size distribution towards larger clusters. An increase of the deposition rate leads to a sharpening of the first peak, see inset of Fig. 5.5 a). This maximum is mainly attributed to monomers deep in the bulk which is verified by Fig. 5.5 b) and c) which show the size distribution in two layers of thickness 4.5 nm under the surface. Here, one can see that monomers practically do not make a contribution to the size distributions up to a depth of 9 nm, and thus are located deeper in the bulk.

The size distributions at the surface layer (Fig. 5.5 b)) exhibit a bimodal shape with two maxima. The position of the second maximum corresponds to the position of the third maximum in the global size distributions. Since this second maximum already vanishes in the second layer under the surface, the third maximum of the global distribution

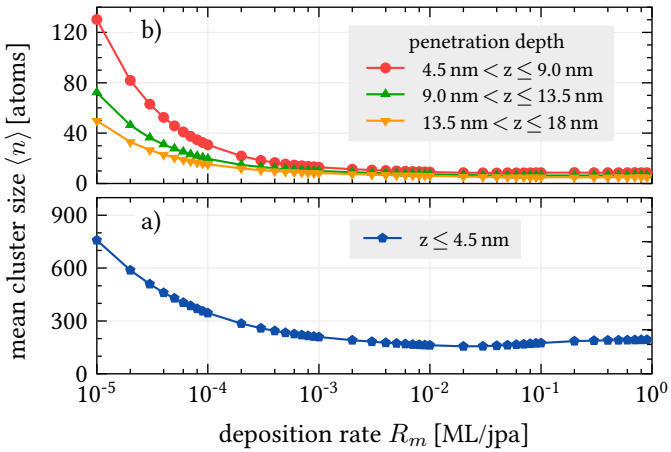

Figure 5.6: *Depth resolved mean cluster size $\langle n \rangle$ in thin layers of thickness 4.5 nm as a function of the deposition rate R_m for a surface without defects. The bottom figure shows the top layer just below the surface, the upper figure shows three layers deeper in the bulk.*

relates to clusters located in the direct vicinity of the surface. Its position and shape exhibit a strong dependence on the atomic deposition rate; an increase of the deposition rate causes a shift of the peak to smaller cluster sizes and a simultaneous narrowing. This reflects the tendency towards homogeneous nucleation at the surface and a narrowing of the growth region of larger clusters in case of high deposition rates (see also the lower panel of Fig. 5.1).

Deeper in the bulk, the size distributions only consist of one maximum whose position shifts to smaller sizes in larger depths. The position of this peak coincides more or less with the mean cluster size $\langle n \rangle$ in the corresponding layer. This is clearly confirmed by Fig. 5.6 which depicts the mean cluster size in four layers of thickness 4.5 nm under the surface as a function of the deposition rate. The general trend one observes is a clear reduction of the mean cluster size with growing distance from the surface. The decay is particularly strong immediately below the surface: from the first to the second layer the mean cluster size drops approximately by a factor of six.

As already mentioned before, the values of the mean cluster size are close to the peak positions in Fig. 5.5 b) and c). Again, there is a clear trend of a monotonic decrease of the mean cluster size with the deposition rate in any depth. At a value around 1.0×10^{-3} ML/jpa, the mean cluster size starts to saturate in all layers. The decrease of the mean cluster size may seem surprising, but it is consistent with the observations made in Secs. 5.1.1 and 5.1.2. As one can see from Fig. 5.2, high deposition rates lead to enhanced metal concentrations in the vicinity of the surface and narrow cluster size distributions, cf. Fig. 5.5. The enhanced concentration of clusters near the surface inhibits

the penetration of metal into the bulk such that an increase of the deposition rate is accompanied by an overall decrease of the mean cluster size.

5.1.3 Behavior above the Glass Transition Temperature

In this section, the behavior of systems with temperatures above the glass transition temperature T_g is discussed. In the simulations, the effect of the temperature is not directly considered. Instead, the transition from temperatures below T_g to temperatures above T_g is modeled by changing the scaling of the bulk diffusion rate ν_{n}^b with the cluster size n. Instead of applying an exponential decay with n, cf. Eq. (4.7), the scaling is chosen according to Eqs. (4.9) and (4.10). Eq. (4.9) is assumed for clusters with a diameter larger than the average gyration radius of the polymer chains and describes the diffusion of spherical particles in a liquid, see Sec. 4.1.5,

$$\nu_{\mathrm{n}}^b \sim D_{\mathrm{n}}^b \sim n^{-1/3}. \tag{5.2}$$

The diffusion of smaller clusters is described by Eq. (4.10) which predicts the diffusion rate to be inversely proportional to the cluster size n,

$$\nu_{\mathrm{n}}^b \sim D_{\mathrm{n}}^b \sim n^{-1}. \tag{5.3}$$

The results in this section are computed with the same parameter set as the previously discussed results, except for the scaling of the bulk diffusion rate ν_{n}^b.

In Fig. 5.7 concentration profiles for five different deposition rates R_m are shown. Expectably, the profiles significantly differ from those illustrated in Fig. 5.1.1. The main

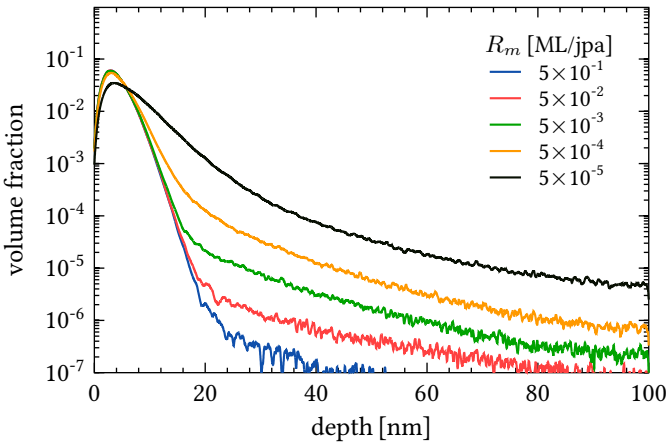

Figure 5.7: *Concentration profiles for five different deposition rates R_m spanning five orders of magnitude.*

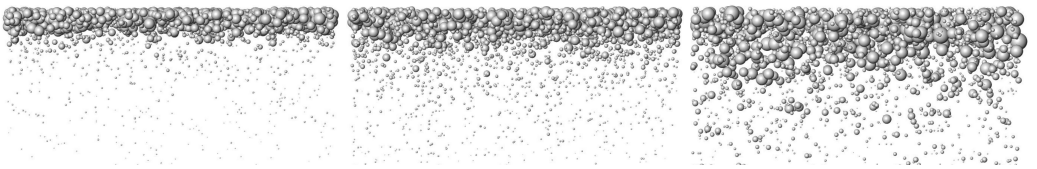

Figure 5.8: *Illustration of the cluster density for R_m=10^{-3} ML/jpa (left), R_m=10^{-4} ML/jpa (middle) and R_m=10^{-5} ML/jpa (right) in a 120 nm × 60 nm cutout of the system. The line of vision is directed onto the x-z plane.*

difference is an enhanced concentration in the bulk of the polymer matrix which is a direct consequence of the increased mobility of clusters in the bulk. In a small area up to about 2 nm below the surface, the situation is reversed: here, the accelerated diffusion of clusters into the bulk leads to a distinct decrease of the concentration. In contrast to temperatures below the glass transition temperature, the concentration shows a steep increase by almost two orders of magnitude near the surface and has its maximum in a depth of about 4 nm for all depicted deposition rates. Except for the lowest deposition rate, $R_m = 10^{-5}$ ML/jpa, all profiles follow the same run up to a depth of about 10 nm and start to diverge afterwards.

Fig. 5.9 a) shows size distributions for three different deposition rates. They do not

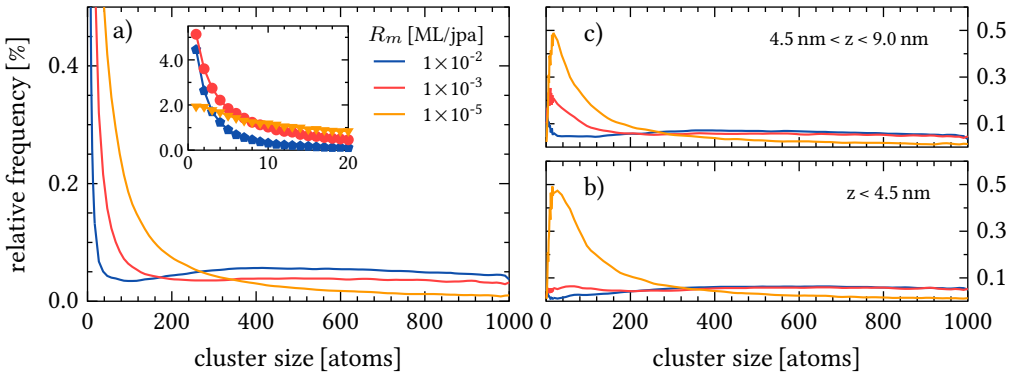

Figure 5.9: *Cluster size distributions for three different deposition rates R_m as indicated in the figure. No surface defects. Left panel global cluster size distribution. Right panel: depth-resolved size distributions in two different thin layers of thickness 4.5 nm near the surface.*

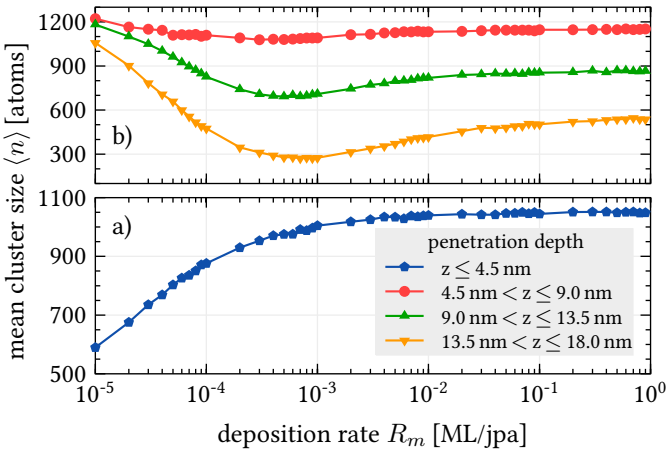

Figure 5.10: *Depth resolved mean cluster size $\langle n \rangle$ in thin layers of thickness 4.5 nm as a function of the deposition rate R_m for a surface without defects and $T > T_g$. The bottom figure shows the top layer, just below the surface, the upper figure shows three layers deeper in the bulk.*

have the shape that was found at temperatures below the glass transition. Instead, they are characterized by one maximum contributed by monomers and a rapid decrease towards larger sizes which are homogeneously distributed over a broad range. This broadening of the distribution results from an extension of the growth region of clusters, i.e. large clusters are likely to grow in larger depths due to their enhanced mobility, see the right panel of Fig. 5.8.

Interestingly, an increase of the deposition rate has a totally different effect than for $T < T_g$; whereas for $T < T_g$ the mean cluster size significantly decreases in all regions of the polymer matrix, cf. Fig. 5.6, an increase of the deposition rate results in a steady increase of the mean size in the vicinity of the surface, cf. Fig. 5.10 a). In the regions below, the behavior is different: the mean size first decreases, reaches a minimum and starts to increase again. This behavior is more pronounced at larger depths; for z between 4.5 and 9.0 nm, a variation of the deposition rate has almost no effect on the mean cluster size, cf. the red curve in Fig. 5.10 b). Besides, this is the region with the largest mean cluster size for all investigated values of the deposition rates. For $R_m = 10^{-5}$ ML/jpa, the mean cluster size in the layer directly under surface is even smaller than in the three layers below. The reason for this phenomenon is the accelerated diffusion of clusters into the bulk. Whereas at temperatures below T_g, clusters containing only some few atoms are practically fixed at the surface, also larger clusters my diffuse into the bulk if the glass transition temperature is exceeded. As a result, clusters being embedded some nm below the surface are exposed to a large influx of clusters and atoms diffusing from the surface into the bulk. This influx is larger than the influx clusters on the surface are exposed to

due to impingement of new atoms and thus results in an enhanced formation of large clusters below the surface.

5.2 Influence of Surface Defects

In experiments, the polymer surface is often exposed to ion bombardment [38] or pre-treated with reactive metals [43] in order to gain a certain density ρ_t of surface defects. The main effects of these defects are trapping of clusters and a significant reduction of metal diffusion into the polymer bulk. In [43], Thran et al. report about experimental investigations of silver diffusion into TMC-PC where only 0.08 ML (which corresponds to a density of 8.0×10^{-1} nm^{-2}) of Cr pre-deposited on the surface act as an almost perfect barrier against diffusion of silver into the polymer matrix.

5.2.1 Concentration Profiles

Concentration profiles[1] for five different densities of surface defects are illustrated in Fig. 5.11. One clearly recognizes that the influence of defects is different in the bulk and in the vicinity of the surface: while defects raise the concentration in the direct vicinity of the surface up to a depth of 0.5 nm, see the inset of Fig. 5.11, the concentration in the bulk is lowered (see also Fig. 5.14). This Lowering is especially pronounced in a depth between 0.5 and 3 nm where the concentration rapidly decreases.

[1] From this chapter on, the scaling of the bulk diffusion rate is chosen according to temperatures below the glass transition temperature T_g, cf. Eq. (4.7).

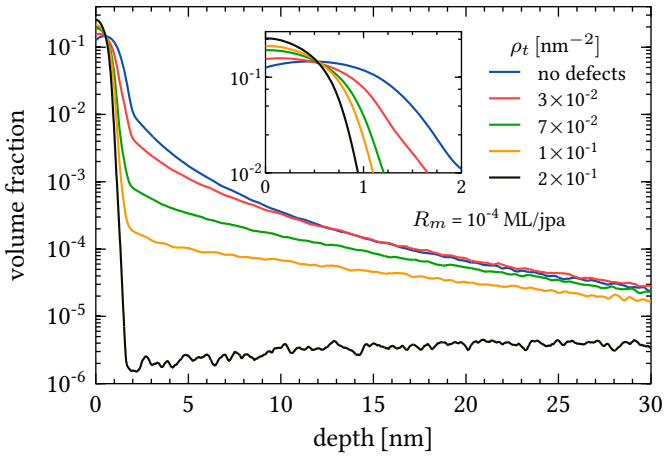

Figure 5.11: *Concentration profiles for five different densities ρ_t of surface defects ranging from 0 to 2×10^{-1} nm^{-2} and a fixed deposition rate $R_m = 10^{-4}$ ML/jpa.*

Deeper in the bulk, this effect weakens and the concentration profiles approach each other. Obviously, the reason for this effect of surface defects is the enhanced growth of trapped clusters at the surface which act as nucleation centers and cause a more homogeneous nucleation of clusters, see Fig. 5.15. This homogenization is accompanied by an enhanced surface coverage[2] σ, see Fig. 5.12, leading to a reduced diffusion of metal into the bulk. For defect densities $\rho_t > 2 \times 10^{-1}\,\mathrm{nm}^{-2}$, the behavior of the concentration profile changes drastically; while at densities below $2 \times 10^{-1}\,\mathrm{nm}^{-2}$, the concentration decreases monotonically, it starts to increase after a very pronounced drop off near the surface but stays below a value of 1.0×10^{-5}. This can also be seen in Fig. 5.14 which mimics the appearance of a TEM micrograph as a view on the x-z plane of the nanocomposite. The right-hand figure in Fig. 5.14 corresponds to the black curve in Fig. 5.11. It clearly shows a region of depletion of metal clusters directly underneath the surface.

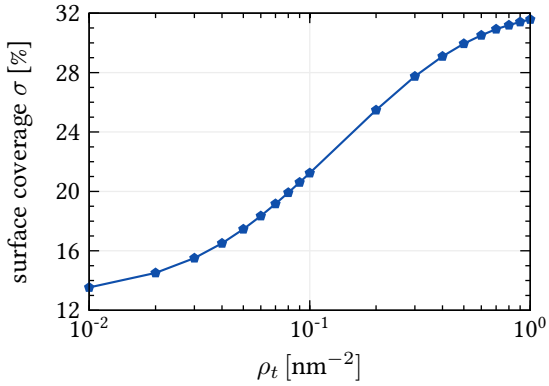

Figure 5.12: *Surface coverage as a function of the density ρ_t of surface defects at constant deposition rate R_m=1.0 × 10^{-4} ML/jpa.*

Fig. 5.13 illustrates the dependence of the mass fraction Q_z on the density ρ_t of surface defects for $z = 3\,(30)\,\mathrm{nm}$ and a constant monomer deposition rate $R_m = 1.0 \times 10^{-4}$ ML/jpa. In accordance to the concentration profiles shown in Fig. 5.11, the fraction of metal that diffuses into the bulk is significantly lowered for high values of ρ_t. For low densities ($\rho_t \lesssim 4.0 \times 10^{-2}\,\mathrm{nm}^{-2}$), Q_3 and Q_{30} differ by factor of about 10. An increase of ρ_t causes a reduction of $Q_{3(30)}$ and a simultaneous approach of the curves until they almost coincide at a value of

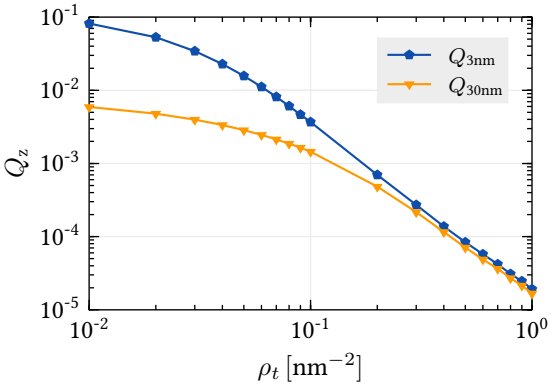

Figure 5.13: *Mass fraction Q_z for $z = 3(30)\,nm$ as a function of the density ρ_t of surface defects. The deposition rate is $R_m = 1.0 \times 10^{-4}$ ML/jpa.*

[2] defined as the fraction of the surface being covered by clusters.

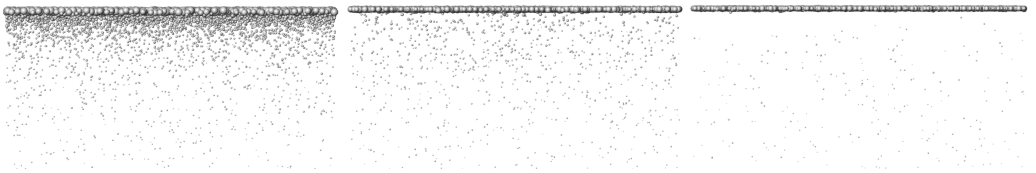

Figure 5.14: *Illustration of the cluster density for three different densities of surface defects in a 120 nm × 60 nm cutout of the system. Left: $\rho_t = 1 \times 10^{-2}$ nm^{-2}. Middle: $\rho_t = 1 \times 10^{-1}$ nm^{-2} Right: $\rho_t = 2 \times 10^{-1}$ nm^{-2}. The line of vision is directed onto the x-z plane.*

$\rho_t = 2.0 \times 10^{-1}$ nm^{-2}. Further increase of ρ_t results in a decrease of $Q_{3(30)}$ following approximately a power law of the form $Q_z = a\rho_t^{-b}$ which can be seen from the linear tail of the two curves in the log-log graph.

5.2.2 Size Distributions

The left panel of Fig. 5.15 shows the global cluster size distribution for different densities of defects and opposes them to a distribution for a surface without defects (blue line).

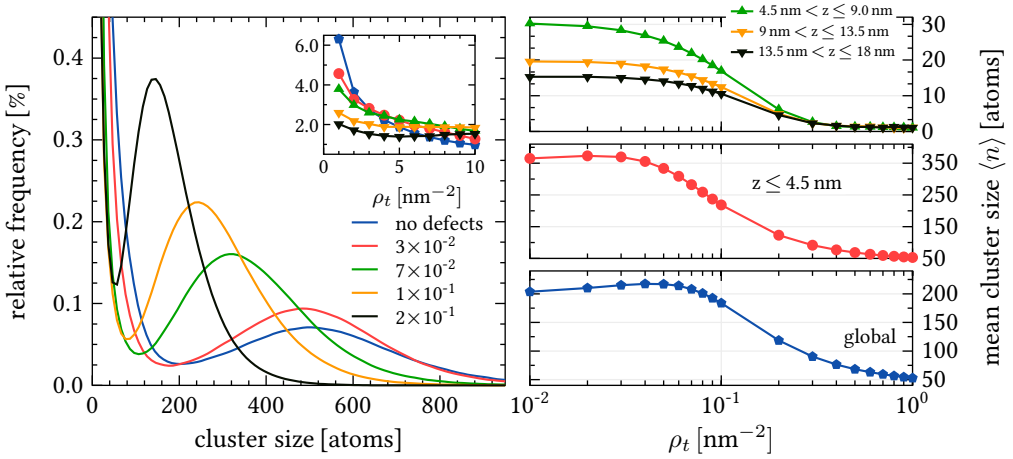

Figure 5.15: *Left: cluster size distributions for five different densities ρ_t of surface defects as indicated in the figure. Right: mean cluster size $\langle n \rangle$ as a function of the density of surface defects. the bottom figure shows the global average. The upper figures show the averaged cluster size in thin layers of thickness 4.5 nm as indicated in the figure.*

It illustrates the above-mentioned homogenization of cluster growth on the surface due to the presence of surface defects: an increase of ρ_t causes a shift of the secondary maximum (which is attributed to clusters on the surface and in the direct vicinity of the surface) to smaller sizes. At the same time, the maximum is considerably slandered.

The upper panel of the right-hand side of Fig. 5.15 shows that the mean cluster size is not significantly affected up to a value of $\rho_t \approx 6 \times 10^{-2}$ nm^{-2}; at smaller densities, defects cause an increase of the mean cluster size which becomes more evident by comparing the blue and the red curves in the left panel of Fig. 5.15. At values above 6×10^{-2} nm^{-2} the mean cluster size starts to decrease which is associated with a clear reduction of metal diffusion into the bulk, see Figs. 5.11 and 5.14.

5.3 Incomplete Condensation

As already mentioned in Sec. 2.2.4, the condensation coefficient $\mathcal{C}$ of metals on polymers strongly depends on the metal/polymer combination as well as on the temperature of the substrate. In the simulations, the incomplete condensation of metal on polymer is achieved by allowing monomers to re-evaporate from the surface with a certain rate ν_e as described in Sec. 4.1.3.

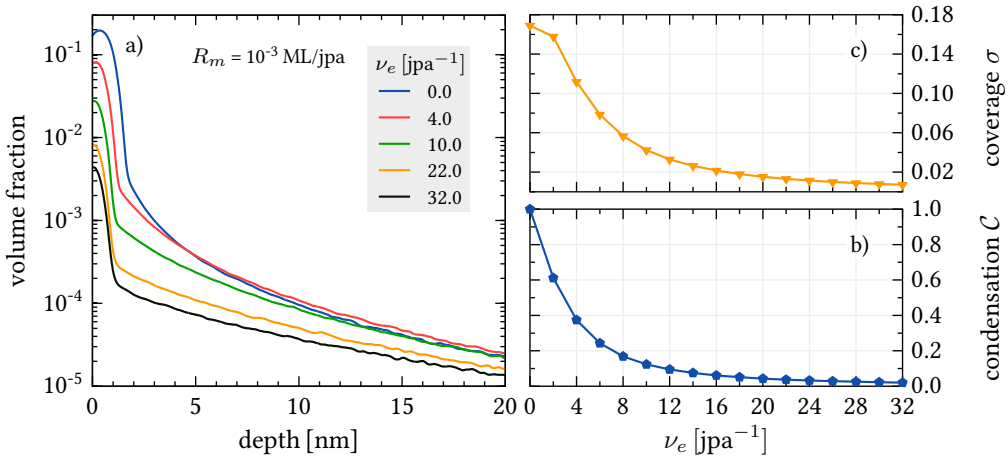

Figure 5.16: *Left: concentration profiles for five different values of the monomer evaporation rate ν_e as indicated in the figure. Right: condensation coefficient $\mathcal{C}$ (bottom) and surface coverage σ (top) as a function of the monomer evaporation rate ν_e.*

5.3.1 Concentration Profiles

In Fig. 5.16 a) the influence of monomer evaporation on the concentration profile is shown for five different evaporation rates ν_e lying in the parameter range $\nu_e = 0.0 \ldots 32.0\,\mathrm{jpa}^{-1}$. Obviously, the main effect of monomer evaporation is an overall reduction of the metal concentration which is caused by desorption of monomers from the surface and the resulting decrease of the total amount of metal in the polymer. Most affected is the region in the vicinity of the surface. Here, the reduction amounts up to a factor of about 60, which roughly corresponds the reduction of the condensation coefficient, as shown in Fig. 5.16 b). Deeper in the bulk, the reduction is clearly reduced. For very low evaporation rates $\nu_e < 10\,\mathrm{jpa}^{-1}$, this effect is not noticeable or even reversed, see the red curve in Fig. 5.16 a) which exceeds the blue curve at a depth of 5 nm. The reason for this increase of the concentration in the bulk is the reduction of the concentration near the surface which increases the probability of clusters on the surface to diffuse into the bulk.

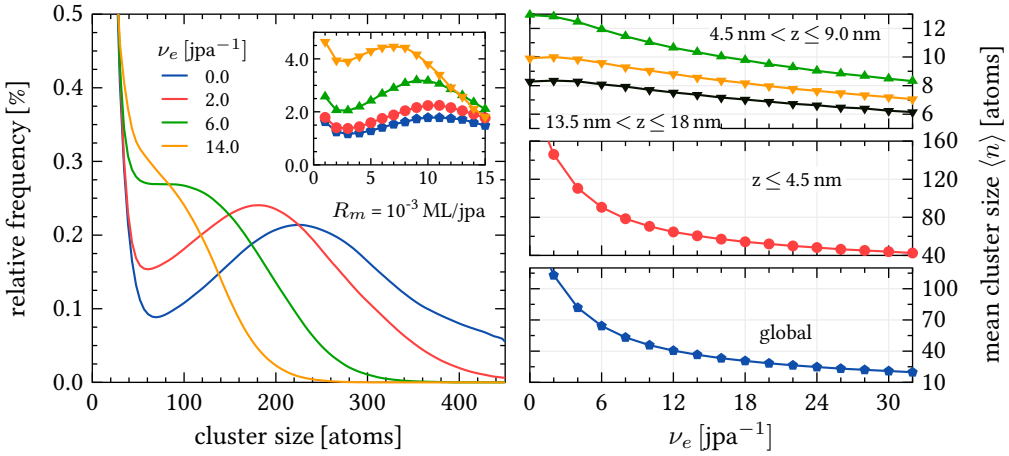

Figure 5.17: *Left: cluster size distributions for four different monomer evaporation rates ν_e ranging from 0.0 to 14.0 jpa^{-1}. Right: mean cluster size $\langle n \rangle$ as a function of the monomer evaporation rate ν_e. the bottom figure shows the global average. The upper figures show the averaged cluster size in thin layers of thickness 4.5 nm as indicated in the figure.*

5.3.2 Size Distributions

Corresponding to the reduction of the concentration near the surface, where the majority of large clusters grows, the mean size of clusters is significantly reduced due to the evaporation of atoms, which is depicted in the right panel Fig. 5.17. The left panel of Fig. 5.17 shows the distribution of cluster sizes for four different evaporation rates lying between 0.0 and 14.0 jpa^{-1}. The secondary maximum is shifted to smaller sizes with an increase of the evaporation rate and vanishes for $\nu_e \geq 6.0$ jpa^{-1}. The reason for this shift is the enhanced metal concentration at the surface which decreases the probability of surface clusters to capture each other and merge into larger clusters.

5.4 Interrupted Coalescence and Percolation

For high deposited thicknesses δ, metal clusters are expected to form a percolating network on the surface. By definition, percolation in thin films sets in if there exists a chain of overlapping clusters that connects one side of the surface with its opposite side [154]. Usually, systems that are studied with regard to percolation are characterized by the percolation coverage (sometimes also referred to as percolation threshold) ρ_c, which is the coverage of the surface at the moment when percolation sets in. Since diffusion of clusters into the bulk is possible in the present simulations, it is appropriate to additionally characterize the percolation transition by the amount of metal δ_c (referred to as critical thickness) that was deposited until percolation sets in.

To capture the effect of percolation in the simulations, it is crucial to impose further restrictions on the growth process leading to the formation of elongated structures of clusters (in the following referred to as chains). To this end, the assumption of unrestricted cluster growth is dropped and a cut-off radius r_c is introduced above which two overlapping clusters do not agglomerate. In the literature, this model is referred to as the interrupted coalescence model (ICM). It was introduced in the early 1990s by Yu et al. in order to study the coalescence of metal clusters in thin films [21]. In their simulations, Yu et al. neglected diffusion of clusters and investigated the dependence of the percolation coverage on the cut-off radius r_c. The ICM involves the following rules for two overlapping clusters with radii r_m and r_n:

1. If $r_m < r_c$ *or* $r_n < r_c$, the clusters agglomerate according to Eq. (4.3) and the new cluster is located at the center of mass of the two clusters.

2. If $r_m \geq r_c$ *and* $r_n \geq r_c$, the clusters do not coalesce but stay juxtaposed.

This section presents concentration profiles and cluster size distributions near the percolation threshold and discusses the dependence of the percolation threshold ρ_c on the monomer deposition rate R_m.

For all presented results below, the size of the surface is 600 nm $\times$ 600 nm. The simulations were stopped once percolation has set in.

5.4.1 Concentration Profiles and Size Distributions

Fig. 5.18 presents concentration profiles and cluster size distributions near the percolation threshold for different values of the monomer deposition rate. The critical radius was set to $r_c = 1.2\,\text{nm} = 8r_a$. On the whole, the shape of the curves is the same as in Sec. 5.1. However, especially the concentration profiles in Fig. 5.18 contain some disparities compared to Fig. 5.2. The most striking one is a significantly increased concentration near the surface which is due to the high amount of metal deposited on the surface (reaching from 27.56 ML ($R_m = 1.0 \times 10^{-5}$ ML/jpa) to 13.01 ML ($R_m = 1.0 \times 10^{-1}$ ML/jpa)). Deep in the bulk, the concentration is slightly enhanced for $R_m < 1.0 \times 10^{-2}$ ML/jpa, cf. Figs. 5.18 and 5.2. For $R_m \geq 1.0 \times 10^{-2}$ ML/jpa, the concentration is lowered. The reason for these opposite effects is a high surface coverage arising due to high deposition rates, see also

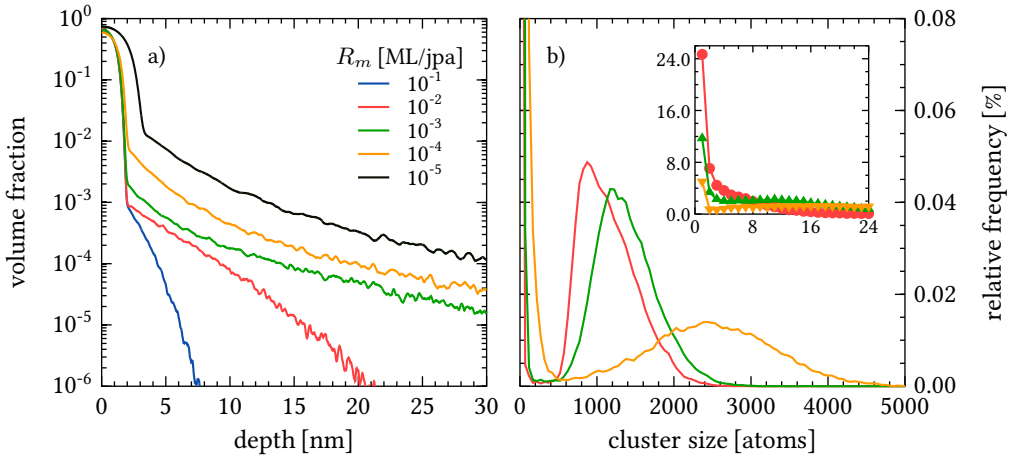

Figure 5.18: *Left: concentration profiles for five different monomer deposition rates. Right: cluster size distributions for three different values of the monomer deposition rate. The color coding is the same as in the left panel. The critical radius is $r_c = 1.2$ nm.*

the discussion in Sec. 5.1. High surface coverages cause a very strong immobilization of clusters near the surface which is obviously enhanced for large deposited thicknesses. In detail, this means that after a deposited thickness of $\delta = 2$ ML (which is the deposited thickness in Sec. 5.1) has been reached, further deposition of monomers leads to an immobilization of small clusters underneath the surface that could potentially diffuse deeper into the matrix. For deposition rates $R_m < 1.0 \times 10^{-2}$ ML/jpa the situation is different. Due to the comparable low surface coverage, further deposition of monomers leads to an enhanced diffusion of monomers and small clusters into the bulk.

The size distributions depicted in Fig. 5.18 b) also exhibit a bimodal shape with a strong peak at a size of $n = 1$ and a secondary maximum located between $n \approx 1000$ and $n \approx 2500$, which is almost one order of magnitude above the positions of the peaks in Fig. 5.5. The discussion of the size distributions is essentially the same as in Sec. 5.1.2, and hence not repeated here.

5.4.2 Percolation Transition

The percolation transition is investigated for different deposition rates R_m ranging from 1.0×10^{-5} to 9.0×10^{-1} ML/jpa. The results are averaged over 200 runs with a constant parameter set but different initial conditions. Fig. 5.19 presents the percolation threshold ρ_c and the critical thickness δ_c as a function of the deposition rate R_m. The percolation threshold ρ_c increases monotonically with the deposition rate R_m, which results from the trend towards more homogeneous cluster growth at high deposition rates. This naturally causes higher surface coverages, cf. Fig. 5.20. In contrast to that, the critical

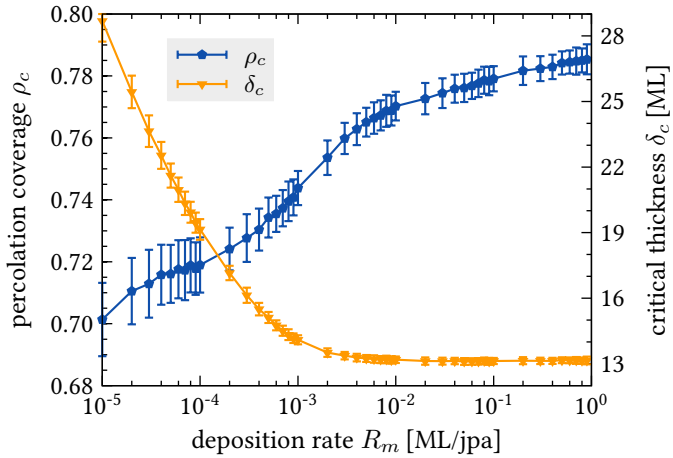

Figure 5.19: *Percolation coverage ρ_c and critical thickness δ_c as a function of the monomer deposition rate R_m.*

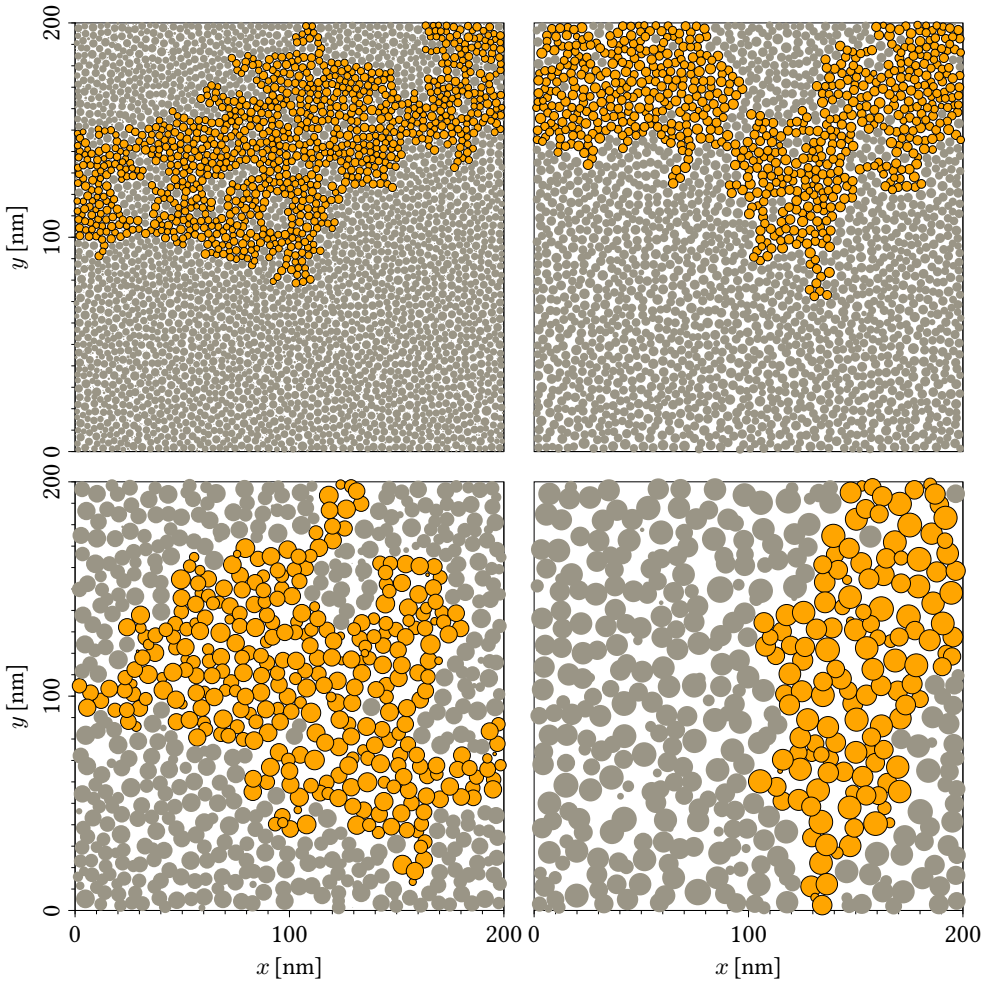

Figure 5.20: *Top view of the surface at the percolation threshold for four different deposition rates R_m and a critical radius $r_c = 8r_a = 1.2$ nm. Top left: $R_m = 9.0 \times 10^{-1}$ ML/jpa. Top right: $R_m = 5.0 \times 10^{-4}$ ML/jpa. Bottom left: $R_m = 1.0 \times 10^{-5}$ ML/jpa. Bottom right: $R_m = 2.0 \times 10^{-6}$ ML/jpa. Cluster islands that connect opposite sides of the surface are colored in orange.*

thickness δ_c exhibits the opposite behavior: δ_c starts at value of around 28 ML at $R_m = 1.0 \times 10^{-5}$ ML/jpa and rapidly decreases towards 13 ML at $R_m = 2.0 \times 10^{-3}$ ML/jpa where it starts to saturate. The reason for the high values of δ_c at low deposition rates is an enhanced diffusion of metal into the bulk, see Sec. 5.1.1, and a comparably slow cluster

growth. Hence, a large fraction of clusters does not participate in the formation of the percolating network on the surface.

CHAPTER 6

Co-Deposition of Metal and Polymer

Nanocomposite films consisting of metallic nanoparticles dispersed in an insulating polymer matrix can be used for many possible advanced technological materials with potential applications in optics [2, 28–30], electronics [9, 155] magnetics [32] and medicine [8], to name a few examples. For these purposes, vapor phase codeposition (VPCD) (see Sec. 2.3.1) of the metallic and the organic component has proven to be an efficient fabrication method since it offers good control of parameters such as the nanoparticle size, their shape, their spatial distribution [59] and the metallic filling factor [62].

This chapter is devoted to simulations of co-deposition of metal and polymer. It is divided into two sections. In the first section, simulations of composites with pure spherical particle growth are presented and discussed. Here, the main focus lies on the influence of two important parameters: the ratio of deposition rates $\kappa := R_m/R_p$ and the monomer evaporation rate ν_e. The second section deals with the growth of metallic nanocolumns which was discovered during co-deposition of a Fe-Ni-Co alloy and Teflon [42]. To study this growth morphology numerically, a second cluster growth mechanism leading to the formation of nanocolumns is incorporated into the simulations. Emphasis is placed on the analysis of the correlation between the transition from spherical cluster growth to nanocolumn formation and the steep increase of the metallic filling factor.

Two Remarks about the Simulations

1. In contrast to Chap. 5, all input parameters of the simulations are given in absolute units throughout this chapter. This is achieved by assuming a value of the surface diffusion constant of monomers D_1^s and determining the dimensionless time unit by means of D_1^s,

$$1\,\mathrm{ML} = 1/\nu_1^s = \frac{l^2}{4D_1^s}. \tag{6.1}$$

   The dimensionless values of the deposition rates R_m and R_p can then be computed via the definition of ML/jpa,

$$1\,\mathrm{ML/jpa} = \frac{4d_a D_1^s}{l^2}. \tag{6.2}$$

2. The ratio of deposition rates $\kappa := R_m/R_p$ is regulated by tuning the deposition rate R_p of the polymer matrix to the desired value.

6.1 Pure spherical Cluster Growth

For all simulation results discussed in this section, the composites have a finite thickness of 32 nm and a surface cross section of 700 nm × 700 nm. The metal deposition rate has a constant value of $R_m = 1.6$ nm/min and the surface diffusion constant is $D_1^s = 2.0 \times 10^{-12}$ cm^{-2}/s. The choice of the input parameters (except for the surface diffusion constant D_s^1) is motivated by a experiments of Takele et al. who investigated the optical

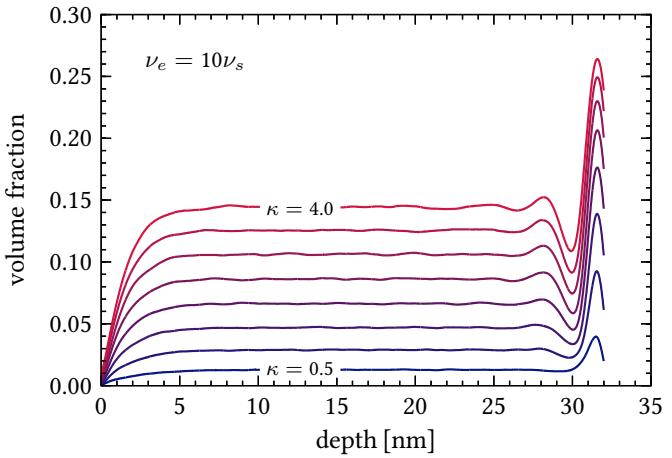

Figure 6.1: *Concentration profiles for eight different values of the deposition rate ratio κ in the parameter range $\kappa = 0.5, 1.0, \ldots 4.0$. The monomer evaporation rate is $\nu_e = 10\nu_s = 10$ ML/jpa.*

and electrical properties of nanocomposite films containing Au nanoparticles [28]. The simulations are stopped, once the composite reaches its final thickness.

Fig. 6.1 shows concentration profiles for eight different values of the deposition rate ratio κ between 0.5 and 4.0. Contrary to the concentration profiles for pure monomer deposition discussed in Chap. 5, where the concentration spans several orders of magnitude, the metal is almost constantly distributed over the whole composite. For all investigated values of κ the concentration profile can be divided into three parts: first a very small area in the direct vicinity of the surface with a strong increase of the concentration from a low value directly at the surface to a higher value a few nanometers below the surface. The second part is a broad region of constant concentration which is followed by a thin concentration peak near the bottom of the composite. This peak results from a high instantaneous condensation coefficient $\beta(t)$ at the beginning of the deposition, cf. Fig. 6.2. The instantaneous condensation coefficient is defined as the ratio of the number of adsorbed atoms per unit of time and the deposition rate [37, 156]. The reason for this high instantaneous condensation coefficient is the missing opportunity of clusters to diffuse deep into the bulk when the composite has a thickness of only a few nanometers.

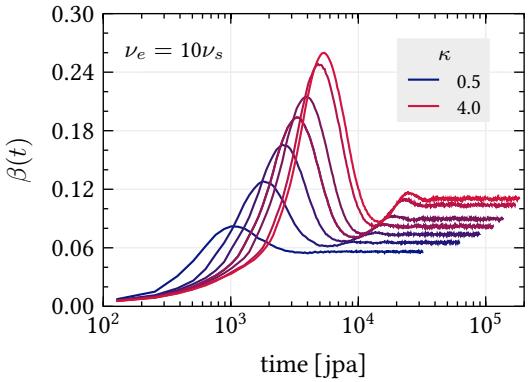

Figure 6.2: *Instantaneous condensation coefficient $\beta(t)$ as a function of time. The monomer evaporation rate ν_e is the same as in Fig. 6.1.*

Fig. 6.3 shows cluster size distributions for four different values of κ. The distributions exhibit a shape with two maxima whose positions show no variation with κ. The main peak of the distributions is contributed by monomers near the surface, which is not surprising since the simulations are stopped once the composite reaches a thickness of 32 nm. Consequently, monomers located at the surface do not have enough time to grow larger, cf. Fig. 6.4. The secondary maximum of all distributions shown in Fig. 6.3 is located at $n \approx 50$, whereby merely the intensity of the maximum varies with κ: the intensity decreases when κ gets larger. This is due to the fact that higher deposition rate ratios cause an accelerated cluster growth since direct impingement of monomers on clusters is more likely to occur. Thus, the fraction of clusters of sizes around the secondary maximum becomes smaller in support of larger clusters, which can be seen

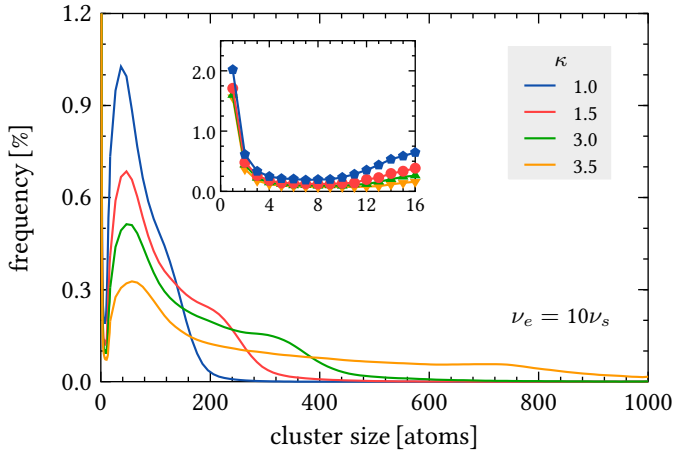

Figure 6.3: *Cluster size distributions for four different values of κ as indicated in the figure. The monomer evaporation rate is the same as in Fig. 6.1.*

from the long-drawn-out tail of the distribution at higher values of κ.

The effect of different monomer evaporation rates on different quantities is depicted in Fig. 6.5. Fig. 6.5 c) shows the mean cluster size $\langle n \rangle$ as a function of κ. The monomer evaporation rate is thereby given is units of the surface diffusion rate of monomers ν_1^s. A monomer evaporation rate $\nu_e = 2\nu_s^1$ means that the average time a monomer needs to evaporate from the surface is half of the average time between two surface diffusion jumps, see also Eq. (3.1.7). Expectably, the mean size $\langle n \rangle$ decreases at higher

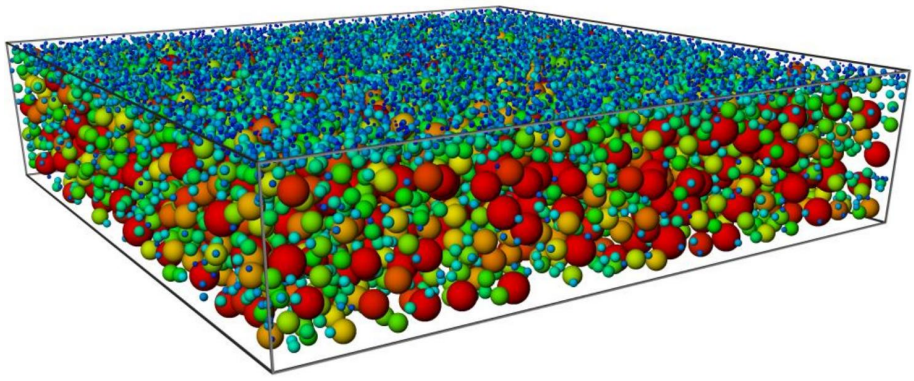

Figure 6.4: *Three-dimensional representation of the nanocomposite after termination of both deposition processes. Clusters are color coded according to their radius, whereby the color gradient reaches from blue (small clusters) to red (large clusters).*

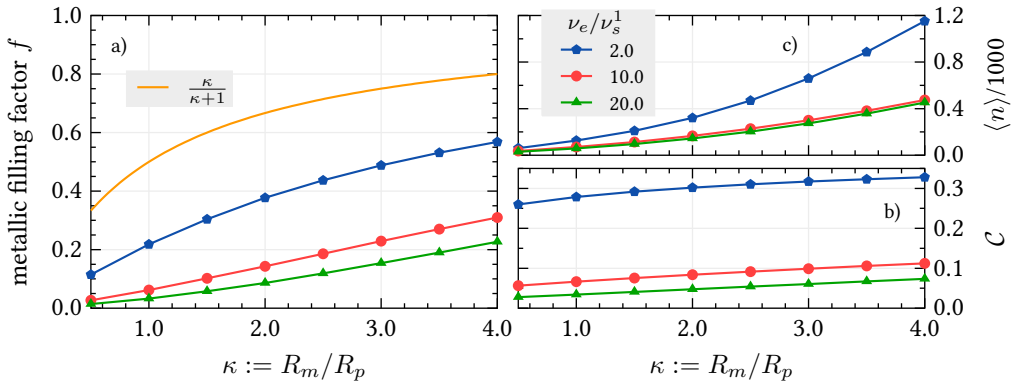

Figure 6.5: *Left: metallic filling factor as a function of the ratio of deposition rates κ for different evaporation rates as indicated in the right panel. Right: condensation coefficient $\mathcal{C}$ (bottom) and mean cluster size $\langle n\rangle$ divided by 1000 (top) as a function of κ.*

evaporation rates and increases monotonically with κ (for the same reason mentioned in the discussion of the cluster size distributions). For $\nu_e = 2\nu_s^1$ the mean size reaches a value near $\langle n\rangle \approx 1200$ at $\kappa = 4.0$, whereas for $\nu_e = 10(20)\nu_s^1$ $\langle n\rangle$ is lowered by a factor of about 3. The same effect is observable for the condensation coefficient $\mathcal{C}$, cf. Fig. 6.5 b). Here, the condensation coefficient has a value of about 0.3 for $\nu_e = 2.0\nu_s^1$ and $\kappa = 4.0$ and decreases towards a value around 0.1 (which is around the value Takele et al. have measured for Au co-deposited with Teflon [28]) if ν_e is increased to $\nu_e = 10.0\nu_s^1$.

The left panel of Fig. 6.5 shows the metallic factor as a function of κ. The metallic filling factor f is calculated from the ratio of the volume of the deposited metal V_m and the total volume V_{tot} of the composite:

$$f = \frac{V_m}{V_{tot}} = \frac{V_m}{V_m + V_p}\,, \tag{6.3}$$

where the total volume V_{tot} is the sum of the metal volume and the polymer volume. V_m and V_p can be expressed via the corresponding deposition rates of the metallic and the polymer component, R_m and R_p, respectively:

$$V_p = R_p L^2 t_d\,, \tag{6.4}$$

$$V_m = \mathcal{C} R_m L^2 t_d\,, \tag{6.5}$$

where L is the side length of the quadratic surface and t_d is the deposition time. For the calculation of the metal volume, the deposition rate R_m has to be multiplied by the

condensation coefficient $\mathcal{C}$. Inserting Eqs. (6.4) and (6.5) into the definition of the filling factor, Eq. (6.3), and taking into account that the condensation coefficient $\mathcal{C}$ is a function of κ yields the following expression:

$$f(\kappa) = \frac{\mathcal{C}(\kappa)R_m}{\mathcal{C}(\kappa)R_m + R_p} = \frac{\mathcal{C}(\kappa)\kappa}{\mathcal{C}(\kappa)\kappa + 1} = \frac{1}{1 + \frac{1}{\mathcal{C}(\kappa)\kappa}} \,. \tag{6.6}$$

The brown curve in Fig. 6.5 illustrates the course of the filling factor in case of full condensation, i.e. $\mathcal{C} = 1$. From Eq. (6.6) and Fig. 6.5, one can immediately see, how the condensation coefficient $\mathcal{C}$ and κ affect the filling factor: an increase of $\mathcal{C}$ as well as κ causes an increase of the metallic filing factor, which is clear because an enhanced condensation increases the fraction of metal by definition, and a high value of κ involves a lower polymer deposition rate R_p.

6.2 Self-organized Formation of metallic Nanocolumns

As already stated in Sec. 2.2.1, co-deposition of a Fe-Ni-Co alloy and Teflon AF has been found to lead to the self-organized formation of thin metallic nanocolumns under specific deposition conditions [42]. It was found that the transition from spherical to columnar growth takes place at a critical value of the ratio of deposition rates $\kappa := R_m/R_p$ and is accompanied by a steep increase of the metallic filling factor f. Fig. 6.7 shows the metal volume filling factor f as a function of the deposition rate ratio $\kappa = R_m/R_p$ at

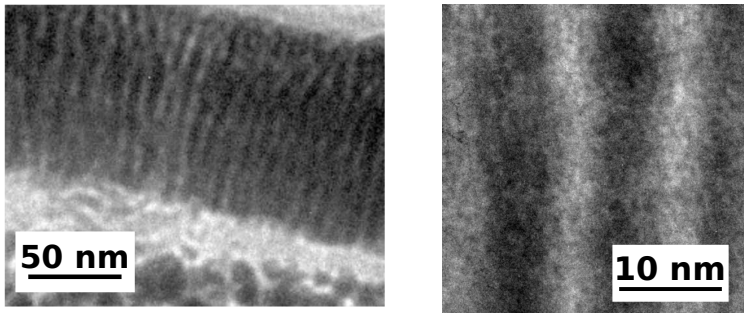

Figure 6.6: *Left: cross-sectional TEM image showing the formation of Fe-Ni-Co nanocolumns in Teflon AF on top of a layer of Ag clusters in Teflon AF isolated by 20 nm of the same matrix material. Right: cross-sectional higher magnified TEM image of self-organized nanocolumns of Fe-Ni-Co in Teflon AF. With kind permission reprinted from Ref. [42].*

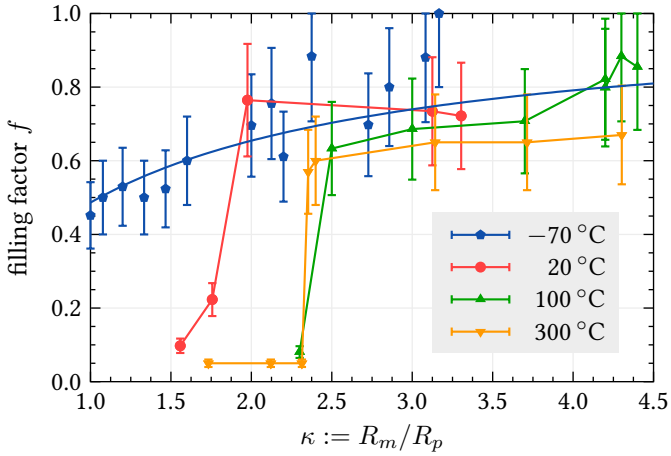

Figure 6.7: *Experimental results of the metallic filling factor as a function of the ratio of deposition rates κ of Fe-Ni-Co and Teflon AF for different temperatures. Reprinted from Ref. [97].*

different temperatures ranging from -70 to 300 °C. One can see that the steep increase of the filling factor is most pronounced at 300 °C and smears out at lower temperatures until it vanishes completely at -70 °C. For this temperature one can assume that the condensation coefficient is close to one for all values of κ. Therefore, the data were fitted to the function

$$f(\kappa) = \frac{1}{1 + \frac{1}{\mathcal{C}\kappa}}, \tag{6.7}$$

which is Eq. (6.6) for the case of condensation coefficients independent of κ. The fitting parameter is the metal condensation coefficient $\mathcal{C}$. The fit yields $\mathcal{C} = 0.94 \pm 0.08$ which is in good agreement with the expectation that the condensation coefficient approaches unity at low temperatures [135]. It has to be pointed out, however, that the condensation coefficient depends on the metal coverage at the surface of the growing composite and, hence, on κ because metal atoms stick with a probability of unity if they directly impinge on a metal nanoparticle or if they reach a metal nanoparticle via surface diffusion. Therefore, Eq. 6.7 is not applicable at higher temperatures, where the condensation coefficient on Teflon AF is expected to be very low due to thermal activation [39, 135]. Even the value of $\mathcal{C} = 0.94$ obtained at -70 °C probably overestimates the condensation coefficient for the pure polymer [97].

6.2.1 Simulation Details

The simulations are based on an extended version of the model described in Chap. 4 and involve the melting point depression of metal clusters. The main assumption is that

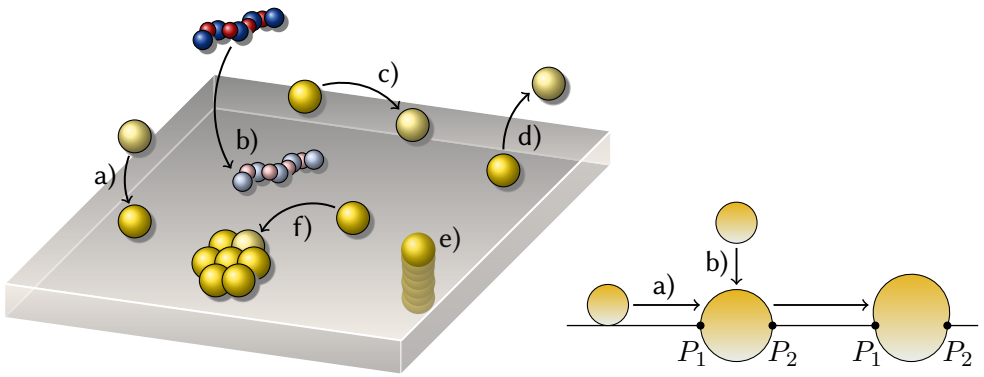

Figure 6.8: *Left: Sketch of the cluster processes included in the simulations: deposition of monomers a) and polymer b), surface diffusion of clusters c), evaporation of monomers d), formation of metallic nanocolumns e), cluster growth induced by surface diffusion f). Right: Illustration of the two basic mechanisms of nanocolumn growth: a) growth induced by surface diffusion and b) by direct impingement of a monomer on a preexisting cluster. The polymer surface moves upwards during the deposition process due to arrival of new organic molecules from the gas phase.*

clusters exist in the liquid state if their radius lies below the melting radius r_m and start to solidify by exceeding the melting radius. If clusters are liquid, they are assumed to merge according to (4.2). For clusters that grew beyond the melting radius, a second growth mechanism is introduced which leads to the formation of elongated columnar structures growing into the direction of the surface. It is initialized when the radius of one of two merging clusters is above the melting radius r_m, i.e. when the number of atoms N exceeds a certain value N_m. This growth occurs, for instance, when a monomer impinges directly into the interaction region of a pre-existing cluster with $N > N_m$ atoms which is partially buried by the surface. This process also occurs when a cluster merges with a partially buried cluster as a result of surface diffusion. It is assumed that the new cluster does not reach a spherical shape after equilibration. Instead, the incoming cluster coalesces with the part of the buried cluster which extends above the surface. These growth mechanisms are subject to two boundary conditions: the first one is volume conservation (due to the assumption of constant density). Furthermore the points P_1 and P_2 in Fig. 6.8 (denoting the circular intersection line of the cluster with the surface) are assumed to remain immobile. Hence, the resulting initial column consists of two spherical caps separated by the surface dividing the column into a buried part and a part located above the surface. Note that the intersection line of the clusters with the

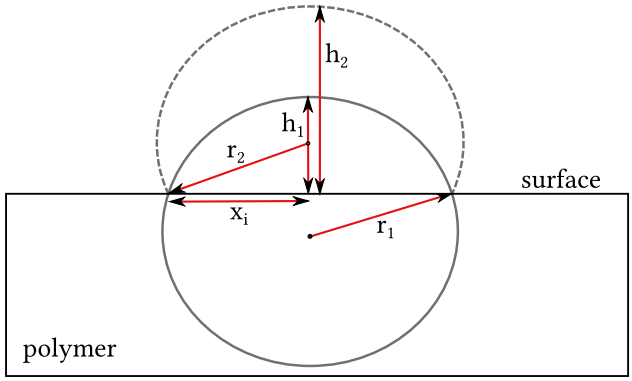

Figure 6.9: *Geometry of the column growth process induced by merging of a partially buried cluster with a free cluster.*

surface moves upwards during the deposition process due to the arrival of new organic molecules. These two mechanisms of nanocolumn growth are depicted in Fig. 6.8. These mechanisms can repeat the same way with a free cluster and a pre-existing column, where only the upper part of the column is involved into the growth process.

Fig. 6.9 shows the geometry of the nanocolumn growth process. Before merging, the volume amount of the buried cluster which lies above the surface is denoted as V_1, its height as h_1 and its curvature radius (which is the radius of the cluster) as r_1. The radius of the intersection circle of the cluster with the surface is labeled as x_i. The incoming cluster is assumed to have the volume ΔV such that the volume of the spherical cap is $V_2 = V_1 + \Delta V$ after merging. Then, the column growth process can be translated into the following formulas[1]:

$$\begin{aligned} &\text{before merging} && \text{after merging} \\ V_1 &= \frac{\pi h_1^2}{3}(3r_1 - h_1) & V_2 = V_1 + \Delta V &= \frac{\pi h_2^2}{3}(3r_2 - h_2) \\ x_i^2 &= 2r_1 h_1 - h_1^2 & x_i^2 &= 2r_2 h_2 - h_2^2\,, \end{aligned} \tag{6.8}$$

where r_2 is the curvature radius and h_2 is the height of the spherical cap after merging. Solving the bottom equation of the right-hand side of Eq. (6.8) for r_2 and inserting the resulting expression into the top equation of the right-hand side of Eq. (6.8) yields

$$h_2^3 + 3x_i^2 h_2 - \tilde{V} = 0, \quad \tilde{V} := 6V_2/\pi, \tag{6.9}$$

which is a depressed cubic equation for h_2. Since the discriminant $\mathcal{D} = \tilde{V}^2 + x_i^6$ of Eq. (6.9) is always positive, only one real solution for h_2 exists.

[1] The volume of a spherical cap with curvature radius r and height h is given by $V = \frac{\pi h^2}{3}(3r - h)$.

To incorporate the effect of very low condensation coefficients $\mathcal{C}$ known for metals on Teflon AF[39, 135], monomers are allowed to evaporate from the surface with a certain rate constant ν_e. The constant ν_e is given in units of the surface diffusion rate ν_s and is adjusted to the experimental values of $\mathcal{C}$.

Due to the fact that very little is known about the rates of surface diffusion of clusters on Teflon AF and evaporation of monomers from Teflon AF, the temperature is not incorporated into the simulations which is usually done by applying an Arrhenius law for the description of these processes. Instead, the main input parameters (e.g. surface diffusion and evaporation rate of monomers and the melting radius r_m) are treated as free parameters to achieve the best accordance with the experiments. To incorporate the size-dependence of the surface diffusion coefficients of metal clusters, the power law given by Eq. (4.8) is applied.

6.2.2 Results

To check the applicability of the simulation model, simulations were performed over a broad range of parameters. For all results presented below, the composites have a finite thickness of 100 nm and a surface cross section of 350 nm $\times$ 350 nm. The metal deposition rate R_m has a constant value of 1.5 nm/min. The melting radius r_m of the clusters is treated as a free parameter. For the surface diffusion coefficient of monomers D_1 and the evaporation rate ν_e of monomers, the following parameter range is used: $D_1 = 1 \times 10^{-11} \ldots 2 \times 10^{-10}\,\mathrm{cm^2/s}$ and $\nu_e = 1 \times 10^3 \ldots 2 \times 10^4\,\mathrm{s^{-1}}$. In order to obtain good statistics, the results presented below are averaged over 20 runs with a constant parameter set but different initial conditions. The deviations are usually less than one percent, so no error bars are included in the figures. The focus of the investigations lies on the influence of the monomer evaporation rate (desorption from the surface) and the surface diffusion rate, which depend on the metal-polymer interaction and hence on the condensation (or sticking) coefficient $\mathcal{C}$.

The main effect which was observed during experiments is a dramatic increase of the volume filling factor f with the deposition rate ratio κ. In contrast to the experiments, the simulations provide additional data such as the size distribution of clusters, their spatial distribution as well as the exact number of the nanocolumns. This allows for a more complete understanding of the self-organized process of nanocolumn growth. In Fig. 6.10 simulation results of different quantities as a function of the deposition rate ratio κ are shown for a system with a surface area of 350 nm $\times$ 350 nm and a final thickness (after the termination of both deposition processes) of 100 nm.

The simulations clearly show a strong increase of the metal filling factor f for values of $\kappa \geq 1.5$ which is related to the formation of nanocolumns cf. Fig. 6.10 a) and c). The upper panel of Fig. 6.10 which shows the number of nanocolumns indicates that there is a sharp transition from the pure spherical growth regime to a regime of column growth that coincides with the strong increase of the filling factor. Within our model the explanation of this phenomenon is as follows: When atoms impinge on the surface, they may undergo various competing processes like surface diffusion, re-emission and nucleation after encountering each other. One crucial point for the observed transition is the low condensation coefficient of metal on Teflon AF, which is caused by the weak chemical interaction of the two components. Metal atoms (clusters) have to encounter each other and form nuclei that can be stabilized in the polymer matrix and initiate the column growth. The simultaneous deposition of the polymer matrix works against the growth of nuclei and isolates the clusters from each other. For low values of κ the re-emission of atoms and the growth of the polymer matrix are the dominant processes and prevent the growth of clusters that are big enough to initiate column growth. When κ exceeds a critical value, the deposition of metal atoms plays the dominant role and the re-emission and isolation of clusters by the growing matrix is compensated by agglomeration of atoms with pre-existing clusters. As a consequence, the growth of

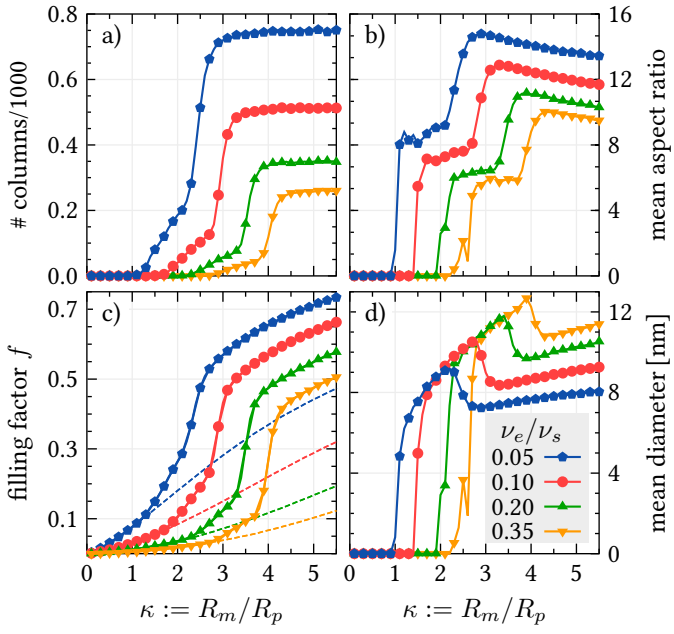

Figure 6.10: *Nanocolumn properties as a function of the deposition rate ratio κ, for four different values of the evaporation rate ν_e. The melting radius r_m is set to 2.23 nm and the monomer surface diffusion coefficient D_1 to $1.845 \times 10^{-11}\,\mathrm{cm}^2/\mathrm{s}$ (corresponding to the rate $\nu_s = 2.05 \times 10^4\,s^{-1}$). The figure parts show a) the total number of nanocolumns, b) the mean aspect ratio (defined as the ratio of the mean length to the mean diameter of the columns). c) the metal filling factor with (solid lines) and without (dashed lines) column growth d) the mean column diameter.*

clusters is strongly accelerated and some clusters reach the critical cluster size to initiate column growth.

Effect of atomic Desorption

Fig. 6.10 shows how the filling factor and geometrical properties of the nanocolumns are affected by the evaporation rate ν_e and the deposition rate ratio. The whole range of investigated values of κ can be divided into four regions: The first region is characterized by pure spherical growth and an almost linear increase of the metal filling factor, see Fig. 6.10 c). In the second region column growth sets in, see Fig. 6.10 a). With an increasing desorption rate and the concomitant increase in the surface diffusivity, the filling factor starts to increase nonlinearly and the transition to the columnar growth regime is shifted to larger values of κ, cf. Fig. 6.10 a). This effect can be easily understood in terms of the underlying column growth model: As explained in Sec. 6.2.1, clusters have to grow beyond the melting size r_m to act as initial nuclei for column growth. When the desorption rate of atoms ν_e from the surface increases the growth of clusters is slowed down. Consequently, the probability of cluster growth can only be enhanced by slowing down the embedding of clusters into the matrix via increasing the mobility of clusters which occurs when κ is increased (recall that κ is increased via reduction of the polymer deposition rate R_p). A further effect of increasing the atomic desorption is a reduction of the total number of columns. This is a direct consequence of the enhanced probability of atom re-emission. This effect can also be seen in Fig. 6.11 which shows a top view of the composite after termination of deposition: clearly the columns grow thicker with higher desorption rates.

The second stage is characterized by a relatively small rise of the number of columns with increasing κ. During this stage the columns are steadily growing thicker and whereas their aspect ratio remains within a relatively narrow range see Fig. 6.10 b). This, obviously, implies that the mean column length is also increasing at a comparable rate. Also, the diameter of the columns increases when the desorption rate is increased.

The third stage can be identified by an abrupt increase of the total number of columns. From Fig. 6.10 c) one can see that the accelerated growth of columns is accompanied by a steep rise of the filling factor, which is more pronounced for higher desorption rates. Our simulations show that this stage comes along with a growing number of columns extending over the whole height of the final composite, resulting in a higher metal coverage of the surface. The mean column diameter is decreasing during this stage due to the increased number of nuclei available for column growth. This gives rise to a

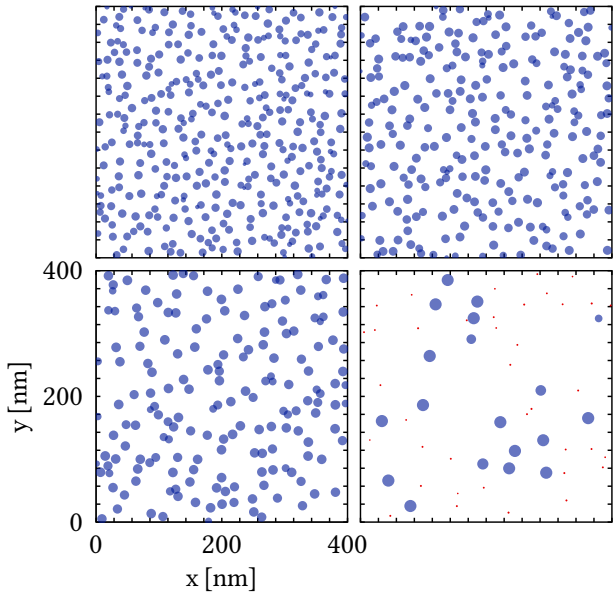

Figure 6.11: *Top view of the surface microstructure after termination of both deposition processes for $\kappa = 0.4$ and four different evaporation rates ν_e. Top left: $\nu_e = 2.05 \times 10^3\ s^{-1}$, top right: $\nu_e = 4.1 \times 10^{3\ -1}$, bottom left: $\nu_e = 8.2 \times 10^3\ s^{-1}$, bottom right: $\nu_e = 1.64 \times 10^4\ s^{-1}$. Other parameters are the same as in Fig. 6.10. Columns (clusters) are depicted as blue (red) circles. The size of the surface is the same in all figures.*

significantly higher aspect ratio. Our simulations show that the average height of the nanocolumns is even some nanometers larger than the thickness of the substrate, see Fig. 6.13, i.e. the majority of the columns extends above the surface. Consequently the incoming atoms are distributed among a larger number of columns compared to the previous stage.

During the fourth growth stage that starts between $\kappa \approx 3.0$ (blue curve in Fig. 6.10 c)) and $\kappa \approx 4.2$ (brown curve), the number and average length of columns remain constant. Only the filling factor and the column diameter increase (and, therefore, the aspect ratio decreases), due to the higher amount of metal atoms impinging on the surface.

Effect of Surface Diffusion

In Fig. 6.12, the same quantities are depicted as in Fig. 6.10, but for a fixed desorption rate $\nu_e = 4.92 \times 10^3\ s^{-1}$ and different surface diffusion coefficients D_1. The main effect of increasing D_1 is a shift of the transition from spherical growth to columnar growth to smaller values of κ, see Fig. 6.12 a) and c). The reason is obviously the accelerated cluster growth caused by a higher mobility. While for slow surface diffusion the cluster growth is dominated by direct impingement of atoms on pre-existing clusters, for fast surface diffusion the probability of two clusters to encounter each other during surface diffusion

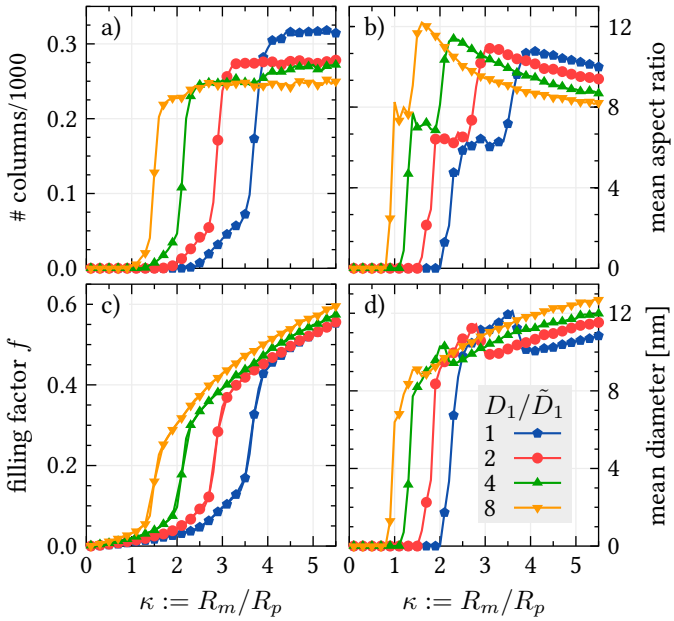

Figure 6.12: *Same as Fig. 6.10, but for the case of different surface diffusion coefficients D_1 of monomers. The constant $\tilde{D}_1$ is set to $1.845 \times 10^{-11}\,\mathrm{cm}^2/\mathrm{s}$. The evaporation rate equals $\nu_e = 4.92 \times 10^3\,s^{-1}$.*

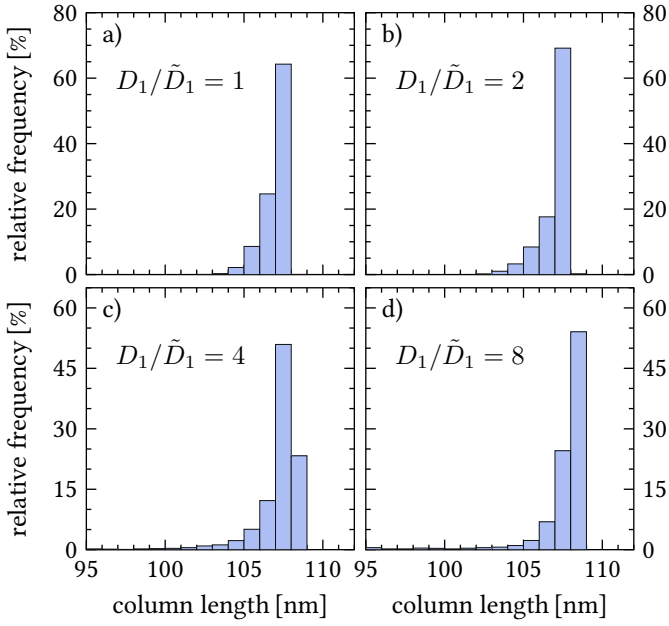

Figure 6.13: *Distribution of column lengths for $\kappa = 4.0$ depicted in a histogram with a resolution of 1 nm. The parameter set is the same as in Fig. 6.12.*

is considerably enhanced. As a consequence, clusters reach the critical nucleus size to induce the columnar growth already for smaller values of κ. Interestingly, the filling factors for higher values of κ ($\geq$ 4.4) lie very close together. The simulations do not show a tendency of the surface diffusion coefficient to influence the filling factor. Other quantities are also weakly affected by the diffusion constant, when columnar growth is observed. Fig. 6.12 a) shows that for all simulations the number of columns lies between 200 and 300 what corresponds to a column surface density between 1.63×10^{-3} nm^{-2} and 2.12×10^{-3} nm^{-2}, where the density is higher the lower is D_1. As one can see in Fig. 6.12 d), the thickness of the columns follows the opposite trend: A higher surface diffusivity leads to thicker columns, which is not surprising since clusters grow faster. The aspect ratio shows the opposite trend, cf. Fig. 6.12 b). This implies that, in the simulated range of D_1, the average length of the nanocolumns stays nearly constant.

Fig. 6.13 shows the distribution of column lengths after termination of both deposition processes, for four different surface diffusion coefficients. All columns extend some nanometers above the surface (which is located at 100 nm). Furthermore, for all values of D_1 the length distribution is very narrow with a maximum at about 108 nm.

CHAPTER 7

Conclusions

The present thesis was concerned with the analysis of the coupled cluster processes which occur during the formation of metal-polymer nanocomposites by means of kinetic Monte Carlo simulations. Due to the simplicity of the underlying model, the simulations allowed for the investigation of macroscopic systems with a cross section of up to 4.0 µm containing several million clusters Since several input parameters such as the exact diffusion and evaporation rates, and the averaged diffusion jump length of clusters are not known exactly, it was not the aim of this study to reproduce experimental outcomes quantitatively. Instead the simulations served to analyze qualitative changes of the microstructure of the nanocomposite due to variations of the deposition conditions and to get further insight into the mechanisms behind these changes.

Metal-Polymer Interface formation

The first part dealt with the formation of a metal-polymer interface under different conditions. Here, important trends of key quantities such as the metal concentration inside the bulk and the size distribution of clusters related to the variation of parameters such as the atomic deposition rate, the evaporation rate and the density of defects were identified and discussed.

In accordance with previous numerical studies [22, 24] and experimental results [35, 152, 153], a distinct bimodal size distribution of metal clusters was found. The size region around the main maximum of the size spectrum, which is located at sizes between $n = 2$

and $n = 20$, could clearly be identified as resulting from the majority of clusters being distributed to a large spatial extent deep inside the polymer matrix. On the other hand, the secondary maximum is located at much larger cluster sizes and could be attributed to clusters located in a thin layer underneath the surface. It has been shown that the position of these maximums can easily be controlled by tuning the atomic deposition rate R_m, where higher deposition rates result in more distinct maximums located at smaller cluster sizes. Furthermore, the position of the maximums could be affected by the density of surface defects as well as the evaporation rate of monomers. The presence of surface defects has lead to a shift of the secondary maximum to smaller sizes and a simultaneous narrowing. Low evaporation rates have also shifted the secondary maximum to smaller sizes but did not change the intensity of the peak. At high evaporation rates the two maximums merged and the distribution lost its bimodal shape.

The concentration profile has been found to be in a tripartite shape with a strong hold-up of clusters in the vicinity of the surface, a narrow region with a steep decrease of concentration and a large area with a small concentration allowing for an almost uncorrelated diffusion of small clusters. Surface defects had, in accordance with experiments [43], the effect of substantially lowering the metal concentration in the polymer matrix and fixing clusters at the surface. Evaporation of monomers was found to cause an overall lowering of the the metal concentration.

The last section of this part dealt with simulations of very high deposition thicknesses δ leading to the formation of a percolating network at the surface. To simulate this realistically, the main assumptions of the interrupted coalescence model [21] were integrated into the simulations. Among the discussion of the concentration profile and the size distribution, which exhibited essentially the same features as for lower values δ, emphasis was placed on the percolation transition and the influence of the deposition rate R_m on the percolation threshold. It has been shown that the critical percolation coverage ρ_c monotonically increases with the deposition rate. This effect could be addressed to the homogenization of cluster growth at high deposition rates.

Formation of Nanocolumns

The last chapter was concerned with simulations of co-deposition of metal and polymer. In the first section of this chapter, the general features of the concentration profiles and size distributions obtained from the simulations were discussed. Here, the main variation parameter was the ratio κ of the metal deposition rate R_m and the polymer deposition rate R_p. The concentration profiles have shown a concentration peak at the

bottom of the composite resulting from an enhanced instantaneous condensation of monomers at the beginning of the deposition. The size distribution exhibited a shape with one maximum contributed by monomers and one maximum at larger sizes.

The main objective of the last section was to develop a simulation model that allows for a detailed analysis of the self-organized growth of nanocolumns, which was discovered during co-deposition of a Fe-Ni-Co alloy and Teflon [42]. The model involves a second growth mechanism for larges clusters leading to formation of the elongated columns growing into the direction of the surface. The simulations were able to reproduce the steep increase of the metallic filling factor at a critical value of the ratio of deposition rates κ, which was found in experiments. The increase of the filling factor could be addressed to the beginning growth of nanocolumns. The correlation between the increase of the filling factor and the transition from spherical to columnar growth was subject to a detailed discussion.

APPENDIX A

Frequently Used Acronyms

CTMC	continuous-time Markov chain	24
DTMC	discrete-time Markov chain	24
KMC	kinetic Monte Carlo	11
MC	Monte Carlo	21
MD	Molecular dynamics	21
FR	first reaction	25
BKL	Bortz-Kalos-Lebowitz	30
CDF	cumulative distribution function	28
PDF	probability density function	29
FVT	free volume theory	47
ML	monolayer	44
FMM	Family and Meakin model	22
ICM	interrupted coalescence model	21
jpa	jumps per atom	47
i.e.d.	independent exponentially distributed	30
PC	polycarbonate	14

PS	polystyrene . . . 14
TEM	transmission electron microscopy . . . 10
XPS	X-ray photoelectron spectroscopy . . . 14
PVD	physical vapor deposition . . . 15
VPCD	vapor phase codeposition . . . 75
CVD	chemical vapor deposition . . . 19
CSD	chemical solution deposition . . . 20
VPD	vapor phase deposition . . . 15
PECVD	plasma enhanced chemical vapor deposition . . . 20
PHCVD	photon induced chemical vapor deposition . . . 20
RF	radio frequency . . . 17
DC	direct current . . . 18
AC	alternate current . . . 18
PS	polystyrene . . . 14
PMDA-ODA	pyromellitic dianhydride-oxydianiline . . . 12
TMC-PC	trimethylcyclohexane polycarbonate . . . 11

APPENDIX B

Frequently used Symbols

Symbol	Explanation
$D_{\mathrm{n}}^{b/s}$	bulk/surface diffusion coefficient of a cluster with n atoms
$\nu_{\mathrm{n}}^{b/s}$	bulk/surface diffusion rate of a cluster with n atoms
ν_e	monomer evaporation rate
R_m	metal deposition rate
R_p	polymer deposition rate
δ	total amount of deposited atoms
t_d	time duration of deposition
κ	ratio of metal and polymer deposition rates
f	metallic filling factor
$\mathcal{C}$	condensation (sticking) coefficient
$\beta(t)$	instantaneous condensation coefficient
σ	metallic coverage of the surface
T_g	glass transition temperature
$\langle n \rangle$	mean cluster size
r_c	cut-off radius of cluster growth
ρ_c	critical percolation coverage
δ_c	critical percolation thickness
r_m	melting radius of a cluster

Bibliography

[1] A. Biswas, O. Aktas, J. Kanzow, U. Saeed, T. Strunskus, V. Zaporojtchenko, and F. Faupel. "*Polymer–metal optical nanocomposites with tunable particle plasmon resonance prepared by vapor phase co-deposition*". Mater. Lett. **58**, 1530 (2004); (pp. 1, 8).

[2] A. Biswas, O. C. Aktas, U. Schürmann, U. Saeed, V. Zaporojtchenko, F. Faupel, and T. Strunskus. "*Tunable multiple plasmon resonance wavelengths response from multicomponent polymer-metal nanocomposite systems*". Appl. Phys. Lett. **84**, 2655 (2004); (pp. 1, 8, 75).

[3] T. A. Fulton and G. J. Dolan. "*Observation of single-electron charging effects in small tunnel junctions*". Phys. Rev. Lett. **59**, 109 (1987); (pp. 1, 7).

[4] H. Graf, J. Vancea, and H. Hoffmann. "*Single-electron tunneling at room temperature in cobalt nanoparticles*". Appl. Phys. Lett. **80**, 1264 (2002); (pp. 1, 7).

[5] H. Takele, S. Jebril, T. Strunskus, V. Zaporojchenko, R. Adelung, and F. Faupel. "*Tuning of electrical and structural properties of metal-polymer nanocomposite films prepared by co-evaporation technique*". Appl. Phys. A, **92**, 345 (2008); (pp. 1, 7).

[6] M. Karttunen, P. Ruuskanen, V. Pitkänen, and W. Albers. "*Electrically Conductive Metal Polymer Nanocomposites for Electronics Applications*". J. Electron. Mater. **37**, 951 (2008); (pp. 1, 7).

[7] A. Emamifar. "*Applications of Antimicrobial Polymer Nanocomposites in Food Packaging*". In: A. Hashim (ed.), *Advances in Nanocomposite Technology*, (pp. 299–318). InTech, Rijeka, 2011; (pp. 1, 8).

[8] R. F. FAN and A. J. BARD. "*Chemical, Electrochemical, Gravimetric, and Microscopic Studies on Antimicrobial Silver Films*". J. Phys. Chem. B, **106**, 279 (2002); (pp. 1, 75).

[9] F. FAUPEL, V. ZAPOROJTCHENKO, H. GREVE, U. SCHÜRMANN, V. S. K. CHAKRAVADHANULA, C. HANISCH, A. KULKARNI, A. GERBER, E. QUANDT, and R. PODSCHUN. "*Deposition of Nanocomposites by Plasmas*". Contrib. Plasma Phys. **47**, 537 (2007); (pp. 1, 8, 16, 75).

[10] A. P. JACKSON, J. F. V. VINCENT, and R. M. TURNER. "*The Mechanical Design of Nacre*". Proc. R. Soc. Lond. B, **234**, 415 (1988); (p. 1).

[11] A. FINNEMORE, P. CUNHA, T. SHEAN, S. VIGNOLINI, S. GULDIN, M. OYEN, and U. STEINER. "*Biomimetic layer-by-layer assembly of artificial nacre*". Nat. Commun. **3**, 966 (2012); (p. 1).

[12] A. SELLINGER, P. M. WEISS, A. NGUYEN, Y. LU, R. A. ASSINK, W. GONG, and C. J. BRINKER. "*Continuous self-assembly of organic–inorganic nanocomposite coatings that mimic nacre*". Nature, **394**, 256 (1998); (p. 1).

[13] A. D. POMOGAILO and V. N. KESTELMAN. *Springer Series in Materials Science, Vol. 81. Metallopolymer Nanocomposites*. 1st ed. Springer, Berlin Heidelberg New York, 2005; (pp. 1, 8–9, 15, 19–20).

[14] F. FAUPEL, V. ZAPOROJTCHENKO, T. STUNSKUS, J. ERICHSEN, K. DOLGNER, A. THRAN, and M. KIENE. "*Fundamental Aspects of Polymer Metallization*". In: E. SACHER (ed.), *Metallization of Polymers 2*, (pp. 73–96). Kluwer Academic/Plenum Publishers, New York, 2002; (pp. 2, 8, 10–12, 15, 48).

[15] B. CARLBERG, T. WANG, J. LIU, and D. SHANGGUAN. "*Polymer-metal nano-composite films for thermal management*". Microelectron. Int. **26**, 28 (2009); (p. 2).

[16] N. LU, X. WANG, Z. SUO, and J. VLASSAK. "*Metal films on polymer substrates stretched beyond 50%*". Appl. Phys. Lett. **91**, 221909 (2007); (p. 2).

[17] R. M. TROMP. "*Interdiffusion at the polyimide–Cu interface*". J. Vac. Sci. Technol. A, **3**, 782 (1985); (pp. 2, 11–12).

[18] F. K. LEGOUES. "*The microstructure of metal-polyimide interfaces*". J. Vac. Sci. Technol. A, **6**, 2200 (1988); (pp. 2, 11–12, 21).

[19] S. P. Kowalczyk, Y.-H. Kim, G. F. Walker, and J. Kim. "*Polyimide on copper: The role of solvent in the formation of copper precipitates*". Appl. Phys. Lett. **52**, 375 (1988); (p. 2).

[20] A. B. Bortz, M. H. Kalos, and J. L. Lebowitz. "*A new algorithm for Monte Carlo simulation of Ising spin systems*". J. Comput. Phys. **17**, 10 (1975); (pp. 2, 24–25, 38, 43).

[21] X. Yu, P. M. Duxbury, G. Jeffers, and M. A. Dubson. "*Coalescence and percolation in thin metal films*". Phys. Rev. B, **44**, 13163 (1991); (pp. 2, 10, 21–22, 46, 70, 92).

[22] A. Thran and F. Faupel. "*Computer Simulation of Metal Diffusion in Polymers*". Defect Diffus. Forum, **143-147**, 903 (1997); (pp. 2, 21, 44, 91).

[23] P. Jensen. "*Growth of nanostructures by cluster deposition: Experiments and simple models*". Rev. Mod. Phys. **71**, 1695 (1999); (pp. 2, 22, 43, 48).

[24] A. Thran. "*Diffusion von Gasen und Metallen in Polymeren: Datenanalysen, Experimente und Simulationen*". PhD thesis, Christian-Albrechts-Universität zu Kiel, Kiel, 2000; (pp. 2, 21, 56, 91).

[25] B. M. Smirnov. *Cluster Processes in Gases and Plasmas*. Wiley-VCH, Weinheim, 2010; (pp. 2, 45).

[26] P. M. Ajayan, L. S. Schadler, and P. V. Braun. *Nanocomposite Science and Technology*. Wiley-VCH, Weinheim, 2003; (pp. 7, 20).

[27] A. E. Berkowitz, J. R. Mitchell, M. J. Carey, A. P. Young, S. Zhang, F. E. Spada, F. T. Parker, A. Hutten, and G. Thomas. "*Giant magnetoresistance in heterogeneous Cu-Co alloys*". Phys. Rev. Lett. **68**, 3745 (1992); (p. 8).

[28] H. Takele, U. Schürmann, H. Greve, D. Paretkar, V. Zaporojtchenko, and F. Faupel. "*Controlled growth of Au nanoparticles in co-evaporated metal/polymer composite films and their optical and electrical properties*". Eur. Phys. J. Appl. Phys. **33**, 83 (2006); (pp. 8, 75, 77, 79).

[29] A. Biswas, H. Eilers, F. Hidden, O. C. Aktas, and C. V. S. Kiran. "*Large broadband visible to infrared plasmonic absorption from Ag nanoparticles with a fractal structure embedded in a Teflon AF® matrix*". Appl. Phys. Lett. **88**, 013103 (2006); (pp. 8, 75).

[30] H. TAKELE, H. GREVE, C. POCHSTEIN, V. ZAPOROJTCHENKO, and F. FAUPEL. "*Plasmonic properties of Ag nanoclusters in various polymer matrices.*" Nanotechnology, **17**, 3499 (2006); (pp. 8–9, 75).

[31] W. CASERI. "*Nanocomposites of polymers and metals or semiconductors: Historical background and optical properties*". Macromol. Rapid Comm. **21**, 705 (2000); (pp. 8, 20).

[32] J. OUYANG, C.-W. CHU, C. R. SZMANDA, L. MA, and Y. YANG. "*Programmable polymer thin film and non-volatile memory device.*" Nat. Mater. **3**, 918 (2004); (pp. 8, 75).

[33] F. FAUPEL, V. ZAPOROJTCHENKO, T. STRUNSKUS, and M. ELBAHRI. "*Metal-Polymer Nanocomposites for Functional Applications*". Adv. Eng. Mater. **12**, 1177 (2010); (pp. 8, 16, 18, 20).

[34] H.-J. BUTT and M. KAPPL. *Surface and Interfacial Forces*. 1st ed. Wiley-VCH, Weinheim, 2010; (p. 9).

[35] F. FAUPEL, R. WILLECKE, and A. THRAN. "*Diffusion of metals in polymers*". Mat. Sci. Eng. R, **22**, 1 (1998); (pp. 9, 12, 14, 48, 59, 91).

[36] F. FAUPEL, V. ZAPOROJTCHENKO, A. THRAN, T. STUNSKUS, and M. KIENE. "*Metal Diffusion in Polymers and on Polymer Surfaces*". In: D. GUPTA (ed.), *Diffusion Processes in Advanced Technological Materials*, (pp. 333–363). Springer, New York, 2005; (pp. 9–10, 14–15, 47).

[37] V. ZAPOROJTCHENKO, K. BEHNKE, A. THRAN, T. STRUNSKUS, and F. FAUPEL. "*Condensation coefficients and initial stages of growth for noble metals deposited onto chemically different polymer surfaces*". Appl. Surf. Sci. **144**, 355 (1999); (pp. 10, 15, 45, 49, 77).

[38] V. ZAPOROJTCHENKO, T. STRUNSKUS, K. BEHNKE, C. VON BECHTOLSHEIM, A. THRAN, and F. FAUPEL. "*Formation of metal–polymer interfaces by metal evaporation: influence of deposition parameters and defects*". Microelectron. Eng. **50**, 465 (2000); (pp. 10, 44, 53, 64).

[39] A. THRAN, M. KIENE, V. ZAPOROJTCHENKO, and F. FAUPEL. "*Condensation Coefficients of Ag on Polymers*". Phys. Rev. Lett. **82**, 1903 (1999); (pp. 10, 15, 46, 81, 84).

[40] V. Zaporojtchenko, K. Behnke, T. Strunskus, and F. Faupel. "*Condensation coefficients of noble metals on polymers: a novel method of determination by x-ray photoelectron spectroscopy*". Surf. Interface Anal. **30**, 439 (2000); (pp. 10, 15).

[41] G. Jeffers, M. A. Dubson, and P. M. Duxbury. "*Island-to-percolation transition during growth of metal films*". J. Appl. Phys. **75**, 5016 (1994); (p. 10).

[42] H. Greve, A. Biswas, U. Schürmann, V. Zaporojtchenko, and F. Faupel. "*Self-organization of ultrahigh-density Fe–Ni–Co nanocolumns in Teflon® AF*". Appl. Phys. Lett. **88**, 123103 (2006); (pp. 10–11, 16, 75, 80, 93).

[43] A. Thran, T. Strunskus, V. Zaporojtchenko, and F. Faupel. "*Evidence of noble metal diffusion in polymers at room temperature and its retardation by a chromium barrier*". Appl. Phys. Lett. **81**, 244 (2002); (pp. 11–13, 44, 53, 64, 92).

[44] C. von Bechtolsheim, V. Zaporojtchenko, and F. Faupel. "*Influence of thermal treatment on the morphology and adhesion of gold films on trimethylcyclohexane-polycarbonat*". Appl. Surf. Sci. **151**, 119 (1999); (pp. 11, 47).

[45] J. Wetzel, D. Smith, and G. Appleby-Mougham. "*The Microstructure of Copper Films Deposited by E-Beam Evaporation onto Thin Polyimide Films*". Res. Soc. Symp. Proc. **40**, 271 (1984); (p. 11).

[46] F. Faupel, R. Willecke, A. Thran, M. Kiene, C. von Bechtolsheim, and T. Strunskus. "*Metal Diffusion in Polymers*". Defect Diffus. Forum, **143-147**, 887 (1997); (p. 12).

[47] M. Kiene, T. Strunskus, R. Peter, and F. Faupel. "*Evidence of Aggregation-Induced Copper Immobilization During Polyimide Metallization*". Adv. Mater. **10**, 1357 (1998); (p. 12).

[48] A. Foitzik and F. Faupel. "*Structural Investigation of the Silver-Polyimide Interface by Cross-Sectional Tem and Ion-Beam Sputtering*". Mater. Res. Soc. Symp. Proc. **203**, 59 (1991); (p. 12).

[49] F. Faupel. "*Diffusion in Non-Crystalline Metallic and Organic Media*". phys. stat. sol. (a), **134**, 9 (1992); (pp. 12, 14).

[50] F. Faupel. "*An apparatus for ion-beam sputtering and its application to high-resolution radiotracer depth profiling of diffusion samples*". J. Vac. Sci. Technol. A, **10**, 92 (1992); (p. 12).

[51] R. WILLECKE and F. FAUPEL. "*Diffusion of gold and silver in bisphenol trimethylcyclohexanen polycarbonate*". J. Polym. Sci. Poly. Phys. **35**, 1043 (1997); (pp. 12–13).

[52] R. WEBER. "*Oberflächenempfindliche Röntgenstreuung an Polymer-Metall Grenzflächen: Strukturelle Eigenchaften und thermisches Verhalten*". PhD thesis, Christian-Albrechts-Universität zu Kiel, Kiel, 2002; (p. 13).

[53] G. J. KOVACS. "*Summary Abstract: Formation of novel vacuum evaporated submicron particulate monolayers just beneath a heated polymer surface*". J. Vac. Sci. Technol. **20**, 419 (1982); (p. 14).

[54] G. KOVACS, P. VINCETT, C. TREMBLAY, and A. PUNDSACK. "*Vacuum deposition onto softenable substrates: Formation of novel subsurface structures*". Thin Solid Films, **101**, 21 (1983); (p. 14).

[55] V. ZAPOROJTCHENKO, T. STRUNSKUS, J. ERICHSEN, and F. FAUPEL. "*Embedding of Noble Metal Nanoclusters into Polymers as a Potential Probe of the Surface Glass Transition*". Macromolecules, **34**, 1125 (2001); (pp. 14, 45).

[56] D. MATTOX. *Handbook of physical Vapor Deposition (PVD) Processing*. Noyes Publications, Park Ridge, New Jersey, U.S.A., 1998; (p. 15).

[57] U. SCHÜRMANN, W. HARTUNG, H. TAKELE, V. ZAPOROJTCHENKO, and F. FAUPEL. "*Controlled syntheses of Ag-polytetrafluoroethylene nanocomposite thin films by co-sputtering from two magnetron sources*". Nanotechnology, **16**, 1078 (2005); (p. 16).

[58] N. BOONTHANOM and M. WHITE. "*Polymer-metal composite films*". Thin Solid Films, **24**, 295 (1974); (p. 16).

[59] V. ZAPOROJTCHENKO, J. ZEKONYTE, A. BISWAS, and F. FAUPEL. "*Controlled growth of nano-size metal clusters on polymers by using VPD method*". Surf. Sci. **532**, 300 (2003); (pp. 16, 75).

[60] H. BIEDERMAN. "*Nanocomposites and nanostructures based on plasma polymers*". Surf. Coat. Tech. **205**, S10 (2011); (pp. 16–17).

[61] H. BIEDERMAN, O. KYLIAN, M. DRABIK, A. CHOUKOUROV, O. POLONSKYI, and P. SOLAR. "*Nanocomposite and nanostructured films with plasma polymer matrix*". Surf. Coat. Tech. **211**, 127 (2012); (p. 16).

[62] A. Biswas, Z. Marton, J. Kanzow, J. Kruse, V. Zaporojtchenko, F. Faupel, and T. Strunskus. "*Controlled Generation of Ni Nanoparticles in the Capping Layers of Teflon AF by Vapor-Phase Tandem Evaporation*". Nano. Lett. **3**, 69 (2003); (pp. 16, 75).

[63] G. L. Harding. "*Magnetron-sputtered metal carbide solar selective absorbing surfaces*". J. Vac. Sci. Technol. A, **16**, 857 (1979); (pp. 16–17).

[64] H. Biederman and L. Holland. "*Metal doped fluorocarbon polymer films prepared by plasma polymerization using an RF planar magnetron target*". Nucl. Instrum. and Methods, **212**, 497 (1983); (pp. 16–17).

[65] E. Kay. "*Synthesis and properties of metal clusters in polymeric matrices*". Z. Phys. D Atom. Mol. Cl. **3**, 251 (1986); (p. 16).

[66] B. Tkachuk, Y. Kobtsev, E. Laurs, V. Mikhal'chenko, and N. Marusii. "*Electrical conductivity of thin films of the polymer trimethylethynyl-tin*". Sov. Phys. J. **15**, 1485–1487 (1972); (pp. 16–17).

[67] H. Yasuda. "*Glow discharge polymerization*". J. Polym. Sci. Macromol. Rev. **16**, 199 (1981); (p. 17).

[68] J. Goodman. "*The formation of thin polymer films in the gas discharge*". J. Polym. Sci. **44**, 551 (1960); (p. 17).

[69] R. Subramanian and B. Garg. "*Recent Advances in Organotin Polymers*". **11**, 81 (1978); (p. 17).

[70] R. Sadhir, W. James, and R. Auerbach. "*Preparation of metallic organotin films by glow discharge polymerization and their properties*". Thin Solid Films, **97**, 17 (1982); (p. 17).

[71] E. Kay, A. Dilks, and U. Hetzler. "*Incorporation of Metals into Fluoropolymer Films Synthesized by Plasma Techniques*". J. Macromol. Sci. A, **12**, 1393 (1978); (p. 17).

[72] H. Urbassek. "*Sputtering of molecules*". Nucl. Instrum. and Methods B, **18**, 587 (1986); (p. 17).

[73] P. Kelly and R. Arnell. "*Magnetron sputtering: a review of recent developments and applications*". Vacuum, **56**, 159 (2000); (pp. 17–18).

[74] F. Penning. "*Die Glimmentladung bei niedrigem Druck zwischen koaxialen Zylindern in einem axialen Magnetfeld*". Physica, **3**, 873 (1936); (p. 17).

[75] R. HIPPLER, S. R. BHATTACHARYYA, and B. M. SMIRNOV. "*Formation and Deposition of Nanosize Particles on Surfaces*". In: M. BONITZ, N. HORING, and P. LUDWIG (eds.), *Introduction to Complex Plasmas*, (pp. 299–314). Springer, Berlin Heidelberg, 2010; (pp. 17–18).

[76] E. KAY. "*Magnetic Field Effects on an Abnormal Truncated Glow Discharge and Their Relation to Sputtered Thin-Film Growth*". J. Appl. Phys. **34**, 760 (1963); (p. 17).

[77] H. BIEDERMAN. "*RF sputtering of polymers and its potential application*". Vacuum, **59**, 594 (2000); (pp. 17–18).

[78] V. ZAPOROJTCHENKO, J. ZEKONYTE, S. WILLE, U. SCHUERMANN, and F. FAUPEL. "*Tailoring of the PS surface with low energy ions: Relevance to growth and adhesion of noble metals*". Nucl. Instrum. Methods Phys. Res. B, **236**, 95 (2005); (p. 18).

[79] J. ZEKONYTE, V. ZAPOROJTCHENKO, and F. FAUPEL. "*Investigation of the drastic change in the sputter rate of polymers at low ion fluence*". Nucl. Instrum. Methods Phys. Res. B, **236**, 241 (2005); (p. 18).

[80] K. SATTLER, J. MÜHLBACH, and E. RECKNAGEL. "*Generation of Metal Clusters Containing from 2 to 500 Atoms*". Phys. Rev. Lett. **45**, 821 (1980); (p. 19).

[81] H. HABERLAND, M. KARRAIS, M. MALL, and Y. THURNER. "*Thin films from energetic cluster impact: A feasibility study*". J. Vac. Sci. Technol. A, **10**, 3266 (1992); (p. 19).

[82] B. M. SMIRNOV, I. SHYJUMON, and R. HIPPLER. "*Flow of nanosize cluster-containing plasma in a magnetron discharge*". Phys. Rev. E, **75**, 066402 (2007); (p. 19).

[83] C. BINNS. "*Production of Nanoparticles on Supports Using Gas-Phase Deposition and MBE*". In: *Metallic Nanoparticles*, (pp. 49–71). Elsevier, Amsterdam, 2009; (p. 19).

[84] S. H. BAKER, S. C. THORNTON, A. M. KEEN, T. I. PRESTON, C. NORRIS, K. W. EDMONDS, and C. BINNS. "*The construction of a gas aggregation source for the preparation of mass-selected ultrasmall metal particles*". Rev. Sci. Instrum. **68**, 1853 (1997); (p. 19).

[85] S. H. BAKER, S. C. THORNTON, K. W. EDMONDS, M. J. MAHER, C. NORRIS, and C. BINNS. "*The construction of a gas aggregation source for the preparation of size-selected nanoscale transition metal clusters*". Rev. Sci. Instrum. **71**, 3178 (2000); (p. 19).

[86] R. Smalley. "*Laser Studies of Metal Cluster Beams*". Laser Chem. **2**, 167 (1983); (p. 19).

[87] J. B. Hopkins. "*Supersonic metal cluster beams of refractory metals: Spectral investigations of ultracold Mo2*". J. Chem. Phys. **78**, 1627 (1983); (p. 19).

[88] C. B. Murray, C. R. Kagan, and M. G. Bawendi. "*Synthesis and Characterization of monodisperse Nanocrystals and close-packes Nanaocrystal Assemblies*". Annu. Rev. Mater. Sci. **30**, 545 (2000); (pp. 19–20).

[89] H. O. Pierson. *Handbook of chemical Vapor Deposition*. Noyes Publications, Park Ridge, New Jersey, U.S.A., 1999; (p. 20).

[90] R. Gradess, R. Abargues, A. Habbou, J. Canet-Ferrer, E. Pedrueza, A. Russell, J. L. Valdés, and J. P. Martínez-Pastor. "*Localized surface plasmon resonance sensor based on Ag-PVA nanocomposite thin films*". J. Mater. Chem. **19**, 9233 (2009); (p. 20).

[91] D. W. Schubert and T. Dunkel. "*Spin coating from a molecular point of view: its concentration regimes, influence of molar mass and distribution*". Mater. Res. Innov. **7**, 314–321 (2003); (p. 20).

[92] K. Norrman, A. Ghanbari-Siahkali, and N. B. Larsen. "*6 Studies of spin-coated polymer films*". Annu. Rep. Prog. Chem., Sect. C: Phys. Chem. **101**, 174 (2005); (p. 20).

[93] L. L. Hench and J. K. West. "*The sol-gel process*". Chem. Rev. **90**, 33 (1990); (p. 20).

[94] N. Metropolis, A. W. Rosenbluth, M. N. Rosenbluth, A. H. Teller, and E. Teller. "*Equation of State Calculations by Fast Computing Machines*". J. Chem. Phys. **21**, 1087 (1953); (pp. 21, 24).

[95] F. Faupel, D. Gupta, B. D. Silverman, and P. S. Ho. "*Direct measurements of Cu diffusion into a polyimide below the glass transition temperature*". Appl. Phys. Lett. **55**, 357 (1989); (p. 21).

[96] B. D. Silverman. "*Single particle diffusion into a disordered matrix: simulation of a metal-polymer interface*". Macromolecules, **24**, 2467 (1991); (p. 21).

[97] L. Rosenthal, H. Greve, V. Zaporojtchenko, T. Strunskus, F. Faupel, and M. Bonitz. "*Formation of magnetic nanocolumns during vapor phase deposition of a metal-polymer nanocomposite: Experiments and kinetic Monte Carlo simulations*". J. Appl. Phys. **114**, 044305 (2013); (pp. 21, 81).

[98] S. A. KHAN, K.-H. HEINIG, and D. K. AVASTHI. "*Atomistic simulations of Au-silica nanocomposite film growth*". J. Appl. Phys. **109**, 094312 (2011); (p. 21).

[99] F. FAMILY and P. MEAKIN. "*Kinetics of droplet growth processes: Simulations, theory, and experiments*". Phys. Rev. A, **40**, 3836 (1989); (pp. 22, 45).

[100] J. CARREY and J.-L. MAURICE. "*Transition from droplet growth to percolation: Monte Carlo simulations and an analytical model*". Phys. Rev. B, **63**, 245408 (2001); (p. 22).

[101] J. CARREY and J.-L. MAURICE. "*Scaling laws near percolation during three-dimensional cluster growth: A Monte Carlo study*". Phys. Rev. B, **65**, 205401 (2002); (p. 22).

[102] F. FAMILY and P. MEAKIN. "*Scaling of the Droplet-Size Distribution in Vapor-Deposited Thin Films*". Phys. Rev. Lett. **61**, 428 (1988); (pp. 22, 45).

[103] H. TAKEUCHI and K. OKAZAKI. "*Molecular dynamics simulation of diffusion of simple gas molecules in a short chain polymer*". J. Chem. Phys. **92**, 5643 (1990); (p. 22).

[104] J. SONNENBURG, J. GAO, and J. H. WEINER. "*Molecular dynamics simulations of gas diffusion through polymer networks*". Macromolecules, **23**, 4653 (1990); (pp. 22, 46).

[105] R. H. BOYD and P. V. K. PANT. "*Molecular packing and diffusion in polyisobutylene*". Macromolecules, **24**, 6325 (1991); (pp. 22, 46).

[106] F. MÜLLER–PLATHE. "*Diffusion of penetrants in amorphous polymers: A molecular dynamics study*". J. Chem. Phys. **94**, 3192 (1991); (pp. 22, 46).

[107] R. M. SOK, H. J. C. BERENDSEN, and W. F. VAN GUNSTEREN. "*Molecular dynamics simulation of the transport of small molecules across a polymer membrane*". J. Chem. Phys. 4699 (1992); (pp. 22, 46).

[108] H. HABERLAND, Z. INSEPOV, and M. MOSELER. "*Molecular-dynamics simulation of thin-film growth by energetic cluster impact*". Phys. Rev. B, **51**, 11061 (1995); (p. 22).

[109] N. METROPOLIS and S. ULAM. "*The Monte Carlo Method*". J. Amer. Statist. Assoc. **44**, 335 (1949); (pp. 23–24).

[110] A. BARTH, A. LANG, and C. SCHWAB. "*Multilevel Monte Carlo method for parabolic stochastic partial differential equations*". BIT Numer. Math. **53**, 3 (2013); (p. 23).

[111] J. Skolnick and A. Kolinski. "*Dynamic Monte Carlo simulations of a new lattice model of globular protein folding, structure and dynamics*". J. Mol. Biol. **221**, 499 (1991); (p. 23).

[112] U. H. Hansmann and Y. Okamoto. "*New Monte Carlo algorithms for protein folding*". Curr. Opin. Struc. Biol. **9**, 177 (1999); (p. 23).

[113] P. P. Boyle. "*Options: A Monte Carlo approach*". J. Financ. Econ. **4**, 323 (1977); (p. 24).

[114] D. Bertsimas, L. Kogan, and A. W. Lo. "*When is time continuous?*" J. Financ. Econ. **55**, 173 (2000); (p. 24).

[115] G. Wood and J. Robertson. "*Buffon got it straight*". Stat. Prob. Lett. **37**, 415 (1998); (p. 24).

[116] G. Buffon. "*Essais d'Arithmétique morale*". Histoire naturelle, générale et particulière, **4**, 46 (1777); (p. 24).

[117] N. Metropolis. "*The Beginning of the Monte Carlo Method*". Los Alamos Science, **15**, 125 (1987); (p. 24).

[118] R. Eckhardt. "*Stan Ulam, John von Neumann, and the Monte Carlo Method*". Los Alamos Science, **15**, 131 (1987); (p. 24).

[119] J. E. Gubernatis. "*Marshall Rosenbluth and the Metropolis algorithm*". Phys. Plasmas, **12**, 057303 (2005); (p. 24).

[120] W. K. Hastings. "*Monte Carlo Sampling Methods Using Markov Chains and Their Applications*". Biometrika, **57**, 97 (1970); (pp. 24, 37).

[121] D. T. Gillespie. "*A general method for numerically simulating the stochastic time evolution of coupled chemical reactions*". J. Comput. Phys. **22**, 403 (1976); (pp. 25, 39, 49).

[122] D. T. Gillespie. "*Exact stochastic simulation of coupled chemical reactions*". J. Phys. Chem. **81**, 2340 (1977); (pp. 25, 39).

[123] D. T. Gillespie. "*Monte Carlo simulation of random walks with residence time dependent transition probability rates*". J. Comput. Phys. **28**, 395 (1978); (pp. 25, 39).

[124] P. Brémaud. *Markov Chains. Gibbs Fields, Monte Carlo Simulation, and Queues*. 1st ed. Springer, New York, 1999; (p. 25).

[125] A. KLENKE. *Wahrscheinlichkeitstheorie*. 2nd ed. Springer, Berlin, Heidelberg, 2008; (p. 25).

[126] P. S. LAPLACE. *Essai philosophique sur les probabilités*. Courcier, 1814; (p. 26).

[127] S. P. LALLEY. "*Continuous Time Markov Chains*". Lecture Notes, University of Chicago, 2012 (p. 34).

[128] K. A. FICHTHORN and W. H. WEINBERG. "*Theoretical foundations of dynamical Monte Carlo simulations*". J. Chem. Phys. **95**, 1090 (1991); (p. 43).

[129] K. A. FICHTHORN and M. SCHEFFLER. "*Island Nucleation in Thin-Film Epitaxy: A First-Principles Investigation*". Phys. Rev. Lett. **84**, 5371 (2000); (p. 43).

[130] M. ZIEGLER, J. KRÖGER, R. BERNDT, A. FILINOV, and M. BONITZ. "*Scanning tunneling microscopy and kinetic Monte Carlo investigation of cesium superlattices on Ag(111)*". Phys. Rev. B, **78**, 245427 (2008); (p. 43).

[131] N. N. NEGULYAEV, V. S. STEPANYUK, L. NIEBERGALL, W. HERGERT, H. FANGOHR, and P. BRUNO. "*Self-organization of Ce adatoms on Ag(111): A kinetic Monte Carlo study*". Phys. Rev. B, **74**, 035421 (2006); (p. 43).

[132] V. S. STEPANYUK, N. N. NEGULYAEV, L. NIEBERGALL, R. C. LONGO, and P. BRUNO. "*Adatom Self-Organization Induced by Quantum Confinement of Surface Electrons*". Phys. Rev. Lett. **97**, 186403 (2006); (p. 43).

[133] M. BONITZ, L. ROSENTHAL, K. FUJIOKA, V. ZAPOROJTCHENKO, F. FAUPEL, and H. KERSTEN. "*Towards a Particle Based Simulation of Complex Plasma Driven Nanocomposite Formation*". Contrib. Plasma Phys. **52**, 890 (2012); (pp. 44, 53).

[134] L. ROSENTHAL, A. FILINOV, M. BONITZ, V. ZAPOROJTCHENKO, and F. FAUPEL. "*Diffusion and Growth of Metal Clusters in Nanocomposites: A Kinetic Monte Carlo Study*". Contrib. Plasma Phys. **51**, 971 (2011); (pp. 44, 53).

[135] V. ZAPOROJTCHENKO, K. BEHNKE, T. STRUNSKUS, and F. FAUPEL. "*Determination of condensation coefficients of metals on polymer surfaces*". Surf. Sci. **454**, 412 (2000); (pp. 45, 53, 81, 84).

[136] J. KOUTECKÝ, V. BONAČIĆ-KOUTECKÝ, L. ČEŠPIVA, and P. FANTUCCI. "*Effective core potential-configuration interaction study of electronic structure and geometry of small neutral and cationic Ag_n clusters: Predictions and interpretation of measured properties*". J. Chem. Phys. **98**, 7981 (1993); (p. 45).

[137] A. A. Gusev and U. W. Suter. "*Dynamics of small molecules in dense polymers subject to thermal motion*". J. Chem. Phys. **99**, 2228 (1993); (p. 46).

[138] F. Faupel. "*Metal diffusion in high-temperature polymers*". Adv. Mater. **2**, 266 (1990); (p. 47).

[139] M. H. Cohen and D. Turnbull. "*Molecular Transport in Liquids and Glasses*". J. Chem. Phys. **31**, 1164 (1959); (p. 47).

[140] J. S. Vrentas and J. L. Duda. "*Diffusion in polymer—solvent systems. I. Reexamination of the free-volume theory*". J. Polym. Sci. A1, **15**, 403 (1977); (p. 48).

[141] J. S. Vrentas and J. L. Duda. "*Diffusion in polymer–solvent systems. II. A predictive theory for the dependence of diffusion coefficients on temperature, concentration, and molecular weight*". J. Polym. Sci. A1, **15**, 417 (1977); (p. 48).

[142] J. S. Vrentas and J. L. Duda. "*Diffusion in polymer–solvent systems. III. Construction of Deborah number diagrams*". J. Polym. Sci. A1, **15**, 441 (1977); (p. 48).

[143] J. S. Vrentas and C. M. Vrentas. "*Predictive methods for self-diffusion and mutual diffusion coefficients in polymer–solvent systems*". Eur. Polym. J. **34**, 797 (1998); (p. 48).

[144] J. Liu, D. Cao, and L. Zhang. "*Molecular Dynamics Study on Nanoparticle Diffusion in Polymer Melts: A Test of the Stokes-Einstein Law*". J. Phys. Chem. C, **112**, 6653 (2008); (pp. 48–49).

[145] A. Tuteja, M. E. Mackay, S. Narayanan, S. Asokan, and M. S. Wong. "*Breakdown of the Continuum Stokes-Einstein Relation for Nanoparticle Diffusion*". Nano Lett. **7**, 1276 (2007); (p. 48).

[146] J. Won, C. Onyenemezu, W. G. Miller, and T. P. Lodge. "*Diffusion of Spheres in Entangled Polymer Solutions: A Return to Stokes-Einstein Behavior*". Macromolecules, **27**, 7389 (1994); (p. 48).

[147] M. Krüger and M. Rauscher. "*Diffusion of a sphere in a dilute solution of polymer coils*". J. Chem. Phys. **131**, 094902 (2009); (p. 49).

[148] R. Tuinier, J. K. G. Dhont, and T.-H. Fan. "*How depletion affects sphere motion through solutions containing macromolecules*". Europhys. Lett. **75**, 929 (2006); (p. 49).

[149] R. Tuinier and T.-H. Fan. "*Scaling of nanoparticle retardation in semi-dilute polymer solutions*". Soft Matter, **4**, 254 (2008); (p. 49).

[150] D. H. COLE, K. R. SHULL, L. E. REHN, and P. BALDO. "*Metal-Polymer Interactions in a Polymer/Metal Nanocomposite*". Phys. Rev. Lett. **78**, 5006 (1997); (p. 49).

[151] F. FAUPEL, A. THRAN, V. ZAPOROJTCHENKO, M. KIENE, T. STRUNSKUS, and K. BEHNKE. "*Nucleation, growth, interdiffusion, and adhesion of metal films on polymers*". AIP Conf. Proc. **491**, 201 (1999); (p. 53).

[152] Y. N. C. CHAN, G. S. W. CRAIG, R. R. SCHROCK, and R. E. COHEN. "*Synthesis of palladium and platinum nanoclusters within microphase-separated diblock copolymers*". Chem. Mater. **4**, 885 (1992); (pp. 59, 91).

[153] J. RÖDER and H.-U. KREBS. "*Tuning the microstructure of pulsed laser deposited polymer-metal nanocomposites*". Appl. Phys. A, **85**, 15 (2006); (pp. 59, 91).

[154] D. STAUFFER. *Introduction To Percolation Theory*. 2nd revised ed. Taylor & Francis, London, 2003; (p. 69).

[155] H. GREVE, C. POCHSTEIN, H. TAKELE, V. ZAPOROJTCHENKO, F. FAUPEL, A. GERBER, M. FROMMBERGER, and E. QUANDT. "*Nanostructured magnetic Fe–Ni–Co/Teflon multilayers for high-frequency applications in the gigahertz range*". Appl. Phys. Lett. **89**, 242501 (2006); (p. 75).

[156] J. A. VENABLES, G. D. T. SPILLER, and M. HANBUCKEN. "*Nucleation and growth of thin films*". Rep. Prog. Phys. **47**, 399 (1984); (p. 77).

Publications in Peer Reviewed Journals

1. L. Rosenthal, A. Filinov, M. Bonitz, V. Zaporojtchenko, and F. Faupel. *"Diffusion and Growth of Metal Clusters in Nanocomposites: A Kinetic Monte Carlo Study"*. Contrib. Plasma Phys. **51**, 971–980 (2011).

2. M. Bonitz, L. Rosenthal, K. Fujioka, V. Zaporojtchenko, F. Faupel, and H. Kersten. *"Towards a Particle Based Simulation of Complex Plasma Driven Nanocomposite Formation"*. Contrib. Plasma Phys. **52**, 890–898 (2012).

3. L. Rosenthal, H. Greve, V. Zaporojtchenko, T. Strunskus, F. Faupel, and M. Bonitz. *"Formation of magnetic nanocolumns during vapor phase deposition of a metal-polymer nanocomposite: Experiments and kinetic Monte Carlo simulations"*. J. Appl. Phys. **114**, 044305–044305-7 (2013).

Danksagung

An erster Stelle möchte ich mich bei Prof. Dr. Michael Bonitz bedanken, der mich vor mittlerweile 5 Jahren in seine Arbeitsgruppe aufgenommen hat und mir die Gelegenheit gab, diese Arbeit anzufertigen. Seine hilfreichen Anregungen und Kommentare haben viel zu dieser Arbeit beigetragen.

Ein besonderer Dank für ihre stetige Unterstützung geht an Prof. Dr. Franz Faupel, Dr. Thomas Strunskus sowie Dr. Vladimir Zaporojtchenko. Insbesondere die Diskussionen mit Vladimir, der durch seinen plötzlichen Tod das Ende dieser Arbeit leider nicht mehr miterleben konnte, waren in vielen Momenten sehr hilfreich.

Allen Mitgliedern der Arbeitsgruppe danke ich für das herzliche Miteinander während der letzten Jahre. Besonders hervorheben möchte ich David Hochstuhl, Kenji Fujioka und Jan Willem Abraham, die mich bei der Durchsicht der Arbeit unterstützt haben. Für viele interessante Gespräche sowie die stetige Hilfe bei diversen technischen Problemen bedanke ich mich bei meinem Bürokollegen Tim Schoof.

Ein ganz besonderer Dank geht an meine Kinder Theodor, Elena und Tabea, dafür, dass wir jeden Tag viele schöne Momente zusammen verbringen und sie mir gezeigt haben, dass auch fünf Stunden Schlaf mit vier Unterbrechungen ausreichen, um sich am folgenden Tag neun Stunden zu konzentrieren ☺.

Mein größter Dank gilt jedoch meiner Frau Maren für ihre Liebe, ihre Aufopferung und ihre stetige Unterstützung während der letzten Jahre.

Selbständigkeitserklärung

Hiermit versichere ich, dass die vorliegende Abhandlung – abgesehen von der Beratung durch den Betreuer – nach Inhalt und Form die eigene Arbeit ist.

Des Weiteren versichere ich, dass die Arbeit unter Einhaltung der Regeln guter wissenschaftlicher Praxis[1] der Deutschen Forschungsgemeinschaft entstanden ist.

Ich versichere, dass die vorliegende Arbeit weder ganz noch zum Teil schon einer anderen Stelle im Rahmen eines Prüfungsverfahrens vorgelegen hat, sowie in dieser Form weder veröffentlicht worden ist noch zur Veröffentlichung eingereicht wurde. Die im Rahmen der Arbeit entstandenen Publikationen in wissenschaftlichen Fachzeitschriften sind auf Seite 113 vermerkt.

Kiel,

[1] Deutsche Forschungsgemeinschaft. *Vorschläge zur Sicherung guter wissenschaftlicher Praxis. „Empfehlungen der Kommission Selbstkontrolle in der Wissenschaft“*, Wiley-VCH, Weinheim (1998).